DEVELOPMENT OF A VIBRATION-BASED MEMS ENERGY HARVESTER

LIU HUICONG

NATIONAL UNIVERSITY OF SINGAPORE

2012

DEVELOPMENT OF A VIBRATION-BASED MEMS ENERGY HARVESTER

BY

LIU HUICONG

(M. Eng.)

A THESIS SUBMITTED

FOR THE DEGREE OF DOCTOR OF PHILOSOPHY

DEPARTMENT OF MECHANICAL ENGINEERING

NATIONAL UNIVERSITY OF SINGAPORE

2012

DECLARATION

I hereby declare that this thesis is my original work and it has been written by me in its entirety. I have duly acknowledged all the sources of information which have been used in the thesis.

This thesis has also not been submitted for any degree in any university previously.

Liu Huicong 20/12/2012

Liu Huicong

20 Dec 2012

Acknowledgements

I would like to express my sincere gratitude to my supervisors Prof. Tay Cho Jui, Prof. Quan Chenggen and Prof. Lee Chengkuo for their consistent support, encouragement and discussions during my entire Ph. D. study. I would like to gratefully acknowledge Prof. Tay and Quan for spending their personal time for the corrections and revisions of my papers and this thesis. I would never forget Prof. Lee's sacrifice for spending hours and hours with me for research discussions. I am really fortunate to have their consistent concern and help, and it is their inspiration and guidance that enable me to complete this work.

I would like to thank all lab technologists at the Experimental Mechanics Laboratory, Dynamic Laboratory, Center of Integrated Circuit Failure Analysis & Reliability Laboratory and Institute of Microelectronics. I am grateful to Mr. Chiam, Mr. Ching, Mrs. Ho, and so on for their constant and kindly help on my experiments. This work would not have been what it is without the collaboration and cooperation from Dr. Kobayashi Takeshi of the National Institute of Advanced Industrial Science and Technology (AIST), Japan.

I must express a big thank you to all my past and present colleagues and friends, who spend their valuable time in all possible discussions and technical support. These people include Dr. Basanta Bhaduri, Dr. Niu Hongtao, Dr. Chen Wen, Dr. Fu Yu, Prof. Yang Bin, Prof. Xiang Wenfeng, Dr. Xie Jin, Mr. Lou Liang, Mr. Wang Nan, Mr. Qian You, Mr. Zhang Songsong, Mr. Li Bo, Mr. Koh Kah How, Mr. Soon Bo

Woon, Mr. Pitchappa Prakash and so on. I wish to thank my nearest friend Ms. Li Zhonghua together with all others. I enjoyed their friendship and their support. I have really spent a memorable life with them during my stay at NUS.

Last but not the least, I would like to express my sincere gratitude to my family. I would not be able to make such adventure without their strong encouragement, support, patience and love. Finally, all the contributions from the many not named above are not forgotten, but greatly appreciated.

Table of Contents

Summary

Vibration-based energy harvesting technique has been considered as a promising technology and has attracted noticeable research interests. In practical applications, ambient vibrations are normally at low frequencies, or with random and irregular frequency peaks, or contain various frequency peaks in different directions. These features have limited the output performance and applicability of traditional micro-electro-mechanical systems (MEMS) energy harvesters. This thesis mainly focuses on the development of new MEMS energy harvesting systems for providing reasonable and promising solutions to current challenges.

In this investigation, a wideband MEMS piezoelectric energy harvester (PEH) system incorporating stoppers has been developed for scavenging energy from low and random environmental vibrations. The key factors for the frequency response of the system, including base acceleration, damping ratio, frequency characteristic and stopper distance, have been studied based on a mechanical model. With predetermined stopper distances, the system has achieved a wideband range of 32-42 Hz for one-side stopper and 30-48 Hz for two-side stoppers at 0.6 g. To date, such low and wide operating range has not been reported for piezoelectric MEMS energy harvesters.

By incorporating high-frequency lead zirconate titanate (PZT) energy harvesting cantilevers as frequency-up-conversion (FUC) stoppers, two PEH systems (PEH-I and PEH-II) have been investigated, which have the capability of converting low and

random ambient vibrations to high-frequency self-oscillations of the devices. In the PEH-II system, the operating frequency range of a meandered PZT cantilever which has a low resonant frequency of 20 Hz has been broadened to 13-26 Hz. The peak-power density of the system reaches to 159.4 $\mu W/cm^3$ at a relatively low frequency of 25 Hz and an acceleration of 0.8 g. The proposed system provides a major advantage of realizing both frequency widening and FUC simultaneously. The design offers a possible solution for harvesting of energy from extremely low frequency vibrations such as that of human motion.

A three-dimensional (3-D) driven electromagnetic MEMS energy harvester with multiple resonant modes is also proposed to scavenge energy from out-of-plane mode I (frequency of 1285 Hz), in-plane mode II (frequency of 1470 Hz) and mode III (frequency of 1550 Hz) vibrations. These three vibration modes are perpendicular to each other. The overall optimized power densities of 0.444, 0.242 and 0.125 $\mu W/cm^3$ have been achieved at various respective modes. The results show a good potential for realizing a practical 3-D vibration-based energy harvester device, which will overcome the limitations of the traditional one-dimensional (1-D) energy harvester.

For each of the proposed energy harvesting system, the design configuration, fabrication, modeling, simulation, voltage and power evaluations are presented in subsequent chapters. A list of publications arising from this research is shown in Appendix C.

List of Tables

List of Figures

List of Acronyms

MEMS	Micro-electro-mechanical systems
PZT	Lead Zirconate Titanate
FUC	Frequency-up-conversion
PEH	Piezoelectric energy harvester
3-D	Three-dimensional
1-D	One-dimensional
IC	Integrated circuit
WSNs	Wireless sensor networks
RF	Radio frequency
PV	Photovoltaic
Si	Silicon
TPGs	Thermoelectric power generators
AlN	Aluminum-nitride
Al	Aluminum
PDMS	Polydimethylsiloxane
PVDF	Polyvinylidene fluoride
FIG	Frequency-increased generator
2-D	Two-dimensional
DOF	Degree-of-freedom
PEH-L	Low-frequency piezoelectric PZT energy harvesting cantilever
PEH-H	High-frequency piezoelectric PZT energy harvesting cantilever

SOI	Silicon-on-insulator
BOX	Buried oxide
RIE	Reactive ion etching
DRIE	Deep reactive ion etching
DIP	Dual in-line package
DSA	Dynamic signal analyzer
PCB	Printed circuit board
FA	Fine-adjustment
NFB	Normalized frequency bandwidth
FUC-1	FUC oscillator 1
FUC-2	FUC oscillator 2
LRF	Low-resonant-frequency
HRF	High-resonant-frequency
PECVD	Plasma-enhanced chemical vapor deposition
PVD	Physical vapor deposition
SEM	Scanning electron micrograph

List of Symbols

d_{31}	Piezoelectric constant for 3-1 mode
d_{33}	Piezoelectric constant for 3-3 mode
t_e	Thickness of the piezoelectric layer
t_b	Thickness of the supporting beam
l_b	Length of the supporting beam
l_m	Length of the proof mass
w_b	Width of the supporting beam
w_m	Width of the proof mass
x	Variable distance starting from the beam anchor to the beam tip
δ_m	Mass tip displacement of cantilever
δ_c	Mass center displacement of cantilever
δ_b	Beam tip displacement of cantilever
$\xi_1(x)$	Mechanical strain distribution along the piezoelectric layer
σ_1	Mechanical stress σ_1 applied in a longitudinal direction
D_3	Induced electrical displacement across the piezoelectric layer
E_3	Applied electrical field across the piezoelectric layer
s_{11}	Axial elastic compliance under a constant electric field
ε_0	Vacuum dielectric coefficient
ε_{33}	Transverse dielectric coefficient measured at a constant stress
d_{31}	Transverse-axial piezoelectric constant
C_e	Capacitance of piezoelectric layer

E	Young's modulus of the piezoelectric material
$V_{o.c.}$	Open circuit voltage generated across the piezoelectric layer
$V_{o.c.m}$	Open circuit voltage in terms of mass tip displacement
$V_{o.c.c}$	Open circuit voltage in terms of mass center displacement
P_{rms}	Average power delivered to the connected load
Z_P	Complex impedance of the piezoelectric capacitor
Z_L	Complex impedance of the connected load
R_L	Resistance of the connected load
$\delta_1 = \frac{d_1}{Y}$	Dimensionless top-stopper distance
$\delta_2 = \frac{d_2}{Y}$	Dimensionless bottom-stopper distance
$\rho = \frac{\omega}{\omega_0}$	Dimensionless base excitation frequency characteristic
$\rho_1 = \frac{\omega_1}{\omega_0}$	Dimensionless frequency characteristics of a secondary suspension system (top stopper)
$\rho_2 = \frac{\omega_2}{\omega_0}$	Dimensionless frequency characteristics of a secondary suspension system (bottom stopper)
A	Relative displacement amplitude of frequency response
$a=A/Y$	Dimensionless relative displacement amplitude of frequency response
α	Angle of incident light
θ	Angle of PZT cantilever deflection
$\beta = \alpha - 2\theta$	Minimum angle of the deflection light
$\gamma = \alpha + 2\theta$	Maximum angle of the deflection light
L	Maximum sweeping distance on the surface plate
L_0	Distance between the PZT cantilever and surface plate
L_1	Distance between the maximum sweeping point to the datum point

L_2	Distance between the minimum sweeping point to the datum point
$\ddot{y}\sin(\omega t)$	Harmonic excitation acceleration
T_1	Normal force applied to FUC-1 by the excitation oscillator
T_2	Normal force applied to FUC-2 by the excitation oscillator
C_R	Coefficient of restitution of the materials coming into contact
v_0	Instantaneous velocity of the excitation oscillator when it just makes contact with the FUC oscillators
v_1	Instantaneous velocity of FUC-1 when the excitation oscillator just makes contact with it
v_2	Instantaneous velocity of FUC-2 when the excitation oscillator just makes contact with it
V_1	Ensuing velocity of the combined FUC-1 system
V_2	Ensuing velocity of the combined FUC-2 system
M	Mass of a spring-mass-damper system
K	Spring stiffness of a spring-mass-damper system
C	Damping factor of a spring-mass-damper system
$Z(t)$	Relative mass displacement of the spring-mass-damper system
$Y(t)$	Harmonic excitation applied to the spring-mass-damper system
$\omega_n = 2\pi f_r$	Resonant frequency of the spring-mass-damper system
ς	Overall damping ratio of the spring-mass-damper system
φ	Phase angle between the base excitation and mass motion
$B(t)$	Magnetic field strength
$\dot{B}(t)$	The rate of change of the magnetic field strength
B_r	Residual magnetic field strength
Φ	Magnetic flux density
i	Order number of each coil loop
n	Total number of loops of a coil

A_B	Area of magnetic field
A_i	Magnetic field area included in the *i*-th loop
ε	Electromotive force (emf)
ε_{out}	Induced voltage by out-of-plane mass motion
ε_{in}	Induced voltage by in-plane mass motion
r	Radius of the magnet
h	Length of the magnet
$d(t)$	Gap distance from the coil to the magnet
d_0	Initial gap distance from the coil to the magnet
l_i	Effective length of each loop included in the electromagnetic field
v	In-plane velocity of mass motion
θ_i	Angle between the in-plane velocity and the induced current direction along each wire
$\vec{v}_0$	Input excitation velocity
$\vec{v}_e$	Effective driving velocity
$v_r(t)$	Mass motion velocity at resonance
α'	Angle of the input excitation velocity
β'	Angle of the in-plane resonant mode
$\gamma' = \beta' - \alpha'$	Angle between the input velocity and the resonant mode

Chapter 1

Introduction

In recent times, the ever increasing demand for ultra portable and highly efficient energy sources requires innovative solutions. MEMS are miniaturized devices that enable the operation of complex systems [1]. They might comprise the following: a sensor that measures a physical quantity and converts it into a signal; an electronic circuit that conditions the sensor signal; and an actuator that responds to the electrical signals generated within the circuit [2]. MEMS devices take advantage of integrated circuit (IC) fabrication techniques and thus have the characteristics of miniaturization, lower power consumption, lower cost, and ease of integration with electronics [3]. Research on the application of MEMS to energy systems, which is often referred to as power MEMS or MEMS energy harvesters, has been steadily gaining momentum.

1.1 Motivations

With the advances in highly integrated microelectronics and wireless communication technologies, there is a rapid emergence of low cost, intelligent, wireless sensor networks (WSNs) in the past few years. A WSN consists of hundreds of spatially distributed ad-hoc micro sensor nodes of low power consumption and multi-function for continuous sensing, event detection, location sensing, and local control of

actuators. This sensor-rich environment, referred to as “Ambient Intelligence” or “Smart Environments”, will dramatically improve the quality of lives in terms of environment, security, education, health and well being, and comfort. There have been a variety of applications for WSNs suggested in the literature [4, 5] and they can roughly be classified into five categories: military, environment, health, home and other commercial areas.

A wireless sensor node, as a micro-electronic device, is made up of four basic components [6]: a sensing unit, a processing unit, a transceiver unit and a power unit. The power unit as one of the most important components may be supported by a power scavenging unit such as solar cells. In some application scenarios, replenishment of energy resources might be impossible. Therefore, sensor nodes are implemented in a “deploy and forget” scenario since the battery replacement will be prohibitive and impractical [7]. Sensor node lifetime, therefore, shows a strong dependence on battery lifetime. State of the art, non-rechargeable lithium batteries can provide up to 800 Wh/l (watt hours per liter) or 2880 J/cm^3. If an electronic device with a 1 cm^3 battery is to consume 100 μW of power on average, the device could last 8000 hours or 333 days, almost a year. Clearly, a lifetime of 1 year is far from sufficient [8]. Not to mention that the sensors and electronics of a wireless sensor node will be far smaller than 1 cm^3, in this case, the battery would dominate the system volume. Therefore, the development of alternative power sources for wireless sensor and actuator nodes is acute.

Significant research is ongoing to deliver power from the environment using energy harvesting technology, which can harvest or convert a variety of ambient wasted and unused energy such as solar energy, vibration/ motion energy, thermal gradient, etc [9, 10] into electric energy, and deliver energy directly to a wireless sensor load or to a

storage element such as a rechargeable battery or capacitor. Some of the major benefits of energy harvesting technology for WSNs are stated [11] as: Firstly, energy harvesting solution can reduce the dependency on battery power and provide long-time solutions. With the advancement of microelectronics, the power consumptions of sensor nodes have been reduced significantly. Hence harvested ambient environmental energy may be sufficient to replace battery completely. Secondly, energy harvesting solution would reduce installation and maintenance cost. Self-powered sensor nodes do not require power cables wiring and conduits, hence they are very easy to install. The heavy installation cost can be reduced greatly [12]. Clearly, it can be deduced that energy harvesting technology is a promising solution to power WSNs for extended operation with the supplement of the energy storage devices.

There are various sources of energy available for energy harvesting, and indeed, many works have been presented on generating electrical energy from solar energy [13-16], temperature gradients [17-21], ambient radio frequency (RF) [22-24], vibrations [25, 26], and human motions [27]. The comparisons of different power sources and their performances in terms of power density are summarized in Table 1.1. The values in the table are derived from published studies, theory and information that is commonly available in data sheets and textbooks. The advantages and disadvantages of various energy harvesting sources are discussed thoroughly in [28-30] and consequently the arguments will not be repeated here in detail. It is seen that solar energy and vibrations offer the most attractive energy scavenging solutions. Both solutions meet the power density requirement in environments that are of interest for WSNs. Solar devices can achieve relatively high power densities in good light conditions, but they are unsuitable for implantable devices or other low light situations. Kinetic energy in the form of motion or vibration is generally the most

versatile and ubiquitous ambient energy source available. It can also provide a good power density and thus is more suitable for harvesting [31]. Therefore, the main focus and development effort of this thesis is vibration-based energy harvesters, which convert energy in the form of mechanical vibrations in the ambient environment into electrical energy by using piezoelectric, electromagnetic, and electrostatic mechanisms [32]. A general vibration to electricity model has been provided [33, 34]. Based on literature survey, different energy conversion mechanisms are presented and discussed in the next. The output performances of the reported vibration-based energy harvesters are summarized as well.

Table 1.1 Comparison of energy harvesting approaches

Energy source	Power density & performance	Source of information
Solar (outdoors)	15 mW/cm^2 (direct sun) 0.15 mW/cm^2 (cloudy day)	Commonly available
Solar (indoors)	0.01 mW/cm^2 (standard office desk) 0.57 mW/cm^2 (< 60 W desk lamp)	Commonly available
Thermal gradient	15 μW/cm^3 @ 10˚C gradient	Stordeur and Stark [15]
Ambient RF	1 μW/cm^2	Hudak and Amatucci [18]
Acoustic noise	0.003 @ 75 Db 0.96 @ 100 Db	Rabaey et al [19]
Vibrations (piezoelectric)	200 μW/cm^3	Roundy et al [20]
Vibrations (micro generator)	4 μW/cm^3 (human motion - Hz) 800 μW/cm^3 (machines - kHz)	Mitcheson et al [21]
Passive human-power	330 μW/cm^2 (shoe inserts)	Schenck and Paradiso [22]

1.2 Vibration-Based Energy Harvesters

1.2.1 Piezoelectric energy conversion

Piezoelectric materials have been used to convert mechanical energy into electrical energy based on piezoelectric effect. It occurs when a charge balance within the crystal lattice of a piezoelectric material is disturbed. When there is no applied stress

on the material, the positive and negative charges are evenly distributed so there is no potential difference. If the material is compressed, a voltage of the same polarity as the poling voltage will appear between the electrodes. If stretched, a voltage of opposite polarity will appear. Piezoelectric materials are mainly utilized in one of two forms, 3-3 mode or 3-1 mode, as shown in Fig. 1.1. With the 3-3 mode, compressive strain is applied parallel to the electrodes, while voltage is generated along the same axis as the applied force. With the 3-1 mode, strain is applied perpendicular to the electrodes, so the direction of voltage generation is perpendicular to the applied force. Material performance is quantified by the piezoelectric constant d_{3i}, which is the ratio of the short circuit charge density to applied stress (in units of C/N). Materials typically have a d_{33} coefficient that is higher than the d_{31} coefficient, but 3-1 mode is easier to implement in devices for vibration energy harvesting.

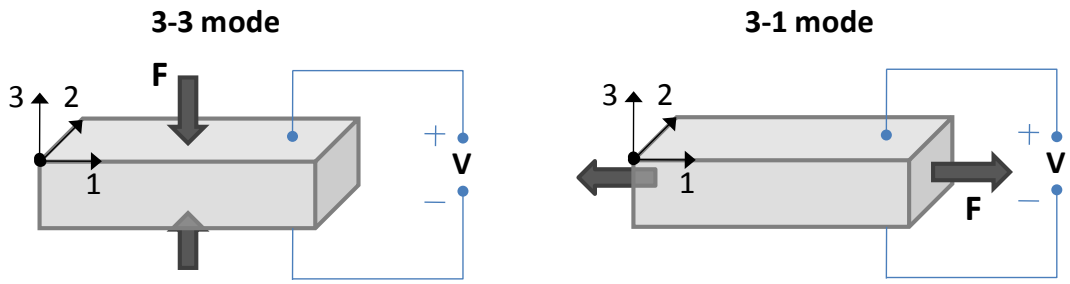

Figure 1.1 Piezoelectric coupling modes.

As shown in Fig. 1.2, piezoelectric energy harvesters usually take the form of a bimorph cantilever [35-39]. A cantilever beam structure with piezoelectric material attached to the top and bottom surfaces acts as a spring. The addition of a proof mass at the end of the beam lowers the resonant frequency. The structure is designed to operate in a bending mode thereby straining the piezoelectric films and generating a charge from the piezoelectric effect. Deflection of the beam causes piezoelectric materials to undergo tension and compression, and thus generate electricity.

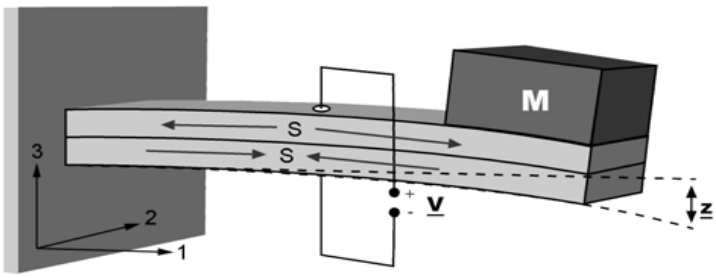

Figure 1.2 Cantilever configuration of a piezoelectric energy harvester [35].

In recent years, many devices based on cantilever structures have been developed with microfabrication techniques, instead of previous bulk prototypes. A piezoelectric MEMS energy harvester working in 3-1 mode [40-43] normally contains a composite cantilever with integrated proof mass. The composite cantilever is made of a piezoelectric film, such as PZT, sandwiched between a pair of metal electrodes and a Si substrate as shown in Fig. 1.4(a). In addition to parallel electrodes, inter-digital electrodes have also been designed to realize a 3-3 mode piezoelectric coupling [44-46] as shown in Fig. 1.4(b). Lee et al. [45] have designed and fabricated two piezoelectric energy harvesters with 3-1 mode and 3-3 mode electrodes as shown in Fig. 1.3. Aluminum–nitride (AlN) is another preferable piezoelectric material for energy harvesting since it has much lower dielectric constant compared with PZT and the power generation is quite comparable [47-49].

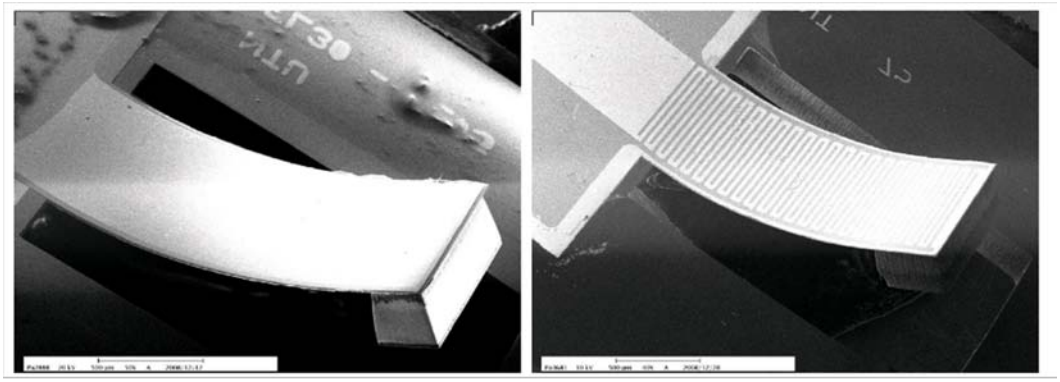

Figure 1.3 PZT energy harvesters with (a) 3-1 mode and (b) 3-3 mode electrodes [45].

The deposition processes of PZT (Sol-gel) and AlN (sputter) limit the thin film thickness within 1~2 μm. Recently, researchers have developed screen-printing [50] and bulk-PZT micro processes [51] to significantly increase the piezoelectric film thickness on beam as shown in Fig. 1.4. Aktakka et al. [51] fabricated a thinned-PZT/Si unimorph cantilever for vibration energy harvesting. An unpackaged harvester with a tungsten proof mass produces 2.74 μW at 0.1 g (167 Hz), and 205 μW at 1.5 g (154 Hz) at resonance. This might be the highest power output and power density amongst reported microfabricated vibration-based energy harvesters.

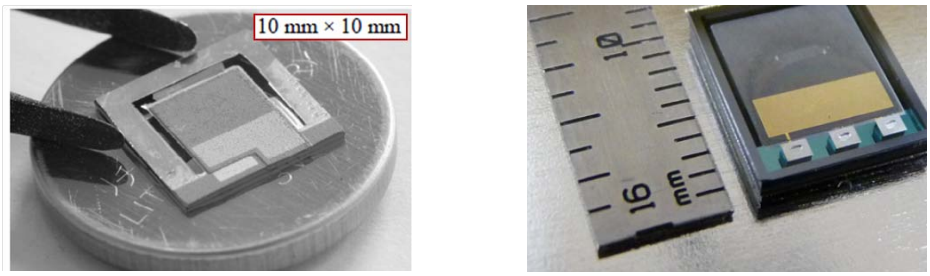

(a) (b)

Figure 1.4 MEMS bulk PZT energy harvesters by (a) Xu [50] and (b) Aktakka [51].

Table 1.2 summarizes the performance of the reviewed piezoelectric energy harvesters in terms of resonant frequency (Hz), input acceleration (m/s^2), volume (cm^3), power (μW) and power density ($\mu W/cm^3$). It is found that the micro piezoelectric energy harvesters exhibit competitive performance relative to the manually assembled devices. Though the micro harvesters have relatively low output power (normally several or tens of micro watts) compared to macro assembled harvesters (hundreds of micro watts), the power density of the micro harvesters are much higher because of their relatively smaller device sizes, some are in several mW/cm^3. While the resonant frequencies of these micro cantilever structures are normally higher than 200 Hz, some are even in kHz range.

1.2.2 Electromagnetic energy conversion

Based on Faraday's law of electromagnetic induction, a conductor (typically in form of coils) situated in a changing magnetic field or a conductor moving through a stationary magnetic field generates electricity. One typical energy harvester prototype as illustrated in Fig. 1.5 is to fix the coil on plane housing and attach a magnet (as mass) on a vibratile or flexible structure (as spring). When the device vibrates, the mass will move out of phase with the housing, so that there is a net displacement between the magnet and coil, resulting in the generation of electrical energy by an electromagnetic transducer. There is a wide variety of electromagnetic energy harvesters based on such spring-mass-coil configurations have been reported [52-58].

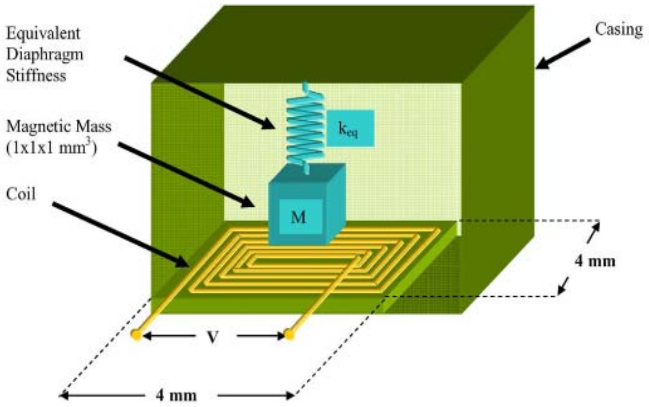

Figure 1.5 Model of a mass/coil type electromagnetic energy harvester.

Kulkarni et al. [59] reported three different designs of partially micro-fabricated energy harvesters. The integrated coil, paddle and beam were fabricated using standard MEMS processing techniques. A group from Chinese University of Hong Kong developed a micro harvester by using a small NdFeB magnet supported by a laser-micromachined Cu spring structure [60, 61]. Wang and Arnold [62] reported three fully-integrated, fully-batch microfabricated electromagnetic energy harvesters, which utilize polydimethylsiloxane (PDMS) diaphragms and embedded NdFeB

powder micro-magnet. Jiang et al. [63] reported an in-plane MEMS-based electromagnetic energy harvester by bonding a vibrator with embedded micro-magnets and a stator with integrated micro-coils. The micro-magnets are formed by using sputtering deposition of multilayered magnetic films and Si molding techniques. Recently, Cepnik and Wallrabe [64] introduced a flat micro electromagnetic energy harvester with a volume of 0.9 cm^3. The back iron plate attached with multiple pairs of magnets is mounted onto a ground plate by two pairs of springs enabling a relative in-plane motion to the meandering coil base in the central layer.

Table 1.3 summarizes the performance of the reviewed electromagnetic energy harvesters. The output power of the electromagnetic harvesters vary greatly from less than one to hundreds of micro-watts. While the power densities are in a range of several to hundreds of micro-watts. Prototypes that in excess of 2 miliwatts per cube-centimeter is possible but rare. Using a permanent magnet as the proof mass enables a low resonant frequency of less than 200 Hz for the vibrating cantilever designs. In-plane vibration-driven energy harvesters are also feasible for electromagnetic energy conversion.

1.2.3 Electrostatic energy conversion

Electrostatic energy conversion is based on a parallel plate capacitor which are electrically isolated from each other typically by air, vacuum or an insulator. The plates charged by a battery of voltage will create equal but opposite charges on each resulting in the charge storage. For a parallel plate capacitor, C is given by $C=Q/V$, where C is the capacitance $C = \varepsilon A / d$, Q is the charge on the plate and V is the voltage on the plates, ε is the permittivity of the material between the plates, A is the area of the plates in and d is the separation distance between the plates. Thus the energy

stored in a capacitor, with plate charge Q and potential difference V, is given by $U=0.5QV=0.5CV^2=0.5Q^2/C$. If the charge on the plates is held constant the perpendicular force between the plates is given by $F=0.5Q^2/\varepsilon A$; while if the voltage between the plates is held constant the perpendicular force between the plates is given by $F=0.5\varepsilon AV^2/d^2$. The work done against the electrostatic force induces the plates move relative to each other and provides the energy conversion from mechanical to electrical. The diagrams of electrostatic energy harvesters can be classified into three types, which are in-plane overlap varying [65-67], in-plane gap closing [68], and out-or-plane gap closing [69], as shown in Fig. 1.6.

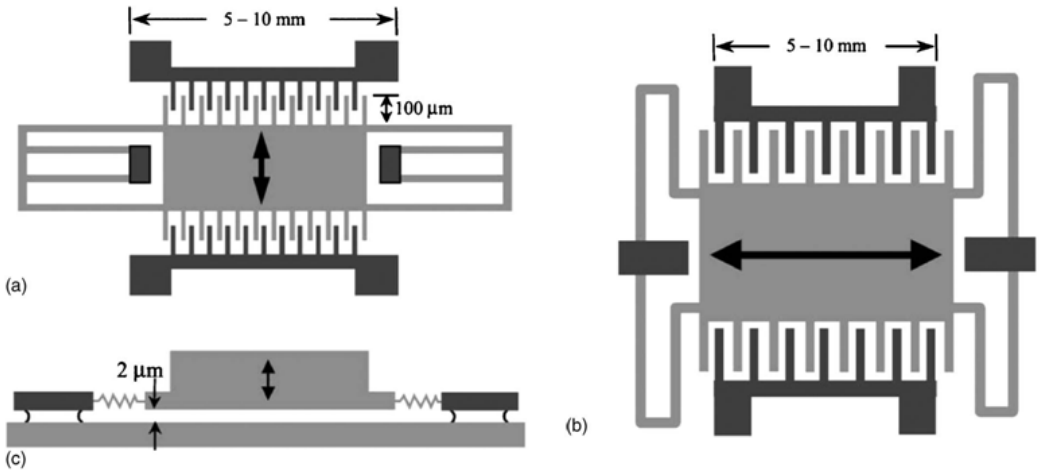

Figure 1.6 Three diagrams for electrostatic energy harvesters (a) In-plane overlap-varying; (b) In-plane gap-closing; (c) Out-of-plane gap-closing.

At present, an in-plane, overlap varying configuration has been widely used since the first electret energy harvester reported by Boland et al. [70]. An electret is an insulating material that exhibits a net electrical charge or dipole moment, which can be used to provide a biasing electric field. As illustrated in Fig. 1.7, when an electret-coated insulating rotor moves from (a), (b) to (c), the final equilibrium image charges on the left electrode decrease and those on the right electrode increase. Thus a net current flows from the left electrode through the load to the right electrodes. When the

rotor moves from (c), (b) to (a), the current reverses and thus completes a power generation cycle. In fact, a wide variety of electret materials for energy harvesting have been investigated by different groups, such as Teflon AF [70], CYTOP [71-75], SiO_2/Si_3Ni_4 [76,77], SiO_2 [78,79], and Paralyne HT [80] electret.

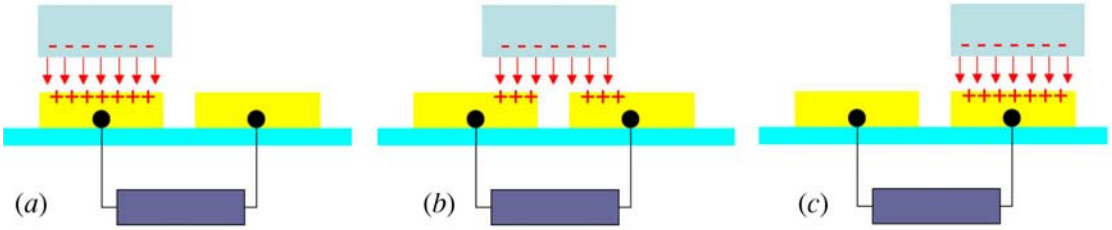

Figure 1.7 Illustration of power generation from an electrets energy harvester [80].

Table 1.4 summarizes the performance of the reviewed electrostatic/electret energy harvesters in terms of active area (cm^3), electrets potential/bias (V), resonant frequency (Hz), input acceleration (m/s^2), power (μW) and power density ($\mu W/cm^2$). The output power of the harvesters vary from less several to tens of micro-watts. Some even reach hundreds of micro-watts level. While the power densities are in a range of several to tens of micro-watts per square centimeter. At present, electrets energy harvesters attract much more attentions than conventional electrostatic prototypes since electrets can be used to provide a biasing electric field eliminating an additional charged bias.

1.2.4 Summary of energy conversion mechanisms

Piezoelectric energy conversion offers a simple way to convert structural vibration directly into voltage output by using piezoelectric material. Complex geometries and large numbers of additional components are not necessary in the design. There is a wide variety of piezoelectric materials available for different application scenarios. One major advantage is that this transduction mechanism is readily achievable to

microfabrication, since several processes exist for depositing piezoelectric thin and thick films. Piezoelectric energy harvesting is capable of producing relatively high output voltages but only at low electrical currents. Some weak points are the piezoelectric materials are required to be strained directly and therefore the performance and lifetime will be limited by their mechanical properties. Also the conversion efficiency is limited by the material property and the piezoelectric impedance is typically very high (>100 kΩ).

Electromagnetic energy conversion is a well-established technique and has been used for many years in a variety of electrical generators. There are various spring/mass configurations that can be used with many types of material that are well suited and proven in cyclically stressed applications. Relatively high output current levels are achievable at the expense of low output voltages (typically <1 V). High-performance bulk magnets and multi-turn, macro-scale coils are easily available. However, wafer-scale systems are quite difficult to achieve due to the relatively poor properties of planar magnets, the limitations on the number of loops achievable with planar coils and the restricted amplitude of vibrations. In addition, there are also problems associated with the assembly and alignment of sub-millimeter scale electromagnetic systems.

The electrostatic energy conversion can be easily realizable as a MEMS energy harvester. Energy density of the harvester can be increased by decreasing the capacitor spacing and increasing the capacitor overlapping surface area. High transduction damping, at low frequencies, can be achieved by incorporating small capacitor gap and high polarizing voltage. Unfortunately, an electrostatic energy harvester requires an initial polarizing voltage or charge, which may require the incorporation of a battery into the power system. In recent few years, researchers

utilize electrets to provide the initial charge and the electrets are capable of storing charge for many years. The output impedance of the harvester is often very high which makes them less suitable as a power supply. Parasitic capacitance structure of the device may sometimes lead to reduced energy efficiency and there is a risk of capacitor electrodes shorting or of 'stiction' in wafer-scale implementations.

The above discussion states a primarily qualitative comparison of the three approaches of energy conversion. Each of the energy conversion mechanisms described has its own advantages and disadvantages and they are summarized in Table 1.5. Because piezoelectric and electromagnetic mechanisms provides relatively high energy conversion coefficients and easy to be implemented, a detailed study based on these two mechanisms has been performed by the author.

Table 1.5 Summary of three energy conversion mechanisms

Type	Advantages	Disadvantages
Piezoelectric	1. Easy implementation and simple configuration; 2. Various piezoelectric materials available; 3. Microfabrication achievable; 4. High output voltage but low electrical current; 5. High energy density.	1. Energy conversion efficiency and lifetime is limited by the mechanical properties of the piezoelectric materials; 2. High piezoelectric impedance of the materials.
Electromagnetic	1. Various spring/mass configurations; 2. Bulk magnet and macro-scale coils are easily achievable; 3. High electrical current but low output voltage.	Poor property of the planer magnet, limitations of coil loops and restriction of the relative movement between magnet and coils in a micro system;
Electrostatic	1. Easily integrated with microsystems; 2. Electrets to be utilized to store and provide the initial charge.	1. Require an initial polarizing voltage or charge; 2. Mechanical stopper is needed to avoid electrode shorting of the capacitors.

Table 1.2 Summary of macro/micro piezoelectric energy harvesters

Reference	Device	Volume (cm^3)	Freq. (Hz)	Acc. (m/s^2)	Power (μW)	Power density ($\mu W/cm^3$)
White [37,38] University of Southampton	Steel/screen printed PZT	0.125	80	2.3	2.1	16.8
Roundy [35] UC Berkeley	Brass/PZT/tungsten bimorph	1	120	2.5	375	375
Sodano [39] Virginia Tech	QuickPack QP40N bimporth	1.94	30	--	450	231
Fang [41] Shanghai Jiao Tong University	d_{31} PZT	0.0012	608	10	2.2	1800
Shen [42] Auburn University	d_{31} PZT	0.0027	461	20	2.15	796.3
Renaud [43] IMEC	d_{31} PZT	0.03	1800	23	40	1333
Jeon [44] MIT	d_{33} PZT	0.0002	13900	110	1	5000
Lee [45] National Taiwan University	d_{31} PZT	0.0026	256	20	2.1	807.7
	d_{33} PZT	0.0028	214	20	1.3	464.3
Park [46] Kwangwoon University	d_{33} PZT	0.001	528	3.9	1.1	1100
Marzencki [47] TIMA, France	d_{31} AlN	0.0005	1495	20	0.8	1600
Elfrink [48] IMEC	d_{31} AlN	0.017	572	20	60	3529
Yen [49] UC Berkeley	d_{31} AlN	0.0016	853	10	0.17	106.25
Xu [50] DTU	Screen printed PZT thick bimorph	0.06	330	10	7.35	122.5
Aktakka [51] University of Michigan	Thinned PZT Tungsten mass	0.0487	154	15	205	4210
	Thinned PZT Si mass	0.0487	415	15	160.8	3302

Table 1.3 Summary of macro/micro electromagnetic energy harvesters

Reference	Device	Volume (cm^3)	Freq. (Hz)	Acc. (m/s^2)	Power (μW)	Power density ($\mu W/cm^3$)
Shearwood et al. [53] Sheffield University	SmCo magnet, polyimide membrane, planar gold coil, GaAs substrate	0.005	4400	380	0.3	60
Serre et al. [55] Universitat de Barcelona,	Magnet stuck on a Kapton membrane, micromachine coil	1.35	382	29	55	40
El-hami et al. [56] University of Southampton	Steel cantilever beam with two NdFeB magnets and copper coil	0.24	322	100	530	2200
Glynne-Jones et al. [57] University of Southampton	Steel cantilever beam with two/four magnets and copper coil	0.84	322	2.7	180	214
Beeby et al. [58] University of Southampton/ Tyndall	Steel cantilever beam with four magnets, copper coil, tungsten mass	0.15	52	0.59	46	310
Kulkarni et al. [59] Tyndall / University of Southampton	Moving NdFeB magnets in between two micro-fabricated coils	0.1	60	8.8	0.586	5.86
Ching et al. [60] Chinese University of Hong Kong	Laser-micromachined spring with magnet	1	110	95	830	830
Jiang et al. [62] Beihang / Hyogo University	Embedded micro-magnets and integrated microcoils	0.1	115	11.7	1.2e-4	0.0012
Cepnik and Wallrabe [63] IMTEK	Inplane springs multiple pairs of magnet and meandering coils	0.9	142	1	12	13.3
Wang and Arnold [64] University of Florida	PDMS diaphragms patterned with coils and magnet powder	0.014	530	9.8	2.3e-5	0.0016

Table 1.4 Summary of micro electrostatic/electret energy harvesters

Reference	**Configuration**	**Active surface (cm^2)**	**Bias/ Electret potential (V)**	**Freq. (Hz)**	**Acc. (m/s^2)**	**Power (μW)**	**Power density ($\mu W/cm^2$)**
Kloub et al. [65] IMTEK	In-plane overlapping	0.42	25	1740	10	5	11.9
Hoffmann et al. [66] HSG-IMIT	In-plane overlapping	0.3	50	1460	130	3.5	11.7
Chiu and Tseng [68] National Chiao Tung University	Gap closing	1	36	120	2.25	31	31
Tsutsumino et al. [71] The University of Tokyo	In-plane CYTOP electret	2	950	20	15.8	37.7	18.9
Sakane et al. [72] Asahi Glass Co.,	In-plane CYTOP electret	4	640	20	18.9	700	175
Miki et al. [73] The University of Tokyo	In-plane CYTOP electret	3	180	63	31.3	1	0.33
Suzuki et al. [74] The University of Tokyo	In-plane CYTOP electret	4	180	63	20	1	0.25
Masaki et al. [75] OMRON Corp.	In-plane CYTOP electret	4	700	30	1.5	100	25
Halvorsen et al. [76] Vestfold University College	In-plane SiO_2/Si_3N_4 electret	0.48	--	596	78.5	1	2.1
Yang et al. [77] Peking University	In-plane SiO_2/Si_3N_4 electret	5	500	20	7	5.9	1.2
Y Naruse et al. [78] SANYO Electric Co.	In-plane SiO_2 electret	9	--	2	7.9	40	4.4
Lo and Tai [80] California Institute of Technology	In-plane Parylene-HT electrets Non-resonant	30	204	50	575.8	18	0.6

1.3 State-of-the-art Technology and Problems

Conversion of vibrational energy to electrical energy is desired to target commonly occurring vibrational energy sources in typical office buildings, manufacturing and industrial environments, military devices, transportations, household appliances and human bodies. The characteristics of a wide variety of vibration sources have been studied by many groups [81-84]. Reilly et al. [85] have studied a variety of notable vibrations that occur in common environments as shown in Table 1.6. The characteristics of vibrational energy sources can be organized and represented in the table as follows: bb - broadband, i - impact (<1 Hz), lf - low frequency (<10 Hz), s - resonant spike. It is noted that, in most cases, the dominant frequencies of the ambient vibration sources are relatively low (generally less than 200 Hz). The acceleration magnitudes are also lower than 10 m/s^2 in most cases. The general vibration characteristics are resonant spike and broadband types and it is common to get resultant of 2 or 3 axes spikes of the same frequency. Recently, a survey of ambient vibration sources in the machine room of a large building was conducted by Miller et al.. [86]. The results indicate that the dominant frequency peaks from the majority of the vibration sources surveyed lie between 20 to 60 Hz, with another set of frequencies lying between 120 to 140 Hz. The accelerations of the ambient vibrations were all below 0.7 g $Hz^{-1/2}$, with most accelerations on the order of 10^{-2}-10^{-1} g $Hz^{-1/2}$. These findings are consistent with the other surveys.

Though environmental vibrations are ubiquitous and sufficient to be scavenged, the practical application of vibration-based energy harvesters is limited by the following factors. Firstly the ambient available vibrations are at low frequencies, and most of generated amplitudes from these vibrational energy sources are small due to

small acceleration available, secondly different vibration sources provide different frequencies and amplitudes, and finally vibrations from different sources normally contain various cyclic movements in different directions. The detailed discussions are as follows.

1.3.1 Vibrations at low frequencies

For a conventional resonant-based energy harvester, it is desirable to match the resonant frequency of the device to the ambient vibration frequency for achieving high energy conversion efficiency. According to the survey above, the fundamental frequencies of common vibration sources are typically less than 200 Hz. Take common machine vibration as an example, one set of frequencies lie between 20 to 60 Hz, such as lathe splatter guard, drill press, air-compressor and refrigerator, while another set of frequencies such as laptop, washing machine, and poster printer, lie approximately between 80 to 130 Hz. With regards to human activities such as walking, running and hand shaking, the frequencies are less than 10 Hz. The acceleration levels of most vibrations are quite low and normally less than 1 g.

It is known that increasing compliant spring and bulk movable mass are required to achieve lower resonant frequency. However, due to the limitation of microfabrication and brittle properties of Si material, it becomes a great challenge to realize both small size and low resonant frequency at the same time for MEMS energy harvesters. To date most resonance-based energy harvesters, particularly MEMS energy harvesters, operate at high resonant frequencies, normally more than 100 Hz as indicated in Tables 1.2, 1.3 and 1.4. There are very few devices with resonant frequency of less than 50 Hz.

Table 1.6 Summary of several vibration sources by Reilly [85]

Vibration source	Frequency (Hz)	Acceleration (g)	Resultant of axes	Characterization
Statasys 3D printer	28.0 28.3 44.7	0.044 0.060 0.017	1 2 3	s s s
W500 Lenovo laptop	119.0 85.2 119.0 85.2	0.199 0.205 0.141 0.158	3 3 1 1	s s s s
Milwaukee cordless drill	0.2 15.2	1.080 0.363	2 2	i s
External HD	119.3 119.3	0.014 0.012	3 1	s s
Washing machine	85.0 85.0	0.314 0.287	3 1	s s
Rockwell sander	59.3 92.5	0.121 0.138	1 1	s s
Monarch lathe splatter guard	15.5 24.5	0.069 0.052	2 2	s s
Monarch lather chassis	284.0	0.144	3	bb
Delta drill press	41.3 184.8	0.407 0.172	1 2	s/bb s/bb
Delta vertical bandsaw	122.5	0.140	1	s/bb
HVAC roof	184.5 184.5	0.252 0.236	2 1	bb bb
HVAC Vent	21.8 29.0 127.3	0.469 0.344 0.214	1 1 1	bb bb bb
Driving 2002 Toyota Camry	0.2 42.8 24.0	0.210 0.022 0.073	2 1 1	i bb bb
Scraper Bike	0.2 15.0	0.091 0.062	2 1	i s/bb
Running	1.5 5.1	2.045 0.762	2 1	s/lf s/lf
Walking	1.0 3.7	0.430 0.305	3 1	s/bb/lf s/bb/lf
Portable Home Air-compressor	43.7	2.103	1	s
Refrigerator	58.7	0.018	3	s
Electric Tea Pot	241.0	0.019	2	bb
Poster Printer	92.5	0.200	3	s
Server/computer	35.3	0.016	1	s

Theoretically, the maximum power generation of a vibration-based energy harvester is strongly dependent on the external excitation frequency [34]. It increases greatly at high excitation frequencies and drops dramatically at low frequencies, as assuming the excitation frequency matches to the resonant frequency of device. Thus energy harvesters with low resonant frequencies would result in reduced power output. In order to boost the output power at low frequencies, the FUC approach has been touted as a breakthrough for converting ambient low-frequency vibrations into high-frequency self-oscillations of the device.

1.3.2 Vibrations at multiple frequencies

A key challenge for a vibration-based energy harvester is that it obtains the optimal power within a narrow frequency bandwidth near its resonant frequency. Away from the bandwidth, the power generation drops dramatically and is too low to be utilized. In fact, the dominant frequencies of most environmental vibrations exhibit multiple resonances or vary within a broadband range instead of a single resonant spike. Such examples can be found in [86]. The frequency peaks of the four vertical fan belt cage surfaces surveyed vary in a broadband range of 20 to 45 Hz, while a compressor base exhibit three frequency peaks at 29.5, 59 and 354 Hz.

However, most of the reported vibration-based energy harvesters are designed only for a particular frequency, resulting in a narrow operating bandwidth from the application aspect. If the environmental vibration frequency deviates a little from the designed frequency, the generated power would decrease rapidly. On the other hand, vibration-based energy harvesters are required to operate for different application scenarios, where the fundamental frequencies vary accordingly. As a result, energy

harvesting mechanisms which can respond to low-frequency vibrations with wideband or tunable operating range are considered to offer promising solutions.

1.3.3 Vibrations in multiple directions

Currently, most vibration-based MEMS energy harvesters are able to oscillate only in a single direction, while optimal energy harvesting requires its oscillation axis to be aligned with the dominant driving direction. However, a vibration source may present unpredictable shift of its dominant direction or exhibit several frequency peaks along different directions. For example, a Statasys 3D printer exhibits three frequency peaks of 28 (1-axis), 28.3 (2-axis) and 44.1 Hz (3-axis) along different axes as shown in Table 1.6. A W500 Lenovo laptop exhibit two frequency peaks of 85.2 and 119 Hz along both 1- and 3-axis.

A 1-D energy harvester is not able to scavenge energy from a vibration source with various directions. In the case of an isotropic vibration source, the component orthogonal to the oscillation direction of the harvesting device would be lost and inefficient harvesting is the obvious consequence. One way to overcome the restrictions of 1-D harvester is to use structure capable of resonating in two or three orthogonal directions and thus harvesting from two or three components of a vibration source.

1.4 Scope of Current Work

As shown in Fig. 1.8, the scope of current work focuses on developing vibration-based MEMS energy harvesters with wideband, FUC and multi-frequency/multi-direction mechanisms to overcome existing problems on scavenging energy from environmental vibrations of low and random frequencies, and multiple directions.

Firstly, a wideband MEMS PEH system is proposed and developed for realizing a quite low and wide operating bandwidth of 30 to 47 Hz. The proposed device is the first real MEMS device with wideband behavior by using mechanical stopper approach. To date, such low and wide operating range has not been reported for piezoelectric MEMS energy harvesters. Secondly, a piezoelectric MEMS FUC energy harvesting system is first proposed to convert a low-frequency excitation into a high-frequency self-oscillation of a piezoelectric microcantilever. The main advantage of the proposed FUC approach is that it realize not only a extremely low and wideband frequency range of 13 to 26 Hz, but also a significant power improvement. In addition, it does not require the use of extra energy or bulk magnets comparing with other reported approaches. Thirdly, to overcome the limitations of 1-D energy harvesting and scavenge energy from vibration sources of different directions, a 3-D electromagnetic MEMS energy harvester has been first developed. The device is capable of scavenging energy from out-of-plane vibrations at mode I and in-plane vibrations at modes II and III.

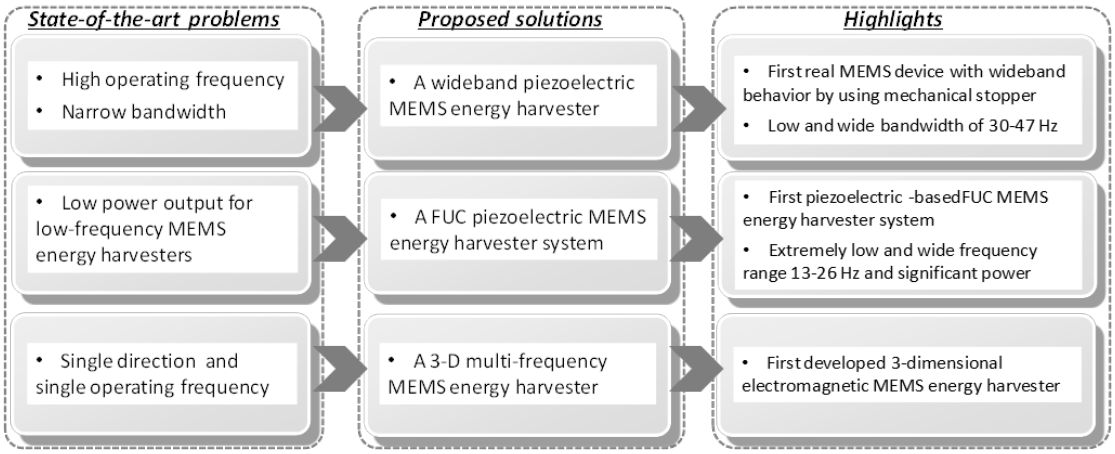

Figure 1.8 Schematics of the proposed vibration-based MEMS energy harvesters

The thesis is organized into 6 chapters. In Chapter 1, the motivation and the state-of-the-art technology and problems for vibration-based energy harvesting have

been described. The literature reviews of wideband, FUC and multi-frequency/multi-direction energy harvesters will be presented in Chapter 2. In Chapter 3, a piezoelectric MEMS energy harvester with low resonant frequency and wide operating bandwidth is designed, microfabricated, and characterized. The wideband frequency responses of the harvester with stoppers on one side and two sides are modeled. The key parameters for the frequency response, including base acceleration, damping ratio, frequency characteristic and stopper distance are investigated. Dynamic characteristics of energy harvesting are evaluated. In Chapter 4, a FUC energy harvesting cantilever triggered to self-oscillate by a periodical impact of a low-frequency energy harvesting cantilever is studied. As a result, additional power is generated by the FUC energy harvesting cantilever and power density of the system is improved significantly. In Chapter 5, a 3-D vibration-driven electromagnetic MEMS energy harvester with multiple vibration modes is investigated. The vibration behavior of the device is characterized by three vibration modes (modes I, II and III) which are perpendicular to each other, and the output performance of device is analyzed. In Chapter 6, conclusions of current study are made and recommendations for future works are discussed.

Chapter 2

Literature Review on Vibration-Based Energy Harvesters

2.1 Tunable/Wideband Vibration-Based Energy Harvesters

Tunable and wideband energy harvesters have been widely developed to increase the operating frequency range thus addressing the aforementioned frequency bandwidth limitation [87]. For frequency tuning approaches, changing the effective length [88] and the position of the gravity centre [89] are potentially suitable for intermittent tuning. However, they are not suitable for *in situ* tuning or tuning with automatic control. The frequency can be tuned intermittently or continuously by changing the spring stiffness [90-92]. However, extra systems and energy are required or sometimes has to be adjusted manually. Electrical tuning method is much easier to implement than mechanical methods [93, 94]. However, an extra closed loop system has to be introduced to control the tuning process. Bandwidth widening approaches include using a harvester array with different resonant frequencies, introducing a mechanical stopper to change the spring stiffness, and employing nonlinear or bi-stable spring structures. A detailed description of each approach is presented in the following.

1. Energy harvester array

The operating bandwidth of an energy harvester device can be widened by integrating an array of small harvesters, each of which has different dimensions and hence different resonant frequencies, as shown in Fig. 2.1. Thus the assembled system has a wide operating frequency range while the Q-factor does not decrease. The power spectrum becomes a combination of that of each individual harvester. Such integrated piezoelectric energy harvester arrays have been proposed by several groups with different cantilever dimensions and operating frequency ranges [95-98]. Sari et al.. [99, 100] reported a micromachined electromagnetic harvester, which consists of a series of cantilevers with various lengths and hence resonant frequencies. The device is able to generate 0.5 μW continuous power between 3.3 and 3.6 kHz of ambient vibration.

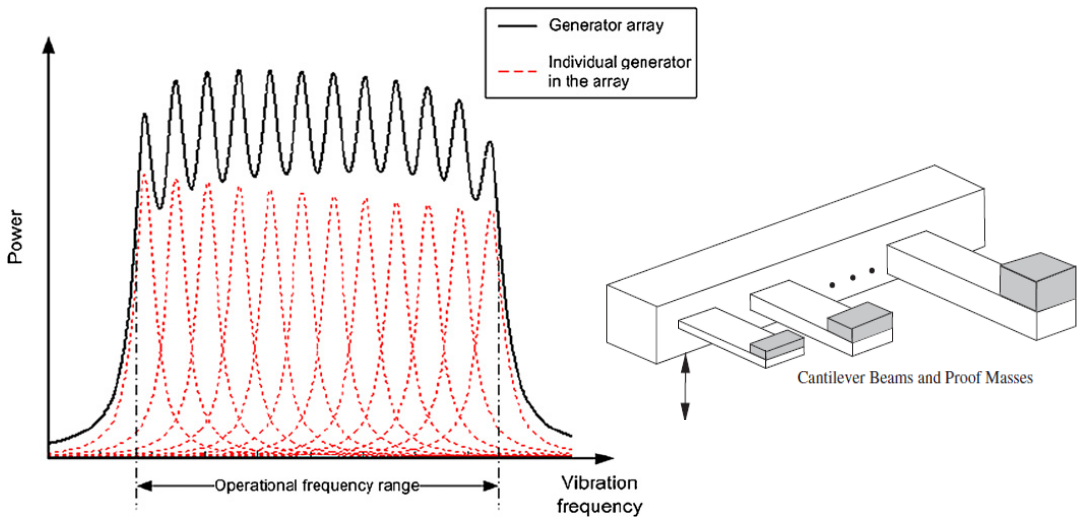

Figure 2.1 Power spectrum of an energy harvester array.

2. Mechanical stopper

Soliman et al.. [101, 102] reported another frequency widening method by using a mechanical stopper to change the spring stiffness of an electromagnetic energy

harvester (Fig. 2.2). This approach increases the bandwidth of the harvester during an up-sweep, while the bandwidth remains the same during a down-sweep. Experimental results show that the up-sweep bandwidth is 240% wider than that of the architecture without a stopper at the half-power level, but the maximum output voltage is 30% less. A piezoelectric energy harvester with a similar principle has been reported by Moss et al.. [103]. It is based on a vibro-impacting oscillator with double-sided, symmetrical, piezoelectric bimorph-stoppers. The device operates in a frequency range of 100-113 Hz and has a maximum power of 5.3 mW for base acceleration of 4.5 m/s^2.

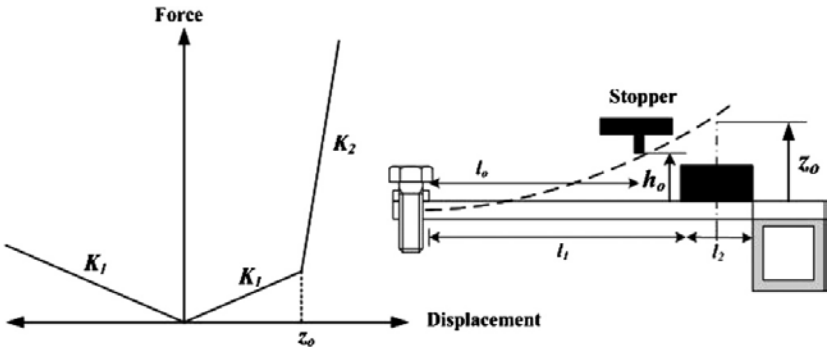

Figure 2.2 A schematic illustration of the frequency widening method by using a mechanical stopper [101].

3. Nonlinear springs by magnetic force

Nonlinear behavior of springs could offer new capabilities to capture energy available from broadband excitations. The nonlinearity efficacy of this approach has been demonstrated by the addition of magnetic reluctance forces [104-115]. Theoretically, for a hard nonlinearity, it will only produce an improvement when approaching the device resonant frequency from a lower frequency. For a soft nonlinearity, it will only produce an improvement when approaching the device resonant frequency from a higher frequency. Stanton et al.. [115] presented a nonlinear energy harvester capable of bidirectional hysteresis. By tuning nonlinear magnetic interactions, both the hardening and softening response of a power

generating piezoelectric beam with a permanent magnet is implemented as shown in Fig. 2.3.

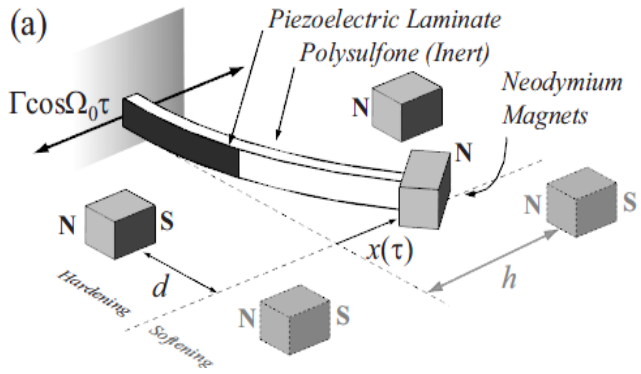

Figure 2.3 Reversible hysteresis of a broadband magnetopiezoelastic energy harvester by Stanton [115].

4. Nonlinear spring structure

Tvedt et al. [116] reported an electrostatic energy harvester utilizing nonlinear spring structures. The nonlinearity is due to the quad beam support of the proof mass which provides each beam with a clamped-guided support. Large displacements induce tensile stresses in the beams and consequently increase spring stiffness. Nguyen et al. [117, 118] reported another similar nonlinear electrostatic energy harvester with a strong softening spring effect as shown in Fig. 2.4. At a broadband random vibration of 7.0×10^{-4} g^2 Hz^{-1}, the bandwidth of the device is found to increase by more than 13 times and the average harvesting output power increases by 68% compared to that of a linear vibration energy harvester. Recently, Hajati and Kim [119] presented a wideband energy harvester by utilizing the nonlinear stiffness of a doubly clamped resonator. It is expected to have more than one order of magnitude improvement in both bandwidth (more than 20% of the peak frequency) and power density (up to 2 W/cm^3).

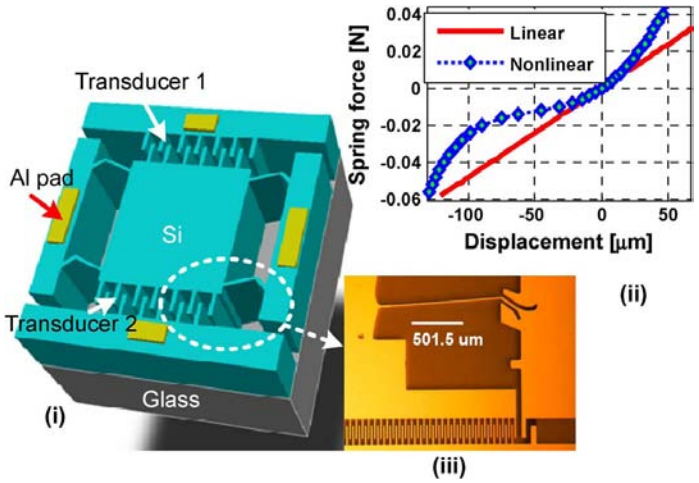

Figure 2.4 Nonlinear MEMS electrostatic energy harvester by Nguyen [118].

5. Non-resonant energy harvester

Yang et al. [120] has reported a non-resonant electromagnetic energy harvester with wide operating bandwidth. As shown in Fig. 2.5, a free-standing magnet is packaged inside a sealed hole which is composed of five pieces of printed circuit board substrates embedded with multi-layer copper coils. Output voltage of 9 mV with a bandwidth from 40 to 80 Hz is generated for input acceleration of 1.9 g. The maximum output power is measured as 0.4 μW under matched load resistance of 50 Ω.

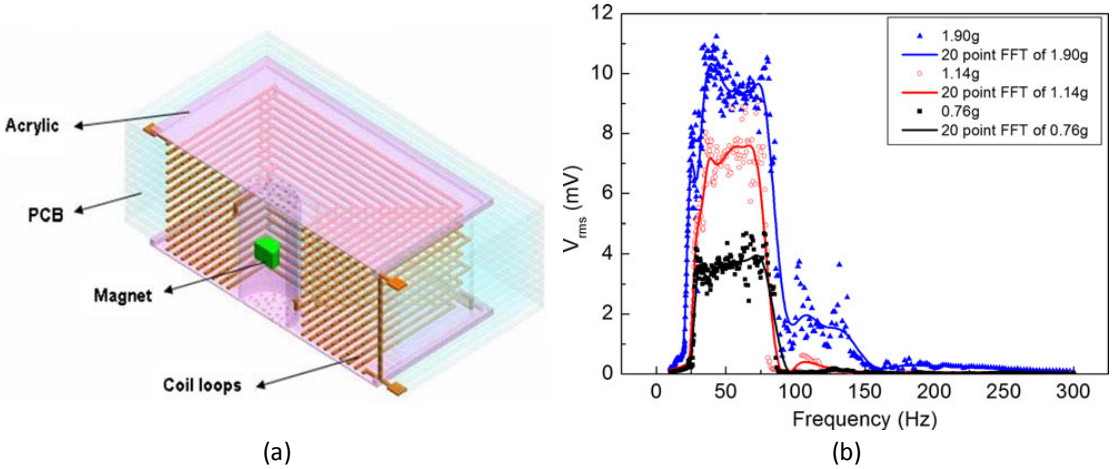

Figure 2.5 Non-resonant electromagnetic energy harvester by Yang [120].

For frequency widening approaches, there is a trade-off between the bandwidth and Q-factor. A wider bandwidth followed by a lower Q-factor will reduce the maximum output power. The operating bandwidth can be widened by designing an array of small generators, while the Q-factor does not decrease. However, at a particular vibration frequency, only a single or a few individual generators contribute to the power output and thus it is volume inefficient. The drawback of mechanical stopper approach is that it causes the maximum output power to drop by limiting the vibration amplitude. The nonlinear energy harvester by magnetic force is able to increase the operating frequency range. However, it requires additional magnets assembled around. Using nonlinear springs is a potential solution to widen the operating bandwidth. While due to the special design of the spring structure, it is difficult to achieve a low resonant frequency. Finally, the non-resonant energy harvester is not restricted by the operating frequency but is limited by a reduced output power comparing with a resonant-based energy harvester.

2.2 FUC Vibration-Based Energy Harvesters

FUC approaches have been presented by several researchers to improve the output power of the energy harvesters for low-frequency applications. The up-conversion approaches can be achieved by utilizing mechanical impact, scrape-through, bi-stable bulking and magnetic force.

1. Mechanical impact approach

The impact-based up-conversion approach for energy harvesting was initially demonstrated by Umeda et al. [121, 122], who investigated the power transformation from mechanical impact energy to electric energy by an impact of a steel ball on a

piezoelectric membrane. The operating mechanism is schematically shown in Fig. 2.6 (a). Based on the up-conversion principle, Renaud et al. [123] and Manla et al. [124] demonstrated non-resonant energy harvesters driven by the repeated impact of a free ball on two piezoelectric plates.

Gu and Livermore [125, 126] reported an impact-driven, resonant, FUC energy harvester using two beams. One is a low frequency driving beam integrated with a proof mass; the other is a short piezoelectric generating beam with a high resonant frequency. As shown in Fig. 2.6 (b), when the driving beam impacts the generating beam, the generating beam is periodically oscillated at its high resonant frequency and produced electrical power. Experimentally, an average power output of 0.43 mW is achieved under 0.4 g acceleration at 8.2 Hz, which are respectively 4.8 times and 13 times higher than those of a conventional energy harvester from a low frequency beam alone.

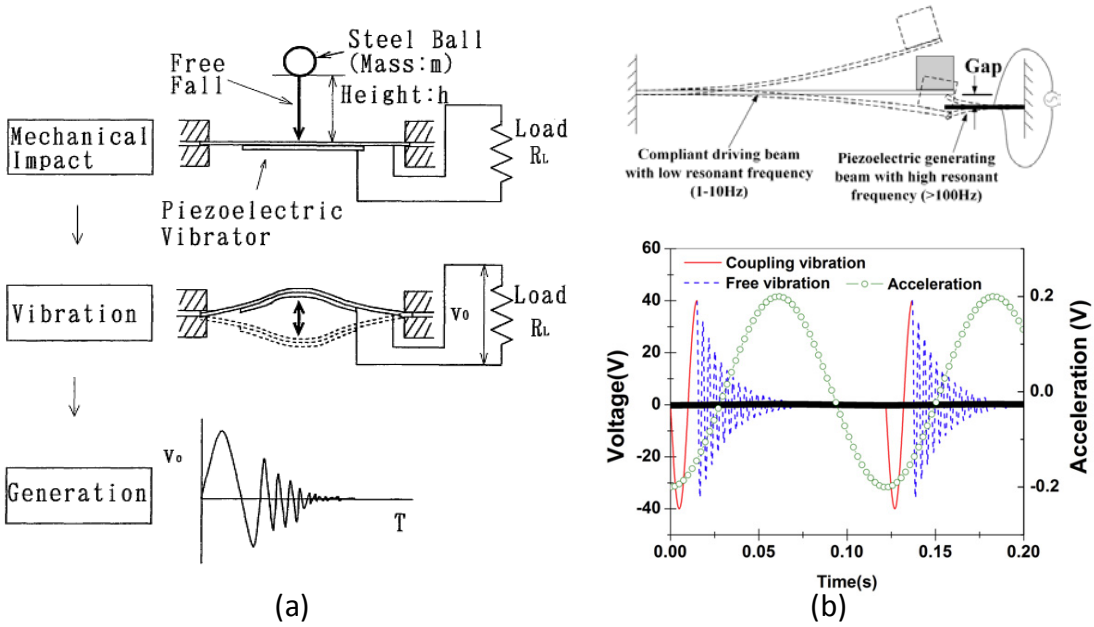

Figure 2.6 Operating mechanisms of (a) an impact of a steel ball on a piezoelectric membrane by Umeda [121] and (b) an impact-driven, resonant, FUC energy harvester by Gu and Livermore [125].

2. Scrape-through approach

Lee et al. [127] demonstrated an FUC approach realized by mechanical scrape-through contact between the tip of a piezoelectric harvesting beam and a set of superelastic ridges that slide past the tip of the harvesting beam (in Fig. 2.7 (a)). The amount of a generated voltage depends on the depth of a ridge and the rectification of FUC is a function of the ridge spacing. Zorlu et al. [128] presented a FUC electromagnetic energy harvester using a mechanical scrape-through method from low-frequency vibrations as shown in Fig. 2.7 (b). The prototype consists of a polystyrene cantilever carrying a pick-up coil and a magnet placed on a diaphragm. The vibrating diaphragm would scrape through the tip of the cantilever and up-converts to the cantilever's high-frequency vibration. Such approaches have the potential to offer the benefit of resonance, but with the difficulty of fine adjusting the overlapping distance.

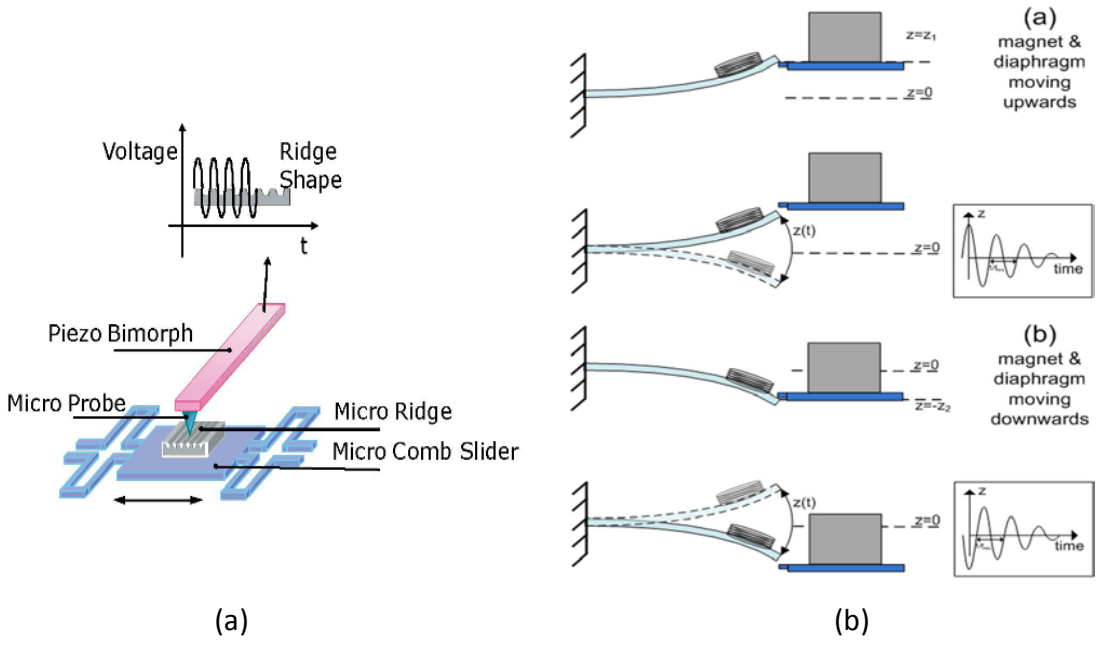

Figure 2.7 Schematic illustrations of scrape-through up-conversion approaches by (a) Lee [127] and (b) Zorlu [128].

3. Bi-stable buckling approach

A bi-stable buckling phenomenon (also known as snap-through buckling) is adapted to achieve highly efficient energy harvesting even at off-resonance conditions. Jung and Yun [129, 130] have demonstrated a bi-stable buckling up-conversion approach as shown in Fig. 2.8. The prototype consists of two prebuckled slender bridges and four cantilever beams at the center of the bridges. A piezoelectric polyvinylidene fluoride (PVDF) layer is attached on top of each beam to convert the induced strain into electrical charge. When the excitation acceleration applied to the buckled bridge exceeds a threshold value, it immediately snaps through to the other equilibrium state. The rapid transition between the two equilibrium states generates a highly accelerated impulse like excitation and thereby caused the attached cantilever beams to vibrate freely at their resonant frequencies independently.

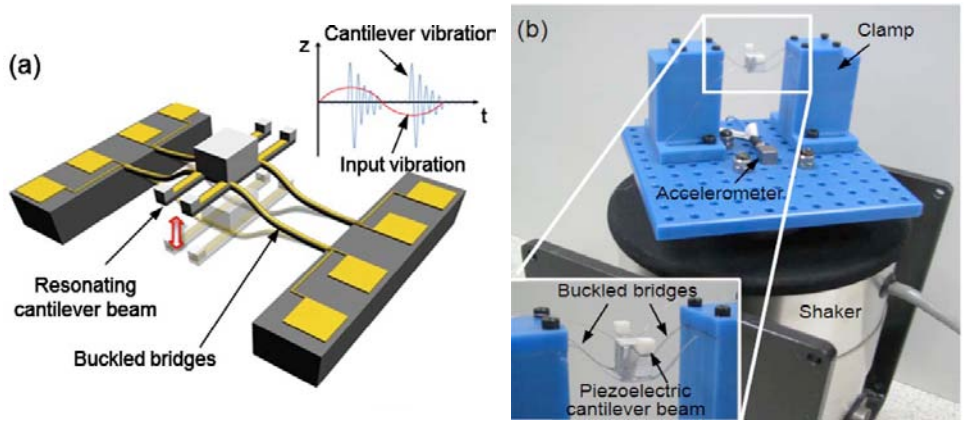

Figure 2.8 Schematic illustration and photograph of a bi-stable buckling up-conversion approach by Jung and Yun [130].

4. Magnetic force approach

Kulah and Najafi [131] demonstrated a FUC energy harvester prototype by utilizing magnetic force as schematically shown in Fig. 2.9. The prototype consists of two resonating structures. The top one is an NdFeB magnet mass suspended by a soft

diaphragm and has a low resonant frequency to match the target scenario. The bottom ones are an array of cantilever beams coated with coils and have higher resonant frequencies. As the magnet mass resonates in response to external vibration, it moves closer to the cantilevers underneath, catches it at a certain point, pulls it up, and releases it at another point. The released cantilever starts to resonate at its high resonance frequency. A similar MEMS-based electromagnetic FUC harvester was fabricated by Sari et al. [132]. The harvester has a total of 20 cantilevers. At the environment frequency range of 70-150 Hz, a voltage output of 0.57 mV and power output of 0.25 nW can be obtained from a single cantilever of the harvester.

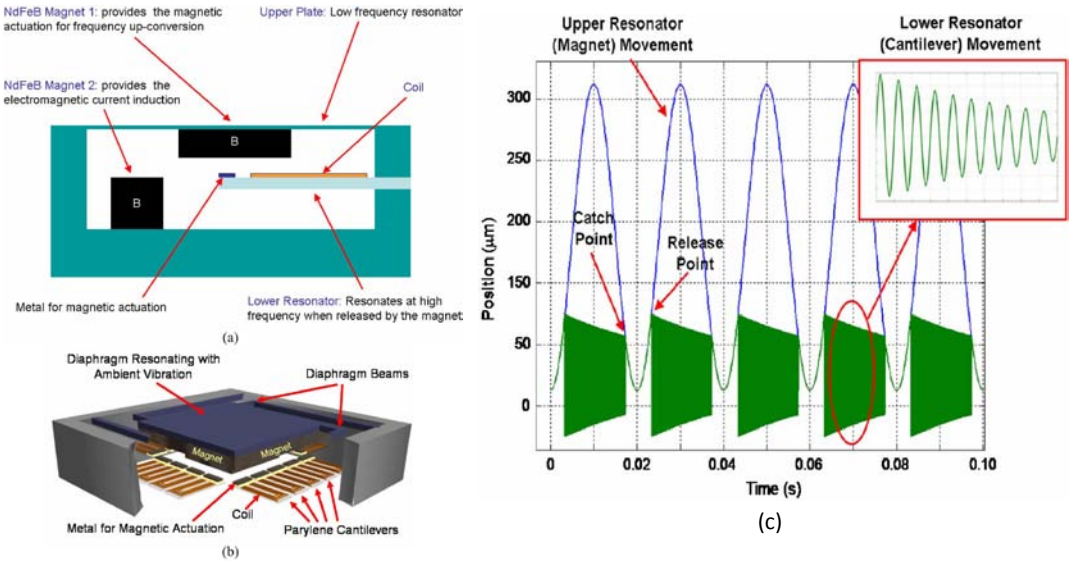

Figure 2.9 (a) Cross-section and (b) 3D view of an electromagnetic FUC harvester; (c) Movement of the low-frequency and high-frequency resonators [131].

Galchev et al. [133-135] have presented a frequency-increased generator (FIG) system by magnetic force as schematically illustrated in Fig. 2.10 (a). The driving FIG utilizes a large inertial mass to couple kinetic energy from the ambient into the structure and to pass a portion of this kinetic energy to one of two FIGs. The operation of the FIGs is outlined in Fig. 2.10 (b). The driving FIG vibrates such that the inertial mass snaps back and forth between the two generating FIGs and attached

magnetically. As the inertial mass moves, it pulls and releases the FIG. The freed FIG resonates at its high natural frequency, converting the stored mechanical energy in its spring to electrical energy. This process is then repeated in the opposite direction. Experimentally, the FIG system can generate a peak power of 163 μW and an average power of 13.6 μW from an input acceleration of 9.8 m/s^2 at 10 Hz, and it can operate at frequencies up to 65 Hz, providing it a wide operating bandwidth and versatility. Tang et al. [136, 137] have demonstrated a similar bi-stable FUC energy harvester driven by non-contact magnetic forces.

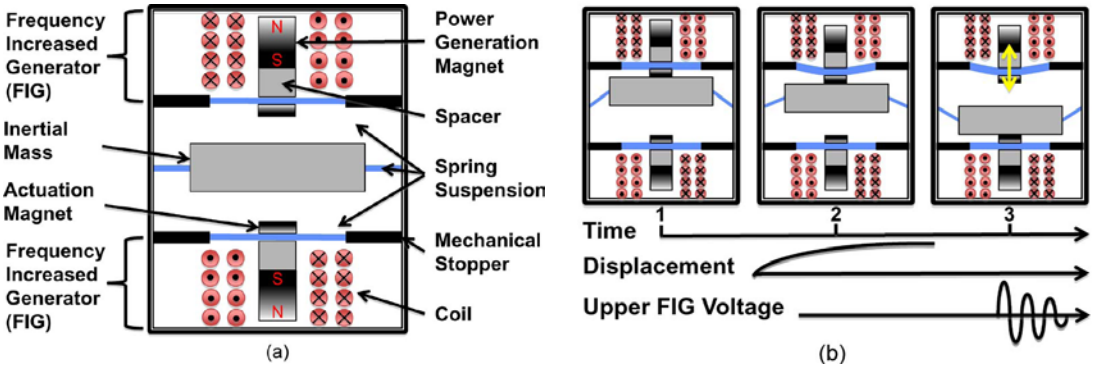

Figure 2.10 (a) FIG architecture; (b) Illustration of the operation of the FIGs [135].

All the above reviewed FUC approaches have an advantage of increasing the energy scavenged from low-frequency scenarios compared with conventional low-frequency energy harvesters, but at a cost. The mechanical impact and scrape-through approaches dissipate extra energy and may result in earlier failure in the cantilever structures. The bi-stable buckling approach requires a large acceleration to drive the buckled beam snapping from one state to the other. While the magnetic force approaches require additional bulk magnets, leading to large device volume and a complicated process of fabrication and assembly.

2.3 Multi-Frequency/Multi-Direction Energy Harvesters

2.3.1 Multi-frequency energy harvesters

Multi-frequency energy harvesters have been developed to scanvege energy from vibration sources with different frequencies. Unlike tunable or wideband energy harvesters that increase the operating range of the first resonant modal in a continuous frequency range, multi-frequency energy harvesters utilize spring-mass structures to achieve multiple resonant modals at discrete frequencies.

This concept has been reported by Ching et al. [60] as shown in Fig. 2.11. They developed an electromagnetic energy harvester using a magnetic mass attached to a circular spiral copper spring and three different resonant modes in the vertical and horizontal directions were achieved. The micro generator with a toal volume of 1 cm^3 around is capable of produce a maximum power of 830 μW with a load resistance of 1000 Ω. Berdy et al. [138] employed a meandering piezoelectric spring and a distributed proof mass to from a vibration-based energy harvester. The fabricated device features two closely spaced resonant modes at 33 and 43.3 Hz with measured RMS output power of 107.3 and 74.9 μW, respectively, for acceleration magnitude of 0.2 g. Kim et al. [139] reported a piezoelectric energy harvesting device which consisted of a rigid proof mass supported by two parallel cantilever beams. The device can utilize both translational and rotational degrees of freedoms. Therefore, it exhibits double power peaks and an increased frequency bandwidth.

Yang et al. [140] reported a multi-frequency energy harvester which consisted of three permanent magnets, three sets of two-layer copper coils and a supported beam of acrylic. In this prototype, the first, second and third resonant modes are 369, 938 and 1184 Hz, respectively. The maximum output power of the first and second modes

are 0.6 and 3.2 μW, respectively, for 14 μm exciting amplitude and 0.4 mm gap between the magnet and coils. Recently, Yang et al. [141] reported a piezoelectric generator with a nonlinear spring oscillator for providing multiple resonant modes. For the nonlinear spring of 8.3 N/m and 1 g acceleration, the maximum output power of 5, 17.83, and 23.39 μW are obtained under the resonant frequencies of 89, 104, and 130 Hz, respectively. Chew and Li [142] demonstrated a piezoelectric energy harvesting prototype using a 9 off-the-shelf beam structure which exhibits at least 7 resonant peaks in a frequency range of 100 to 1000 Hz.

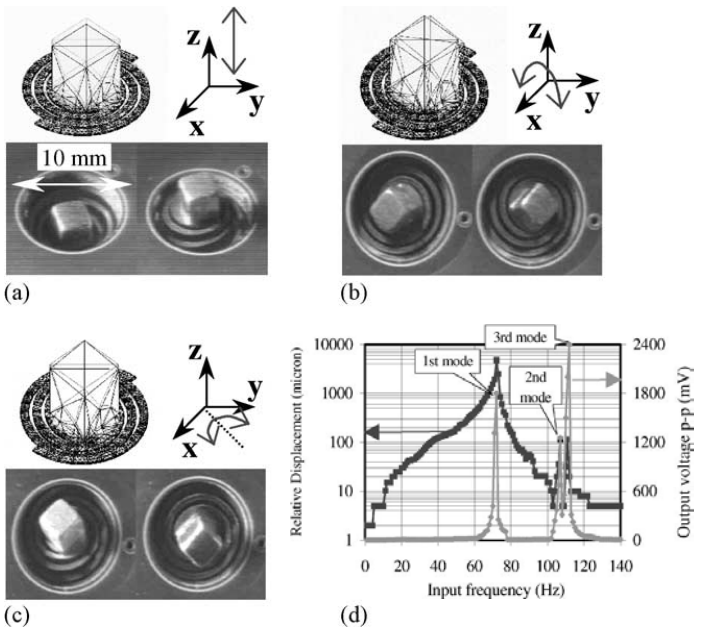

Figure 2.11 A multi-frequency electromagnetic energy harvester by Ching [60].

2.3.2 Multi-direction energy harvesters

To harvest energy from vibration sources of different directions, several electrostatic-based energy harvesters have been developed. A capacitive energy harvester with in-plane rotary combs capable of collecting kinetic energy from planar ambient vibrations was proposed by Yang et al. [143]. It includes movable and fixed combs, ladder springs, stoppers and proof mass. A maximum measured output power in air

for vibrations of 0.5 g, 1 g, 1.5 g, 2 g and 2.5 g are 0.11, 0.17, 0.24, 0.3 and 0.35 μW, respectively, when the loading resistance matches the parasitic resistance of 80 MΩ at a resonant frequency of 110 Hz.

Zhu et al. [144] introduced a 2-dimensional (2-D) MEMS ultrasonic energy harvester device. In the design, a 2 degree-of-freedoms (2-DOFs) motion mechanism has been incorporated to realize two closely spaced resonant frequencies of 38520 and 38725 Hz in x- and y- mode. When the harvester is driven by an ultrasonic transducer at a distance of 0.5 cm in the x-axis, and is biased by 60 V_{dc}, an energy harvesting capability of 21.4 nW in the x-axis is indicated. When excited along the y-axis, the harvester has an energy harvesting capacity of 22.7 nW.

Bartsch et al. [145, 146] reported a 2-D electrets-based energy harvester which was able to extract vibration energy from an arbitrary in-plane motion. The structure consists of a seismic mass suspended by a circular spring system. The surrounding spring system consists of two concentric rings connected to each other, to the seismic mass, and to the supporting substrate using nine bridges. The design of the circular rings enables two closely spaced resonance frequencies at 370.5 and 373.9 Hz along two perpendicular directions in x- and y-mode, respectively. While the level of power generated is rather low at 100 pW.

Chapter 3

A Wideband Vibration-Based MEMS Energy Harvester

The maximum power generated for a resonant-based energy harvester occurs only when the environmental vibration falls within a narrow bandwidth near its resonant frequency. Outside the bandwidth, the output power drops dramatically and is too low to be utilized. Therefore, wideband vibration-based energy harvesters are considered to be feasible in harvesting energy from irregular or random environmental vibrations. In this work, a microfabricated PEH system that can realize a quite low resonant frequency as well as a wideband operating range is proposed. The device configuration, fabrication process and assembly strategy are illustrated and mechanical modeling is discussed. Vibration measurement is performed and energy harvesting characteristics are also discussed.

3.1 Design and Fabrication

3.1.1 Working principle

Figure 3.1 illustrates a piecewise linear model of a wideband PEH system with stoppers on two sides. A low-frequency energy harvester, which is modeled as a

primary suspension system, consists of a proof mass m_0 suspended by a spring k_0 and a damper c_0. Top and bottom mechanical stoppers are considered as secondary suspension systems and are assumed to have spring stiffness of k_1 and k_2 and damping factors of c_1 and c_2, respectively. The top stopper is mounted at a distance of d_1 from the proof mass while the bottom stopper is mounted at a distance of d_2 below the proof mass. The top-stopper distance d_1 is smaller than the bottom-stopper distance d_2, i.e., $d_1<d_2$. The secondary suspension systems limit the relative movement of the mass and prevent the mass from excessive travel.

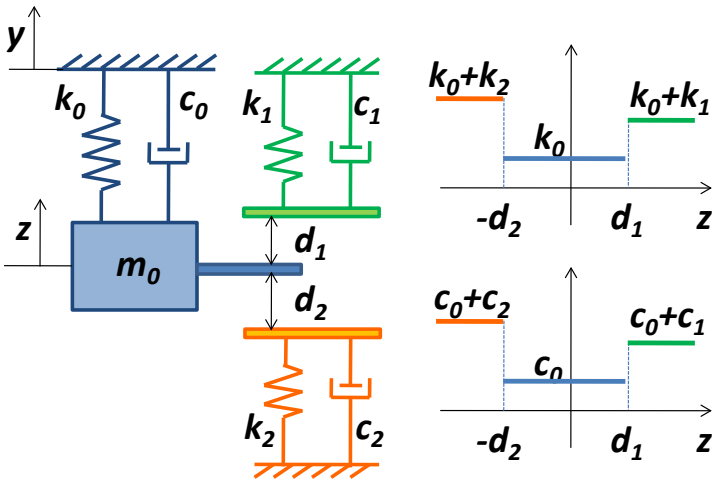

Figure 3.1 Piecewise linear model of a wideband PEH system with stoppers.

In the model, the base excitation $y(t)$ causes the proof mass to move relative to the housing $z(t)$. The motion of the proof mass can be divided into three stages. In the first stage (stage I), assuming the motion of the mass is smaller than distances d_1 and d_2, the system retains an overall stiffness and damping of k_0 and c_0, respectively. When the mass motion exceeds d_1 but is smaller than d_2, the top stopper will be engaged (stage II). The overall stiffness and damping of the system is then increased to k_0+k_1 and c_0+c_1, respectively. In the third stage (stage III), when the mass motion exceeds d_2, the top stopper as well as the bottom stopper will both be engaged. The overall stiffness and damping will then be increased to k_0+k_2 and c_0+c_2 as the

downward motion exceeds d_2 and change to k_0+k_1 and c_0+c_1 as the upward motion exceeds d_1.

3.1.2 Device configuration

The proposed wideband MEMS PEH system comprises of a low-frequency piezoelectric PZT energy harvesting cantilever (termed as PEH-L) and a high-frequency piezoelectric PZT energy harvesting cantilever (termed as PEH-H). The supporting bases of PEH-L and PEH-H are separately attached to their spacer chips and further assembled onto their metal base as shown in Fig. 3.2.

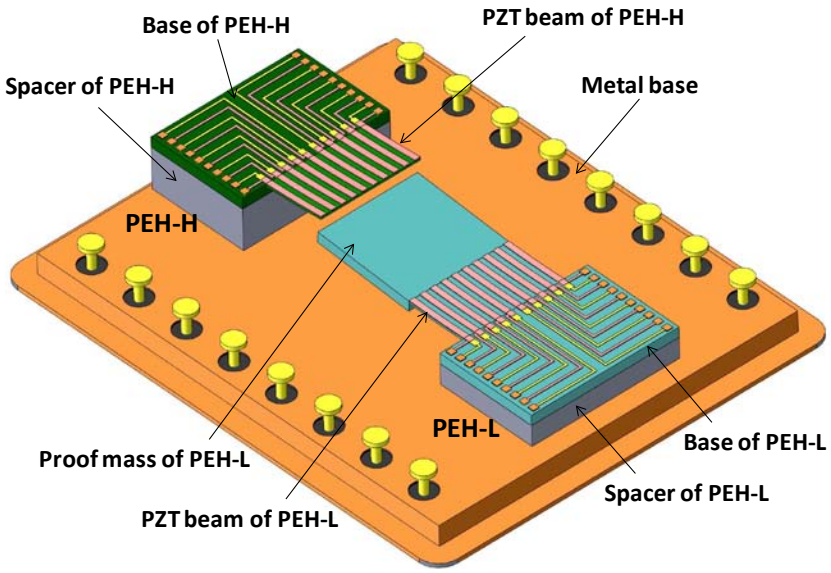

Figure 3.2 Schematic drawing of the proposed wideband PEH system with PEH-L and PEH-H assembled on a metal base.

In Fig. 3.3, PEH-L consists of a Si proof mass (5-mm-long × 5-mm-wide × 0.4-mm-thick) and a Si supporting beam (3-mm-long × 5-mm-wide × 5-μm-thick) integrated with ten parallel-arrayed PZT energy harvesting elements (hereinafter called “PZT elements”). For convenience of illustration, the PZT elements are assigned Arabic numbers from 1 to 10. The ten PZT elements are electrically isolated from one another and each PZT element consists of a top electrode layer (Ti/Pt/Ti), a

piezoelectric thin film (PZT) and a bottom electrode layer (Pt/Ti). Each of the top and bottom electrodes is connected to a bonding pad individually. The proof mass is attached to the end of the PZT beam to achieve a low resonant frequency. Likewise, PZT-H has the same beam as PEH-L but without the proof mass.

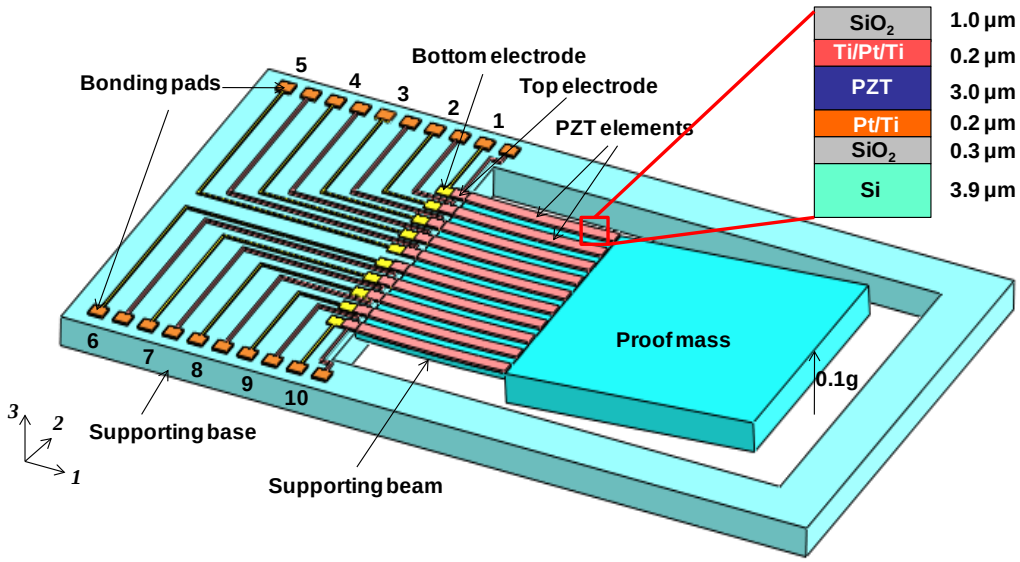

Figure 3.3 Schematic drawing of PEH-L.

Figure 3.4 illustrates the operation mechanism of the impact-based wideband PEH system. PEH-H, which acts as a top stopper, is mounted above the proof mass at a distance d_1 and a lateral overlapping length l. The distance of the proof mass from the metal base which acts as a bottom stopper is d_2. In a vibration cycle, when PEH-L is excited with sufficiently large amplitude, the proof mass will impact both the top stopper (PEH-H) and the bottom stopper (metal base). The impact results in a reduction of the vibration amplitude but broadening of the operating bandwidth of PEH-L. When the proof mass impacts the stopper, the frequency responses are altered and the effective stiffness of PEH-L increases. The increase in stiffness raises the effective resonant frequency of PEH-L and widens the frequency spectrum, while PEH-H which is impacted by proof mass would oscillate at higher frequencies. The

cyclic deformation of the PZT beams would be transformed into electricity due to piezoelectric effect.

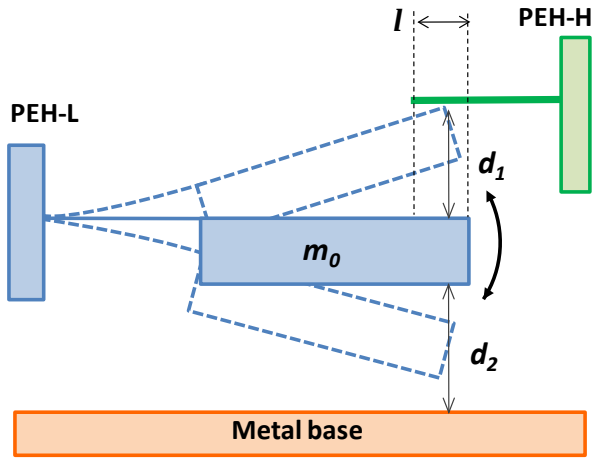

Figure 3.4 Operation mechanism of the impact-based wideband PEH system.

3.1.3 Fabrication process

The microfabrication process of the PZT cantilever begins from a Silicon-on-insulator (SOI) wafer with Si structural layer of 5 μm, buried oxide (BOX) layer of 1 μm and Si handle layer of 400 μm. As shown in Fig. 3.5 (a), the SOI wafer is first oxidized at 1100^{o}C to form a 0.3-μm-thick thermal oxide layer. After oxidation, 0.2-μm-thick Pt/Ti thin films are deposited as a bottom electrode by DC magnetron sputtering at 100^{o}C and 1.5 mTorr. A 3-μm-thick (100)-oriented PZT thin film is then deposited by sol-gel technique [147-149]. Commercially available PZT-20 solution from Kojundo Chemical Co, Japan, is used as a precursor solution. The Pb:Zr:Ti molar ratio in the precursor solution is 120:52:48. The solution is spin-coated onto the substrate at 500 rpm for 3 s, 3200 rpm for 20 s and 6000 rpm for 2 s. The deposited PZT film is dried at 120 ^{o}C for 2 min and pyrolyzed at 300^{o}C for 5 min and then crystallized by rapid thermal annealing (RTA) at 650 ^{o}C for 2 min. The spin-coating, drying, pyrolysis and RTA processes are repeated for 25 times so as to obtain the 3-μm-thick PZT film. This (100) crystallographic orientation helps in maximizing the

dielectric constant and electrical properties of the PZT film. Finally, Ti/Pt/Ti multiple layers are sputtered on top of the PZT film to form a top electrode.

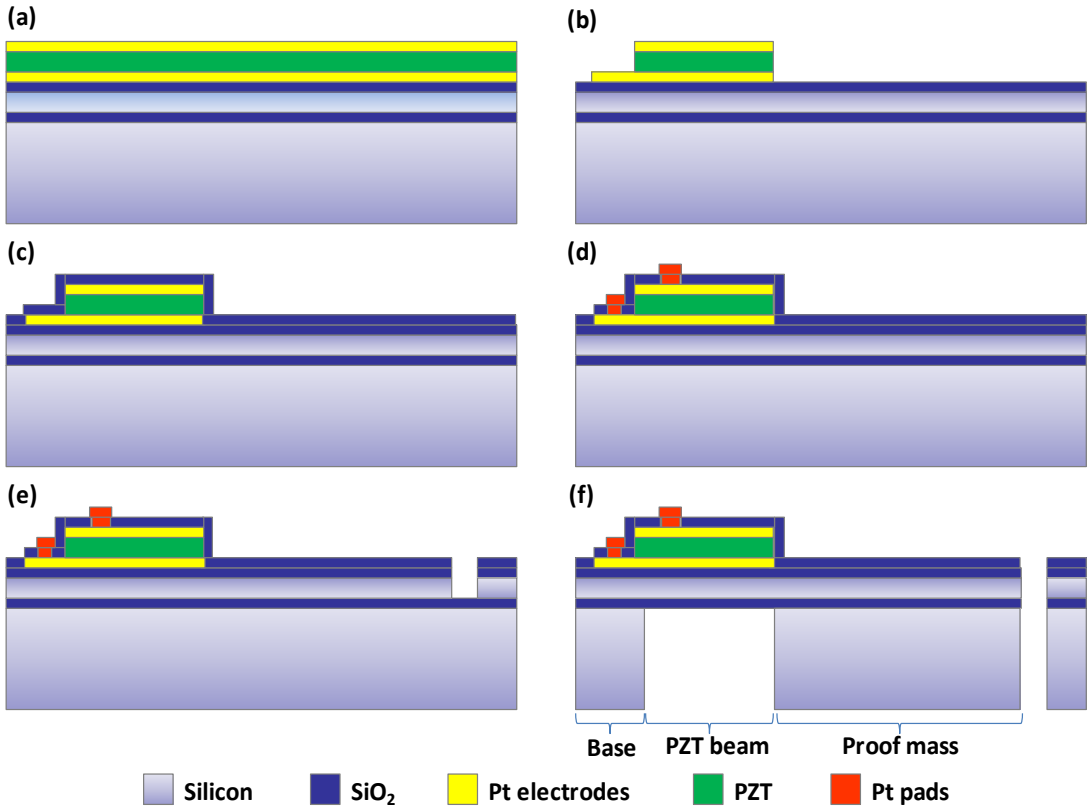

Figure 3.5 Microfabrication process of the piezoelectric PZT cantilever.

Figure 3.5 (b) shows the Ti/Pt/Ti top electrodes and Pt/Ti bottom electrodes are etched by 30 minutes 120 W Ar-ion plasma while PZT thin films are wet-etched by an solution of HF(0.9%)/HCl(8.2%)/H_2O(90.9%) and HNO_3(50%)/H_2O(50%). After etching of the Ti/Pt/Ti/PZT/Pt/Ti multilayer, a SiO_2 layer is deposited by RF-magnetron sputtering which acts as an insulation layer (Fig. 3.5 (c)). In Fig. 3.5 (d), contact holes are created on the deposited SiO_2 layer by reactive ion etching (RIE) using CHF_3 gas. Subsequently, 1-μm-thick Pt wires with Ti adhesion layer are deposited by sputtering and patterned to connect the top and bottom electrodes to bonding pads. In Fig. 3.5 (e), the thermal oxide layer, structural Si layer and buried oxide layer are etched by RIE with feed gases of CHF_3, SF_6 and CHF_3, respectively.

Finally, Fig. 3.5 (f) shows the handle Si layer and buried oxide layer are etched by deep RIE (DRIE) from the backside to release the PZT beam and proof mass structures.

The microfabricated piezoelectric PZT cantilever is assembled onto a dual in-line package (DIP) with a spacer chip, as shown in Fig. 3.6 (a) (PEH-L) and (b) (PEH-H). The gold wires are bonded from bonding pads of the chip to metal pins of the DIP. An enlarged section of the highlighted area of the boding pads on the supporting metal base is show in Fig. 3.6 (c).

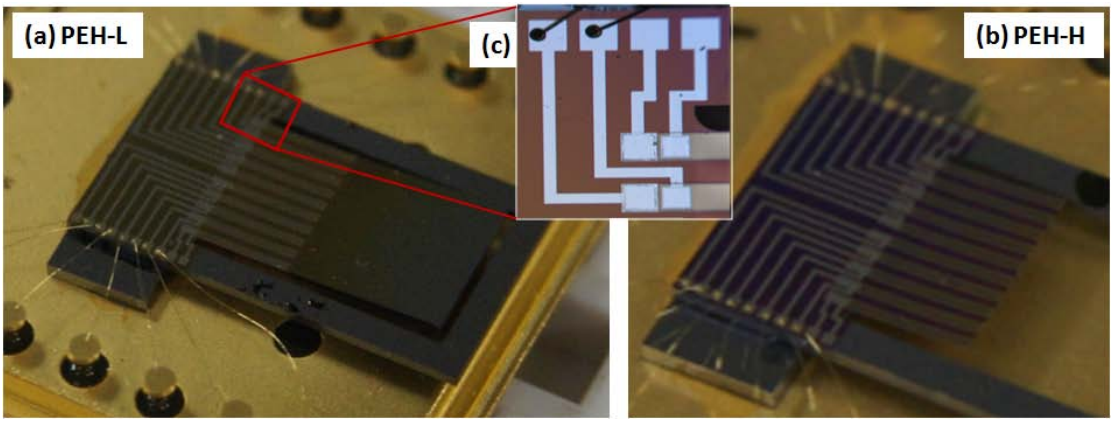

Figure 3.6 Photographs of (a) PEH-L, (b) PEH-H and (c) their bonding pads on the supporting metal base.

3.2 Modeling and Simulation

3.2.1 Output voltage and power

For a vibration-based piezoelectric cantilever operating in 3-1 mode (as seen in Fig 1.4), an applied mechanical stress σ_1 in the longitudinal direction (denoted as 1-axis) induces an electrical displacement D_3 across the piezoelectric layer, i.e., normal to the cantilever longitudinal direction (3-axis). In addition, the applied electrical field E_3 would in turn induce a mechanical strain ξ_1. The relationship between the electrical

displacement D_3 and the mechanical strain ξ_1 is given by the piezoelectric constitutive equations as

$$D_3 = \varepsilon_{33} E_3 + d_{31}\sigma_1 \tag{3.1}$$

$$\xi_1 = s_{11}\sigma_1 + d_{31} E_3 \tag{3.2}$$

where s_{11}, ε_{33} and d_{31} are the axial elastic compliance for a constant electric field, the transverse dielectric coefficient at a constant stress and the transverse-axial piezoelectric constant, respectively.

As the piezoelectric cantilever is connected to an external electric circuit and the load resistance is increased from zero to infinity, the system changes from a short to an open circuit condition. In the calculation of short-circuit current, it is assumed that $E_3 = 0$; while for the open-circuit voltage, it is assumed that $D_3 = 0$ [150]. Therefore, by having $V_{o.c.} = E_3 \cdot t_e$ and assuming a constant electric field in the thickness direction of the piezoelectric layer, the open circuit voltage generated across the piezoelectric electrodes can be obtained from $E_3 = -d_{31}\sigma_1 / \varepsilon_{33}$ and is expressed in terms of the mechanical strain distribution $\xi_1(x)$ along the PZT element as

$$V_{o.c.} = \frac{-d_{31} E t_e}{\varepsilon_{33} l_b} \int_0^{l_b} \xi_1(x) dx \tag{3.3}$$

where E is the Young's modulus of the piezoelectric material; t_e is the thickness of the piezoelectric layer; l_b is the length of the supporting beam; $\xi_1(x)$ is the strain distribution along the top surface of the supporting beam. Considering a piezoelectric cantilever with proof mass is subjected to a base acceleration, a concentrated force is assumed to be applied at the center of the proof mass. The strain distribution $\xi_1(x)$ in terms of the supporting beam tip displacement δ_b is given by

$$\xi_1(x) = \frac{3t_b}{l_b}\left(\frac{2l_b + l_m - 2x}{4l_b^2 + 3l_b l_m}\right)\delta_b \tag{3.4}$$

where x refers to the variable distance starting from the supporting beam anchor to the beam tip; l_m is the proof mass length; l_b and t_b are the supporting beam length and thickness, respectively. The detailed derivations of the strain distributions for a cantilever with proof mass are refer to [151].

The proof mass tip displacement δ_m, proof mass center displacement δ_c and supporting beam tip displacement δ_b are related by the following expressions assuming a constant slope at beam-mass connection

$$\delta_b = \frac{4l_b^2 + 3l_b l_m}{4l_b^2 + 9l_b l_m + 6l_m^2}\delta_m \tag{3.5}$$

$$\delta_b = \frac{4l_b^2 + 3l_b l_m}{4l_b^2 + 6l_b l_m + 3l_m^2}\delta_c \tag{3.6}$$

Hence, the open circuit voltages in terms of the proof mass tip displacement and proof mass center displacement are expressed as

$$V_{o.c.m} = \frac{-d_{31}Et_e}{\varepsilon_{33}l_b}\frac{3(l_b + l_m)t_b\delta_m}{4l_b^2 + 9l_b l_m + 6l_m^2} \tag{3.7}$$

$$V_{o.c.c} = \frac{-d_{31}Et_e}{\varepsilon_{33}l_b}\frac{3(l_b + l_m)t_b\delta_c}{4l_b^2 + 6l_b l_m + 3l_m^2} \tag{3.8}$$

The average power delivered to the load is

$$P_{rms} = \frac{1}{2}\frac{V_{o.c.}^2}{(Z_P + Z_L)^2}Z_L \tag{3.9}$$

where Z_P and Z_L are the complex impedance of the piezoelectric capacitor and load, respectively. The maximum power transfer occurs when the load impedance Z_L matches with the piezoelectric impedance, i.e., Z_L=Z_P. In a situation where the

connected load is real, i.e., $Z_L=R_L$, the maximum power transfer occurs when the load resistance matches with the magnitude of the piezoelectric impedance, i.e., $R_L= |Z_P|$.

3.2.2 Frequency response

3.2.2.1 Two-side stoppers

For the calculation of the frequency response, it is assumed that the mechanical stoppers are zero mass and the impact is perfectly elastic. The differential equations of mass motion of the impact-based wideband PEH system with two-side stoppers can be written as [152]

$$\begin{cases} m_0\ddot{z}+(c_0+c_1)\dot{z}+(k_0+k_1)z-k_1d_1=-m_0\ddot{y} & (z\geq d_1) \\ m_0\ddot{z}+c_0\dot{z}+k_0z=-m_0\ddot{y} & (-d_2<z<d_1) \\ m_0\ddot{z}+(c_0+c_2)\dot{z}+(k_0+k_2)z+k_2d_2=-m_0\ddot{y} & (z\leq -d_2) \end{cases} \tag{3.10}$$

Equation (3.10) can be rearranged as follows:

$$\begin{cases} \ddot{z}+(2\xi_0\omega_0+2\xi_1\omega_1)\dot{z}+(\omega_0^2+\omega_1^2)z-\omega_1^2d_1=-\ddot{y} & (z\geq d_1) \\ \ddot{z}+2\xi_0\omega_0\dot{z}+\omega_0^2z=-\ddot{y} & (-d_2<z<d_1) \\ \ddot{z}+(2\xi_0\omega_0+2\xi_2\omega_2)\dot{z}+(\omega_0^2+\omega_2^2)z+\omega_2^2d_2=-\ddot{y} & (z\leq -d_2) \end{cases} \tag{3.11}$$

where $y(t)=Y\sin(\omega t)$, Y is the amplitude of the base excitation, ω is the excitation frequency; ξ_0 and ω_0 are the primary damping and frequency characteristics, ξ_1, ξ_2 and ω_1, ω_2 are the secondary damping and frequency characteristics, which can be further defined as $2\xi_0\omega_0=\frac{c_0}{m_0}$, $2\xi_1\omega_1=\frac{c_1}{m_0}$, $2\xi_2\omega_2=\frac{c_2}{m_0}$, $\omega_0^2=\frac{k_0}{m_0}$, $\omega_1^2=\frac{k_1}{m_0}$, $\omega_2^2=\frac{k_2}{m_0}$.

To study the frequency response of the impact-based wideband PEH system, we use dimensionless variables $\tau=\omega_0 t$, $\rho=\frac{\omega}{\omega_0}$, $\rho_1=\frac{\omega_1}{\omega_0}$, $\rho_2=\frac{\omega_2}{\omega_0}$, $u=\frac{z}{Y}$,

$v = \frac{y}{Y} = \sin(\rho\tau)$, $\delta_1 = \frac{d_1}{Y}$, $\delta_2 = \frac{d_2}{Y}$ to obtain the following dimensionless equations of mass motion

$$\ddot{u} + 2\xi_0\dot{u} + u = \rho^2 \sin(\rho\tau) + f(u,\dot{u}) \tag{3.12}$$

where

$$f(u,\dot{u}) = \begin{cases} -2\rho_1\xi_1\dot{u} - \rho_1^2 u + \rho_1^2\delta_1 & (u \geq \delta_1) \\ 0 & (-\delta_2 < u < \delta_1) \\ -2\rho_2\xi_2\dot{u} - \rho_2^2 u - \rho_2^2\delta_2 & (u \leq -\delta_2) \end{cases} \tag{3.13}$$

The frequency response function, which describes the dimensionless amplitude *a* with frequency ρ, is obtained as

$$\pi^2\rho^4 = X_1^2 + X_2^2 \tag{3.14}$$

where

$$X_1 = -2\xi_0 a\rho\pi - \rho_1\xi_1 a\rho(\pi - 2\varphi_1 - \sin 2\varphi_1) - \rho_2\xi_2 a\rho(\pi - 2\varphi_2 - \sin 2\varphi_2) \tag{3.15}$$

$$\begin{aligned} X_2 = \pi a(1-\rho^2) - [&\frac{1}{2}\rho_1^2 a(2\varphi_1 - \sin 2\varphi_1 - \pi) + \frac{1}{2}\rho_2^2 a(2\varphi_2 - \sin 2\varphi_2 - \pi) \\ &+ 2\rho_1^2\delta_1\cos\varphi_1 + 2\rho_2^2\delta_2\cos\varphi_2] \end{aligned} \tag{3.16}$$

$\varphi_1 = \sin^{-1}(\delta_1/a)$ and $\varphi_2 = \sin^{-1}(\delta_2/a)$ are the phase angles when the proof mass engages the top and bottom stoppers, respectively. Detailed derivations are shown in Appendix A.

3.2.2.2 One-side stopper

When a one-side stopper is involved in the impact-based PEH system, the dimensionless differential equation of mass motion can be rewritten as

$$\ddot{u} + 2\xi_0\dot{u} + u = \rho^2 \sin(\rho\tau) + f_i(u,\dot{u}) \tag{3.17}$$

where i = 1 or 2 represents the situation where the mass motion engages either the top or the bottom stopper, respectively.

$$f_1(u,\dot{u}) = \begin{cases} -2\rho_1\xi_1\dot{u} - \rho_1^2 u + \rho_1^2\delta_1 & (u \geq \delta_1) \\ 0 & (u < \delta_1) \end{cases} \tag{3.18}$$

$$f_2(u,\dot{u}) = \begin{cases} 0 & (u > -\delta_2) \\ -2\rho_2\xi_2\dot{u} - \rho_2^2 u - \rho_2^2\delta_2 & (u \leq -\delta_2) \end{cases}$$

(3.19)

An implicit equation for the amplitude a as a function of the excitation frequency ρ is given by

$$\pi^2\rho^4 = Z_1^2 + Z_2^2 \tag{3.20}$$

where

$$Z_1 = -2\xi_0 a\rho\pi - \rho_i\xi_i a\rho(\pi - 2\varphi_i - \sin 2\varphi_i) \tag{3.21}$$

$$Z_2 = \pi a(1-\rho^2) - [\frac{1}{2}\rho_i^2 a(2\varphi_i - \sin 2\varphi_i - \pi) + 2\rho_i^2\delta_i \cos\varphi_i] \tag{3.22}$$

$\varphi_i = \sin^{-1}(\delta_i / a)$ is the phase angle when the proof mass engages the top or bottom stopper.

3.2.3 Analytical simulation

3.2.3.1 One-side stopper

In the case of where the impact-based wideband PEH system employs a one-side stopper, the frequency response can be obtained analytically using Eq. (3.20). The metal base is assumed to be the only stopper at a distance of 1 mm in the simulation and the acceleration is set at 0.4 g. The damping ratios are assumed to be $\xi_0 = 0.025$

and $\xi_2 = 0.1$. The stiffness related frequencies are $f_0 = 35.8$ Hz and $f_2 = 100$ Hz, which are obtained from $\omega = 2\pi f = \sqrt{k/m}$. From the simulated results, the frequency response of the mass motion is divided into two stages as shown in Fig. 3.7.

The mass motion initially follows the frequency response of a linear spring-mass-damper model and increases monotonically from A to B as the excitation frequency increases (Stage I). At point B, the proof mass reaches a displacement of 1 mm and starts to engage the bottom stopper, hence transforming the motion to a piecewise linear model with a one-side stopper and the frequency response follows the trace from B to C (Stage II). The overall stiffness and damping in stage II are much higher than those in stage I, thus the operating bandwidth is significantly extended beyond the original frequency bandwidth. When the excitation frequency sweeps to point C, the mass motion drops immediately to point D, and reverts to the original trace of the linear model (without stopper) in stage I. Subsequently, the mass motion decreases monotonically from D to E with up-sweeping frequencies.

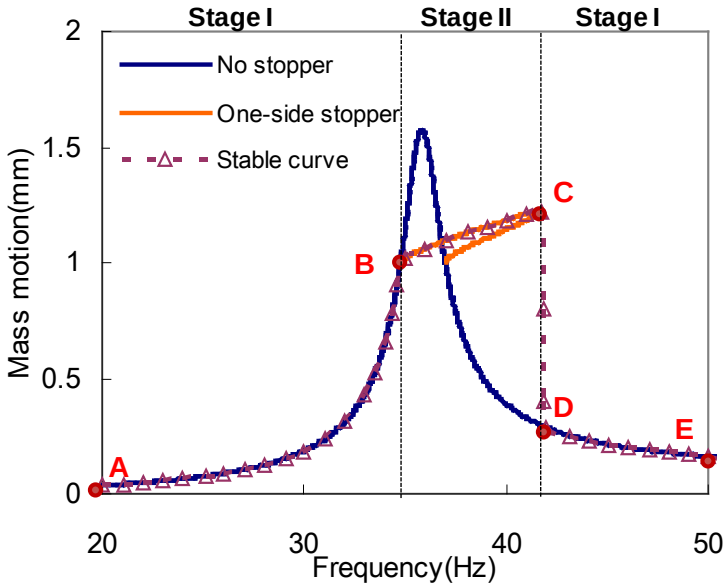

Figure 3.7 Analytical simulation of the mass motion of the PEH system against frequency with a one-side stopper.

In this model, certain parameters such as base acceleration, secondary damping ξ_2, secondary frequency characteristics ω_2 and bottom-stopper distance d_2 show strong influence on the frequency response. As shown in Fig. 3.8, each of these four parameters has been studied separately with the other parameters kept constant. Figure 3.8 (a) shows that, for constant values of ξ_2, ω_2, and d_2, the base acceleration has a strong influence on the frequency operating bandwidth. For instance, when the base acceleration increases from 0.4 g to 0.6 g, the operating bandwidth is widened from 7 to 14 Hz.

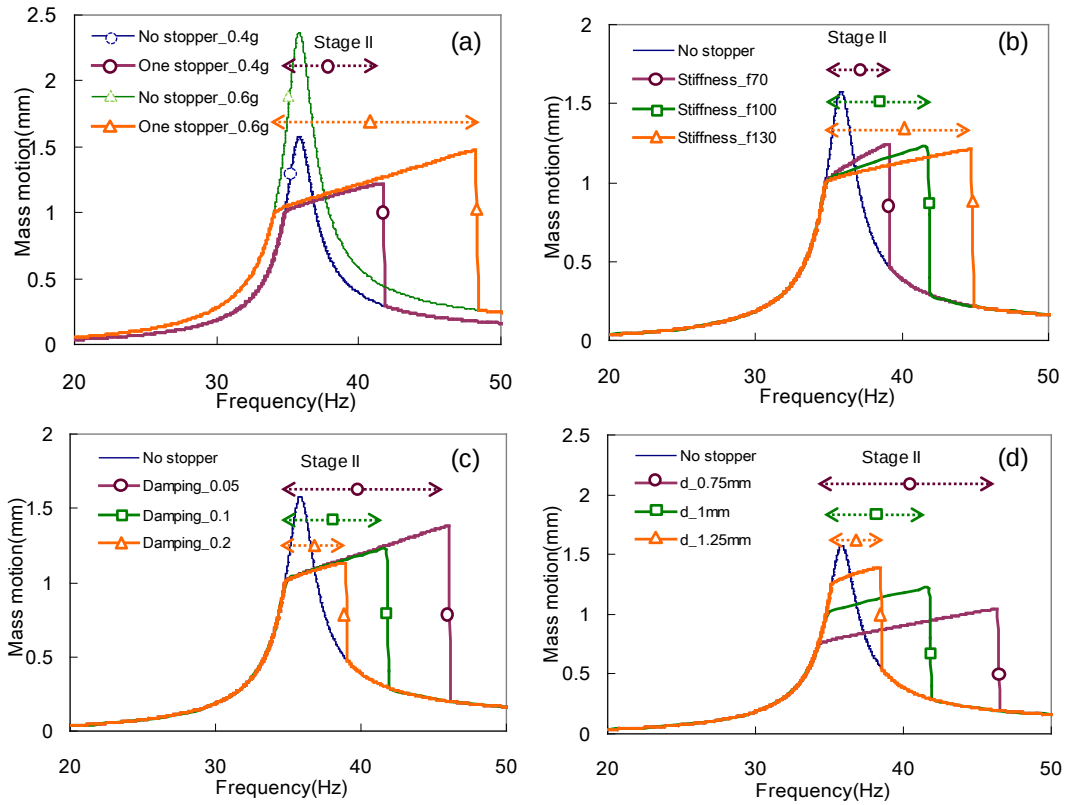

Figure 3.8 Parameter effects on the frequency response of the PEH system with a one-side stopper.

Likewise, Fig. 3.8 (b) shows the frequency response with different frequency characteristics of the bottom stopper, i.e., 70, 100 and 130 Hz. Since the frequency characteristic is related to its spring stiffness, it is seen that a higher stiffness of the bottom stopper results in a wider frequency bandwidth. However, as the stiffness

increases, the mass motion increasing rate decreases. In Fig. 3.8 (c), as the damping ratio of the bottom stopper increases from 0.05, 0.1 to 0.2, the frequency bandwidth decreases from 11, 7 to 4 Hz. Hence, a lower damping ratio is necessary to realize a wider frequency bandwidth. The frequency response with various bottom-stopper distances is shown in Fig. 3.8 (d). A lower stopper distance would result in a wider frequency bandwidth at the expense of a reduction in the mass motion.

From the above observation, it is seen that the frequency wideband increases with a decrease in the damping and an increase in stiffness of the stopper. In addition, a high base acceleration is preferred to realize a better performance (wider operating bandwidth and higher power output). There is a trade-off for the stopper distance, since it affects the frequency bandwidth and mass motion with opposite trend.

3.2.3.2 Two-side stoppers

For the impact-based wideband PEH system with two-side stoppers, the frequency response can be obtained analytically using Eqs. (3.14) and (3.20). Similarly to the one-side stopper, initially the base acceleration is set as 0.4 g. The damping ratios are assumed to be $\xi_0 = 0.025$, $\xi_1 = 0.03$, $\xi_2 = 0.1$, and the frequencies are $f_0 = 35.8$, $f_1 = 35.8$, $f_2 = 100$. The top and bottom-stopper distances are 0.5 and 1 mm, respectively.

As shown in Fig. 3.9, the mass motion of PEH-L is divided into three stages. In stage I, the mass motion follows the frequency response of a linear model and increases monotonically from A to B with up-sweeping frequency. At point B (d_1=0.5 mm), the mass starts to engage the top stopper. Hence, the mass motion transforms into a piecewise linear model with one-side stopper in Stage II. The mass motion increases gradually from point B until the proof mass impacts the bottom stopper at

point C. At this stage, the mass motion transforms into a piecewise linear model with two-side stoppers in Stage III. Since the overall stiffness and damping in stage III is higher than those in stage II, the mass motion increases slightly from C to D. At point D, the mass motion drops immediately to point E and reverts to the original trace of the linear model in stage I and subsequently the mass motion decreases monotonically to point F with up-sweeping frequencies.

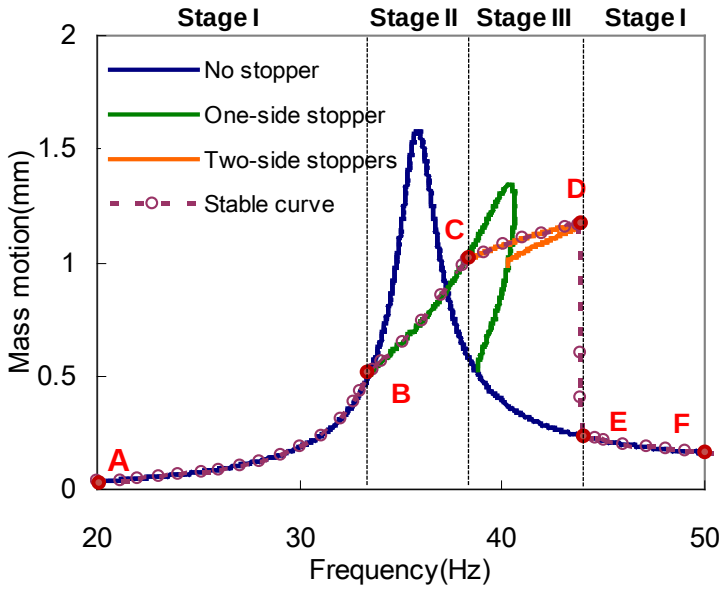

Figure 3.9 Analytical simulation of the mass motion of the PEH system against frequency with two-side stoppers.

Figure 3.10 shows the frequency response of the system with two-side stoppers for various parameters. Similarly to the one-side stopper in Fig. 3.8, one of the four parameters, such as base acceleration, top-stopper damping ratio ξ_1, top-stopper frequency characteristics f_1 and top-stopper distance d_1, is varied while the other three parameters are kept constant. Other parameters such as ξ_0, ξ_2, f_0, f_2, d_2, are also kept constant. Figure 3.10 (a) shows the frequency responses at accelerations of 0.4 g and 0.6 g. A higher base acceleration results in a wider operating bandwidth manifested mainly in stage III. In Fig. 3.10 (b), as the stiffness of the top stopper (in terms of the

frequency) increases from 35.8, 50 to 70 Hz, the operating bandwidth in stage II are broadened from 4 Hz (34-38 Hz), 7 Hz (34-41 Hz) to 13 Hz (34-47Hz), respectively. While the starting frequencies of the operating bandwidth in stage III are shifted accordingly from the ending frequencies in stage II, i.e., 38, 41 and 47 Hz. Fig. 3.10 (c) shows that the lower the damping of the top stopper, the wider the operating bandwidth as reflected in stage III. Fig. 3.10 (d) shows the frequency response of different top-stopper distances. As can be seen, a smaller stopper distance results in a wider operating bandwidth in stage II and a shift of the stage III operating bandwidth to a higher frequency range. A higher stiffness and a larger stopper distance will cause a larger bandwidth shift in stage III. In addition, a higher base acceleration and a lower damping ratio will result in a larger operating bandwidth and mass motion.

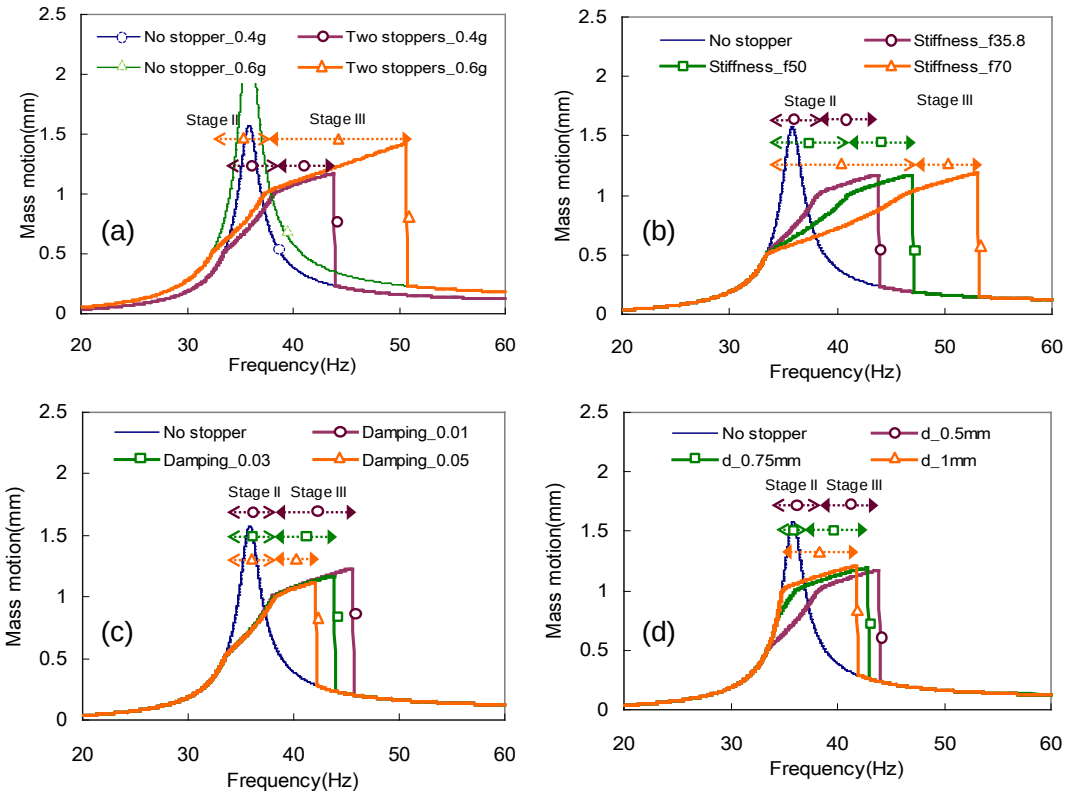

Figure 3.10 Parameter effects on the frequency response of the PEH system with two-side stoppers.

3.3 Experimental Work and Discussion

3.3.1 Configuration I – One-side stopper

3.3.1.1 Experimental setup

The vibration testing system for configuration I consists of an electromagnetic shaker, a power amplifier, a dynamic signal analyzer (DSA), an accelerometer and its controller as shown in Fig. 3.11. The packaged PEH-L is mounted onto a printed circuit board (PCB) and attached together with an accelerometer onto a shaker. The vibration frequency and amplitude of the shaker are controlled by a DSA through an amplifier with a sinusoidal signal input. The output voltage of PEH-L is recorded via the DSA through channel 1. The acceleration signal is collected via channel 2 and recorded to the DSA through the acceleration controller.

Figure 3.12 shows an equivalent voltage measurement circuit of one PZT element of PEH-L which is connected to the DSA. The PZT element can be considered as an AC voltage source V_S connected in series with a piezoelectric impedance Z_P. The piezoelectric impedance Z_P is measured to be a capacitance C_P of 2.2 nF and a resistance R_P of 67.2 MΩ connected in parallel. The input impedance Z_L of the DSA, which has an equivalent load resistance R_L of 1 MΩ is lower than the magnitude of the piezoelectric impedance $|Z_P|$. Therefore, the output voltage detected by the DSA is not the open circuit voltage V_S of the PZT element, but the load voltage V_L on the resistance R_L of the DSA.

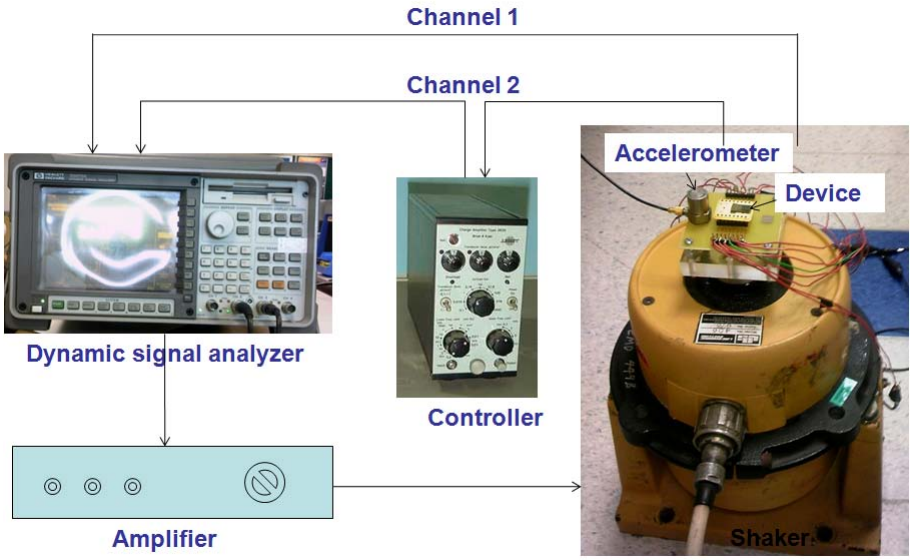

Figure 3.11 Vibration testing system for configuration I.

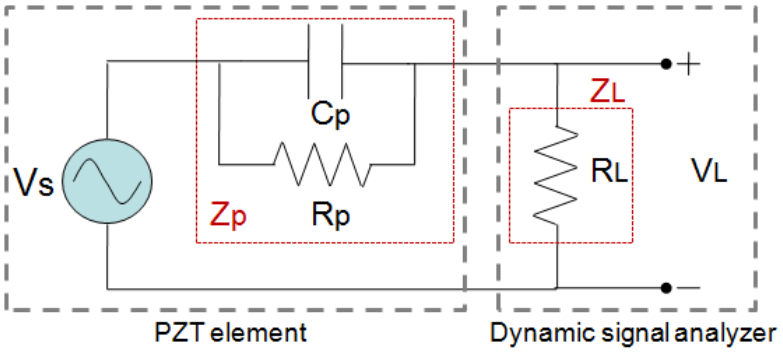

Figure 3.12 Equivalent voltage measurement circuit for one PZT element of PEH-L connected to the DSA.

To accurately characterize the vibration behavior of configuration I, an optical method as shown in Fig. 3.13 is deployed. The optical measurement setup consists of a function generator, a DSA, a laser source with an angle adjustable tripod. Since PEH-L contains 10 PZT elements, some PZT elements are used as PZT actuators, while the others are used as PZT harvesters. As the PZT actuators are excited by an AC voltage, PEH-L will start to oscillate first. Subsequently, the PZT harvesters will generate electrical current due to self-oscillation of PEH-L.

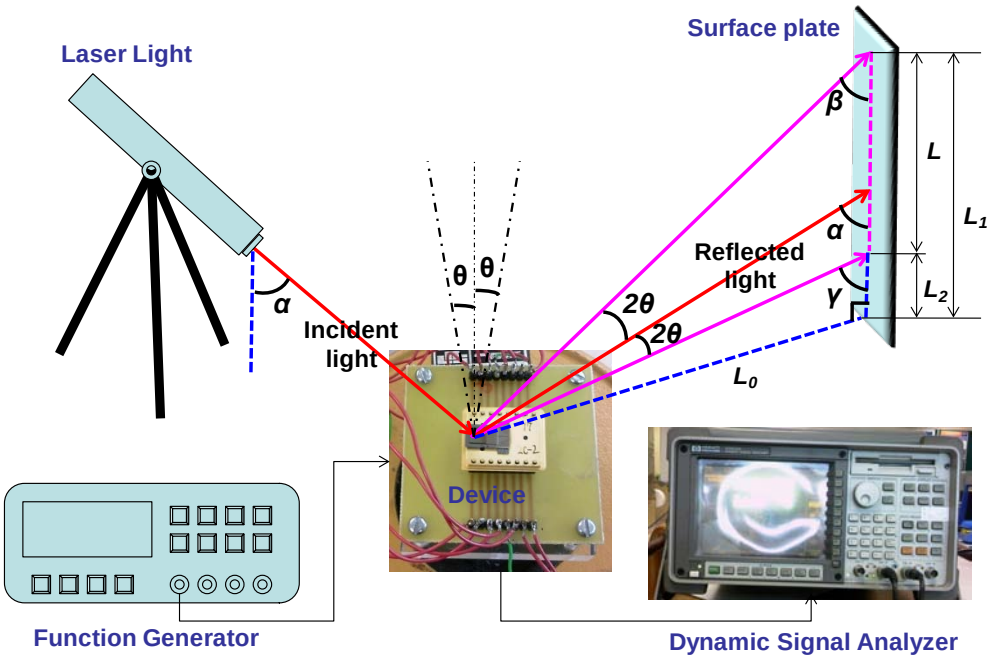

Figure 3.13 Optical setup for the measurement of mass tip displacement for configuration I.

The bending angle of the cantilever is derived from the sweeping distance of the reflected light on the surface plate. Hence, to calculate the relationship, the cantilever is initially flat and the radius of curvature of the bending is assumed constant. The incident light illuminates the mass surface at a fixed angle α and is reflected on a surface with the same angle. In a vibration cycle, when the cantilever rotates by an angle of θ, and the reflected light would rotate by an angle of 2θ. The maximum sweeping distance L transverse along the plate surface is expressed as

$$L = L_1 - L_2 = \frac{L_0}{\tan(\beta)} - \frac{L_0}{\tan(\gamma)} \tag{3.23}$$

where angles β and γ are related to the incident angle α and deflection angle θ by $\beta = \alpha - 2\theta$ and $\gamma = \alpha + 2\theta$. L_0 is the perpendicular distance between the cantilever and plate surface. The relationship between deflection angle of the cantilever and sweeping distance is express as

$$L = L_0\left[\frac{1}{\tan(\alpha - 2\theta)} - \frac{1}{\tan(\alpha + 2\theta)}\right] \tag{3.24}$$

From the deflection angle, the displacement of the proof mass tip δ_m is given by

$$\delta_m = l_b(1-\cos\theta)/\sin\theta + l_m \sin\theta \tag{3.25}$$

3.3.1.2 Energy harvesting characteristics

The vibration testing system as shown in Fig. 3.11 is used to characterize the energy harvesting performance of configuration I. PEH-L is assembled onto a PCB board and six of the ten PZT elements are individually connected to the DSA for load voltage measurement. The vibration frequency of the shaker sweeps from 20 Hz to 50 Hz, and the load voltages generated from each PZT element are recorded by the DSA.

Figure 3.14 (a) shows the variation of the load rms voltages of No. 6 PZT element against vibration frequencies at different input accelerations ranging from 0.1 to 1.0 g. It is found that at a low input acceleration of 0.1 g, the maximum load rms voltage of 27 mV is generated at a low resonant frequency of 36 Hz. As the input acceleration increases more than 0.2 g, the load rms voltage is suppressed but the operating frequency is extended to a wider bandwidth. The higher input acceleration, the wider bandwidth of the operating frequency. Other PZT elements show similar trend. Figure 3.14 (b) shows that the load rms voltages fluctuate for each of the PZT element at acceleration of 0.1 and 0.2 g. The average load rms voltages are 37 and 50 mV at acceleration of 0.1 and 0.2 g, respectively. Because these ten PZT elements experience similar induced strain in each vibrate cycle, they should exhibit similar voltage output. The variation in the output could be due to the small variation of the PZT dimensions and properties.

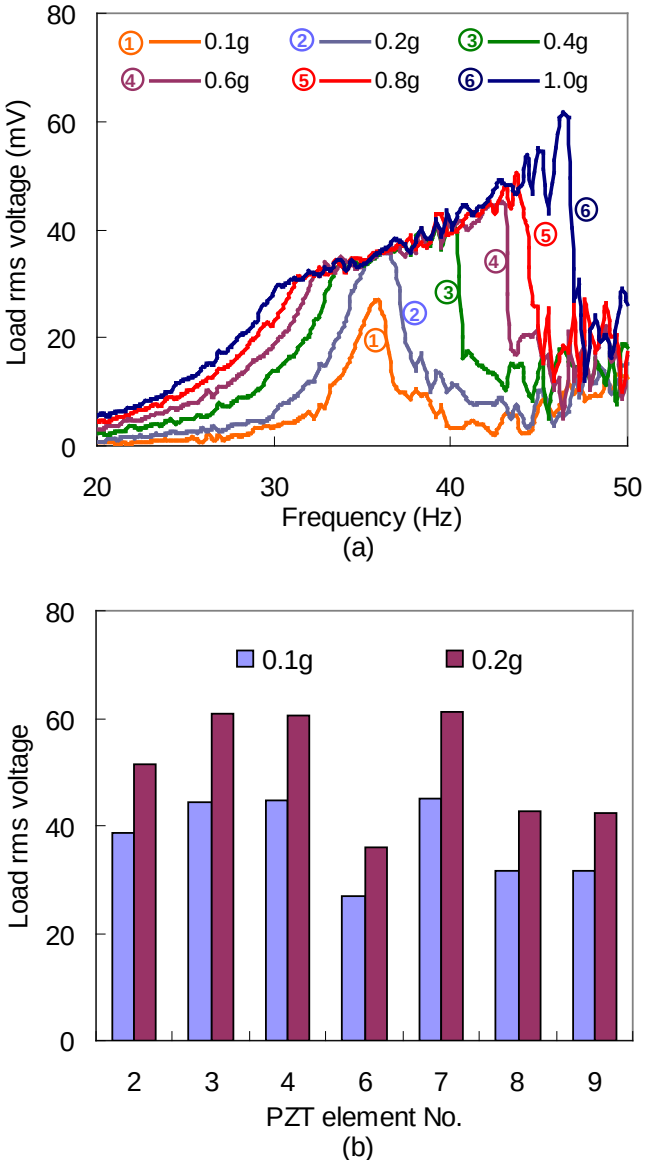

Figure 3.14 (a) Load voltages against frequencies for No. 6 PZT element at different accelerations; (b) Load voltages at resonant frequency of each PZT element at accelerations of 0.1 and 0.2 g.

Figure 3.15 (a) shows the load rms voltages against vibration frequencies for six PZT elements (No. 2, 3, 4, 7, 8, and 9) connected in parallel at different input accelerations. The characteristics show a similar trend with that of Fig. 3.14 (a), but with much higher voltage output. For an input acceleration of 0.1 g, the maximum load rms voltage is 94 mV at a resonant frequency of 36 Hz. As the input acceleration increases to 1.0 g, the load rms voltages increase to 114, 124 and 164 mV at

frequencies of 30.1, 36 and 47.3 Hz, respectively, while the operating bandwidth is extended to 17 Hz (from 30 to 47 Hz). At the same time, the load voltage is steadily increased within this frequency bandwidth. These figures also indicate that, as long as the vibration frequencies are within this bandwidth, the voltage remains constant even as the input acceleration changes.

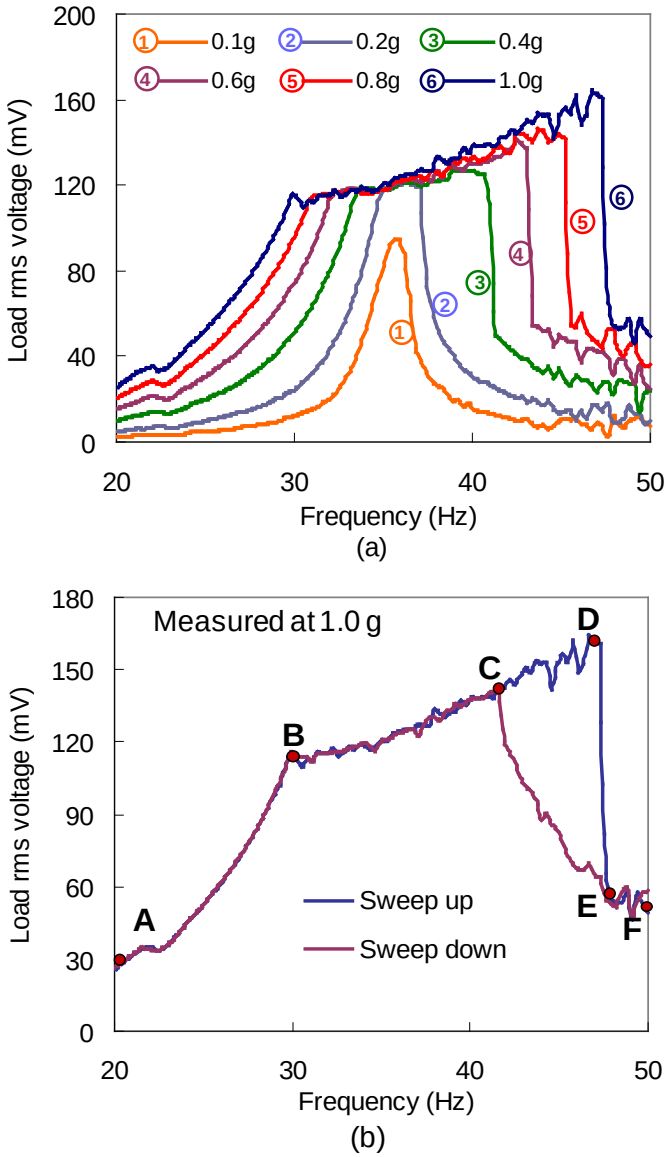

Figure 3.15 (a) Load voltages against frequencies at different accelerations; (b) Load voltages against frequencies at accelerations of 1.0 g for six PZT elements in parallel.

Taken six PZT elements with an input acceleration of 1.0 g for example (as shown in Fig. 3.15 (b)), when the excitation frequency is increased from 20 Hz, the

load voltage increases monotonically from point A until point B (30 Hz), where the proof mass impacts the metal base. From this point, the voltage increases at a smaller rate until it reached point D (47 Hz) where the voltage suddenly decreases to point E. From this point, the system changes to a linear behavior and rattling of the vibration ceases. From point E to point F, the voltage decreases with increasing frequency until 50 Hz. As the excitation frequency sweeps down from 50 Hz, the load rms voltage increases from point F to point C (41.5 Hz), where again the proof mass impacts the metal base and rattling occurs. When the excitation frequency is reduced to point B, the vibrating amplitude is not sufficiently large for the proof mass to engage the metal base and the vibrating frequency is eventually reduced to 20 Hz at point A. In this vibration cycle, the operating bandwidth is widened from 11.5 Hz to 17 Hz, which is an increase of 150% of the original bandwidth.

3.3.1.3 Vibration amplitude measurement

To demonstrate the wideband effect of configuration I and to study the relationship between the proof mass displacement and output voltage, an optical experimental setup shown in Fig. 3.13 is used. In the experiment, six PZT elements (No. 2, 3, 4, 7, 8, and 9) are connected in parallel to a function generator, which act as PZT actuators. The PZT element of No. 6 is connected with the DSA as the energy harvesting element. The excitation frequency is set from 25 to 45 Hz at an increment of 1 Hz. The excitation voltage is applied from 1 to 10 V at an interval of 0.5 V.

Figure 3.16 shows the load voltages of No. 6 PZT element against frequencies at different excitation voltages and input accelerations. This suggests that the voltage outputs and vibration behaviors of PEH-L excited by six PZT elements at excitation voltages of 2.5, 5 and 9 V are equivalent to those excited at accelerations of 0.1, 0.2

and 0.4 g, respectively. Under these three excitation voltages, the sweeping distances of reflected laser light on the plate surface are measured. By using Eqs. (3.24) and (3.25), the mass tip displacements are calculated and plotted in Fig. 3.17.

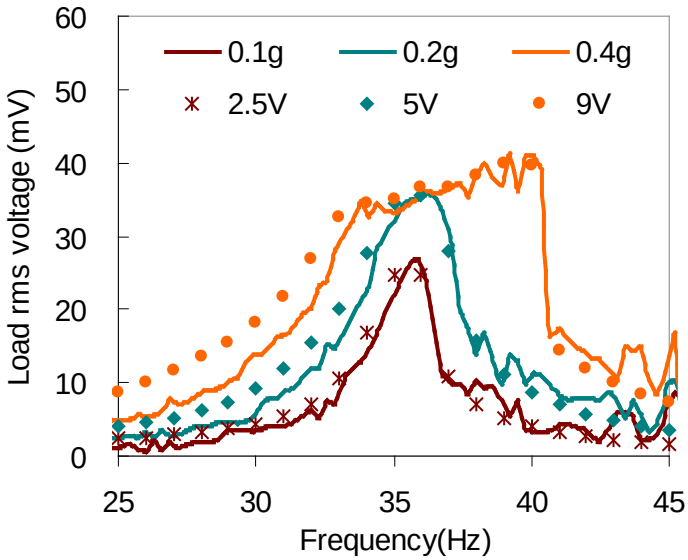

Figure 3.16 Calibration of the load rms voltages of No. 6 PZT element against frequencies at various AC excitation voltages and input accelerations.

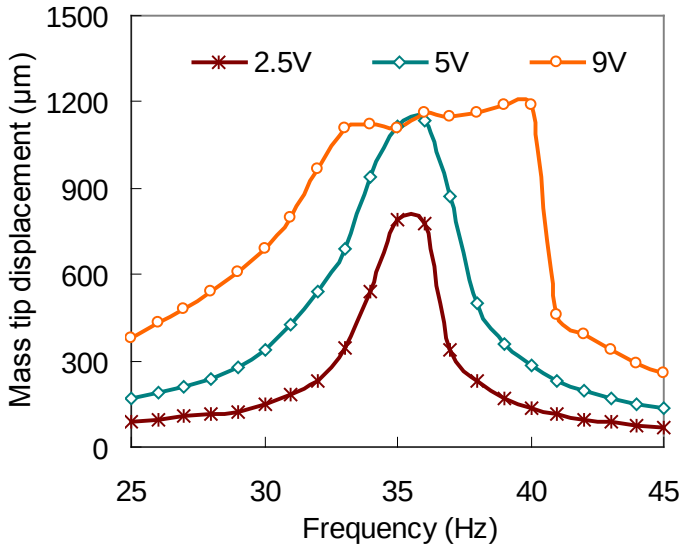

Figure 3.17 Mass tip displacements against frequencies for different excitation voltages.

It is seen that at an excitation voltage of 5 V which is equivalent to input acceleration of 0.2 g, the maximum mass tip displacement is about 1100 μm, which is

the distance between the mass tip and metal base. At an excitation voltage of 9 V, the frequency increases steadily from 25 Hz to 33 Hz, the mass tip displacement increases from 381 μm to about 1100 μm, where it impacts the metal base. The displacement at this stage remains at a platean of around 1100 μm until it reaches to 40 Hz, where the mass tip displacement suddenly decreases to 458 μm. From this point onward, the mass tip displacement decreases gradually to 260 μm at 45 Hz without any rattling occurs.

From the mass tip displacement, the output voltages of one PZT element can be calculated by Eq. (3.7). Using the material properties and structural parameters as shwon in Table 3.1, the computed values are compared with the experimental values of No. 9 PZT element. As shown in Fig. 3.18, both set of results match well. The solid lines represent the experimental results at accelerations of 0.1, 0.2 and 0.4 g and the dotted lines are the theoretical values at excitation voltages of 2.5, 5 and 9 V (which correspond to acceleration of 0.1, 0.2 and 0.4 g).

Table 3.1 Material properties and structural parameters of the piezoelectric cantilever

	Parameter	**Value**
Structural parameters	Length of PZT beam	3 mm
	Width of PZT beam	5 mm
	Thickness of PZT beam	5 μm
	Length of proof mass	5 mm
	Width of proof mass	5 mm
	Thickness of proof mass	0.4 mm
	Length of PZT element	3 mm
	Width of PZT element	0.24 mm
	Thickness of PZT element	3 μm
Material properties	Young's modulus of PZT	72 GPa
	Relative dielectric constant of PZT	1000
	Piezoelectric constant of PZT	-50 pm/V
	Young's modulus of Si	190 GPa

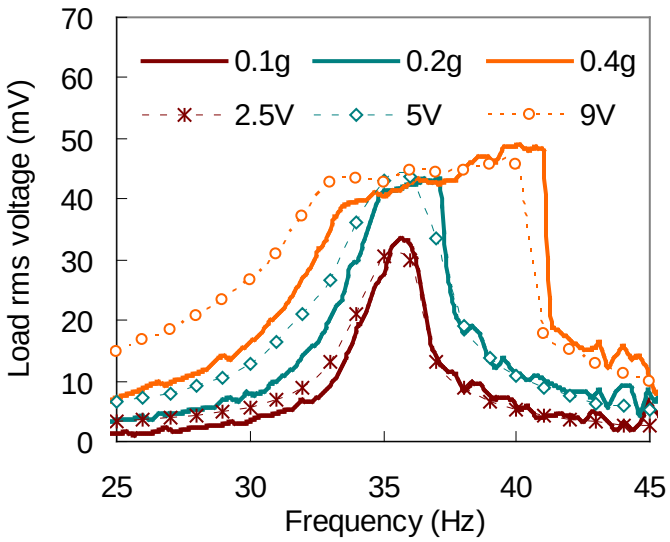

Figure 3.18 Experimental and theoretical results of the load rms voltages against frequencies for No. 9 PZT element.

3.3.2 Configuration II– Two-side stoppers

3.3.2.1 Experimental setup

The experimental setup for configuration II is by and large similar to that of configuration I. As shown in Fig. 3.19 (a), the fine-adjustment (FA) mechanism is utilized to assemble PEH-L and PEH-H together. It consists of a top and bottom L-shaped Al plates mounted on a microstage. The bottom L-shaped plate is fixed while the top L-shaped plate is movable and can be finely adjusted in the x- and z-directions. In addition to PEH-L which is mounted at the bottom L-shaped plate, PEH-H is mounted at the top L-shaped plate. Both the vertical d_1 and horizontal l distances between PEH-L and PEH-H can be adjusted accurately.

The entire FA mechanism is mounted on a vibration shaker as shown in Fig. 3.19 (b). The vibration frequency and amplitude of the shaker are controlled by a DSA through an amplifier. The output voltages of PEH-L with two PZT elements connected in parallel (capacitance of 4.3 nF) and PEH-H with three PZT elements

connected in series (capacitance of 0.72 nF) are recorded separately by the DSA and an oscilloscope (internal impedance 1 MΩ). The measured output voltages of the PEH-L and PEH-H are considered as the load voltages instead of the open circuit voltages.

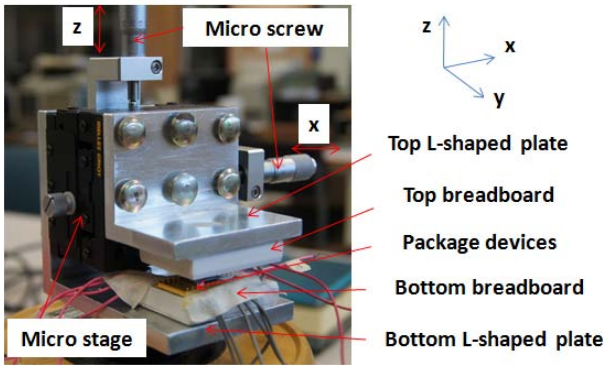

(a)

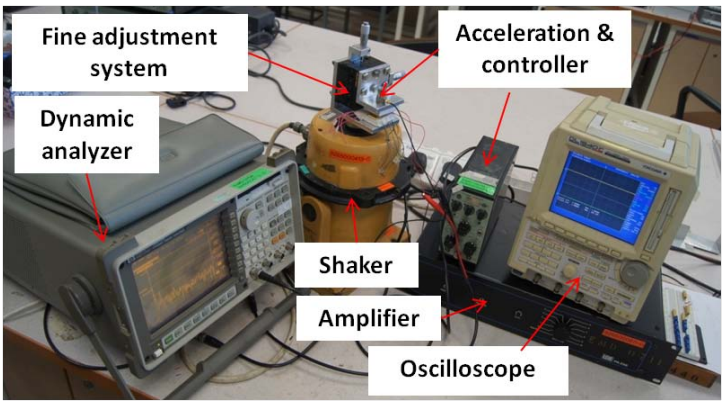

(b)

Figure 3.19 (a) FA mechanism for energy harvesting characterization; (b) Vibration testing setup for configuration II.

3.3.2.2 Energy harvesting characteristics

In configuration II, PEH-H is employed as a top stopper and mounted at distances of 0.75 and 0.5 mm from the proof mass of PEH-L with a horizontal overlapping distance of 0.1 mm. Figure 3.20 shows the output rms voltages of PEH-H against frequencies at accelerations of 0.2, 0.4 and 0.6 g, respectively. As seen in Fig. 3.20 (a), for a top-stopper distance d_1 of 0.75 mm at an acceleration of 0.2 g, as the excitation

frequency sweeps up, the output voltage increases monotonically until the proof mass impacts PEH-H when the amplitude of the proof mass reaches 0.75 mm. Thereafter, the vibration transforms into stage II, and the output rms voltage increases steadily from 60 mV at 34 Hz to 83 mV at 40 Hz. At an acceleration of 0.4 g, when the amplitude of PEH-L reaches 0.75 mm, the proof mass again engages PEH-H (stage II). Thereafter, the amplitude continues to increase until it reaches 1.1 mm at 40 Hz. In this stage, the proof mass engages the metal base which acts as the bottom stopper as well (stage III). In stage II, the output rms voltage increases from 60 to 83 mV as the frequency sweeps from 32 to 40 Hz. In stage III, the output rms voltage increases slightly from 83 to 92 mV as the frequency sweeps from 40 to 46 Hz. Since the stiffness of the bottom stopper is much higher than that of the top stopper, the voltage increment in stage III is significantly lower than that in stage II. At an acceleration of 0.6 g, the operating bandwidth in stages II is broadened from 31 to 40 Hz, while in stage III it is 40 to 49 Hz. The corresponding output rms voltages are respectively 60 to 83 mV and 83 to 97 mV.

When the top-stopper distance d_1 is reduced to 0.5 mm as shown in Fig. 3.20 (b), the maximum voltage in stage II is not significantly reduced except at the initial phase of stage II. However, the rate of voltage increment in stage II becomes steeper and the operating frequency range is widened significantly. At an excitation frequency of about 44 Hz, PEH-L engages the metal base (stage III) and the output voltage remains relatively flat. As a result, decreasing the top-stopper distance would increase the operating frequency range in stage II and shift the on-set vibration of stage III to a higher frequency range.

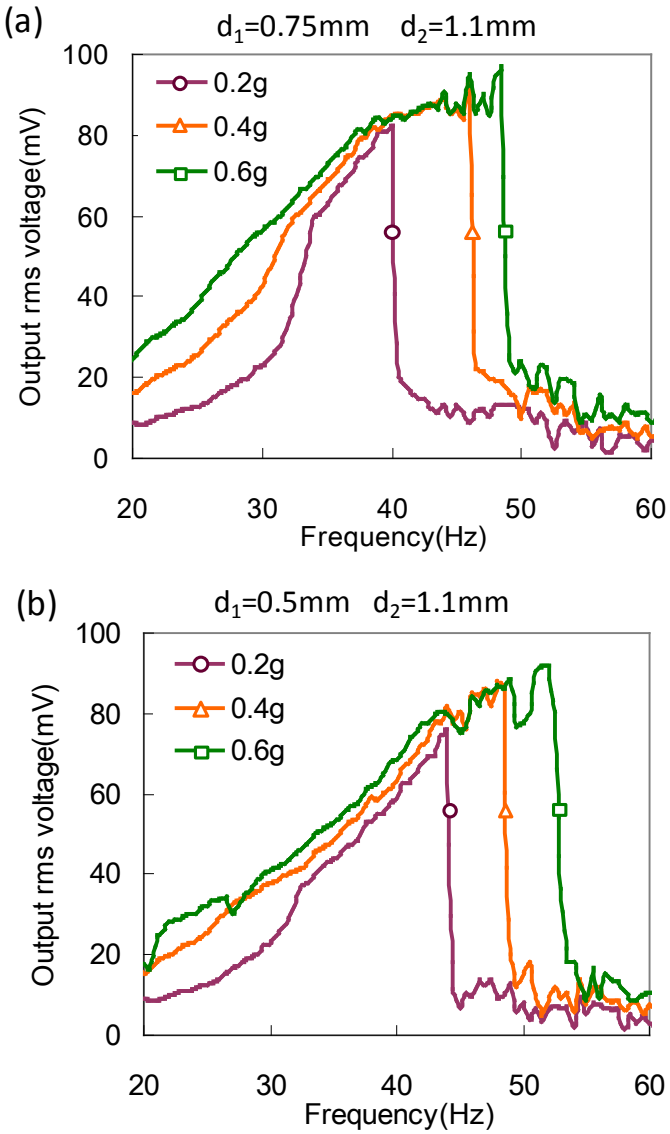

Figure 3.20 Voltage outputs against frequencies for configuration II at different base accelerations and stopper distances.

3.3.3 Comparison of configurations I and II

Appendix B shows the expemental results of the output voltage and power of six connected PZT elements. It elucidates that when the load resistance matches with the internal impedance, the PZT elements either in series or in parallel connections produce the same level of power. However, PZT elements in parallel connection is preferred because a lower matched load resistance is required. Hence, as shown in Fig. 3.21, the optimal power output against frequency for configurations I and II with ten

PZT elements connected in parallel at base acceleration of 0.6 g is obtained by using Eq. (3.21). As can be seen, for configuration I, the output power is relatively higher from 72 to 114 nW within a narrower bandwidth ranging from 32 to 42 Hz. While for configuration II (d_1 = 0.75 mm and d_2 = 1.1 mm), the output power varies from 34 to 100 nW within a larger wideband range of 30 to 48 Hz.

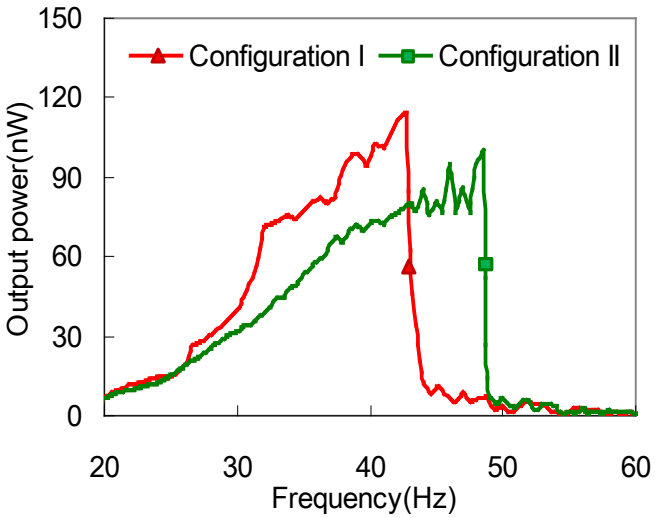

Figure 3.21 Optimal power outputs against frequency for configurations I and II.

Table 3.2 Comparison of operating frequency bandwidth

Ref.	Approach	Device	Acc. (g)	Bandwidth (Hz)	Center freq. (Hz)	NFB
[96]	Cantilever array	--	--	87 -115	100	0.28
[99]	Cantilever array	MEMS	50	4200 - 5000	4600	0.17
[102]	Mechanical stopper	Prototype	0.1	94 - 99	94.7	0.05
[117]	Nonlinear spring	MEMS	0.158	520 - 590	588	0.12
This work	Configuration I	MEMS	0.6	32 - 42	36	0.28
	Configuration II	MEMS	0.6	30 - 48	36	0.5

The operating bandwidth of the PEH system (configurations I and II) is compared with published results as shown in Table 3.2. In terms of normalized

frequency bandwidth (NFB), which is obtained by dividing the operating frequency bandwidth with the center resonant frequency, the proposed wideband PEH system realizes a much higher NFB than those reported.

3.4 Summary

This chapter presents the design, microfabrication, modeling and characterization of a PEH system with a wide operating bandwidth introduced by the use of mechanical stoppers. The wideband frequency responses of the PEH system with one-side stopper (configuration I) and two-side stoppers (configuration II) are analytically and experimentally investigated. The key parameters for the frequency response have been studied based on a mathematical model. It is found that a larger stopper distance will result in a larger operating bandwidth but at a cost of reduced output power. The experimental results show a good agreement with the modeling results. For configuration I, the output power ranges from 72 to 114 nW within a bandwidth ranging from 32 to 42 Hz at an acceleration of 0.6 g. For configuration II, the operating bandwidth is broadened to 18 Hz (30–48 Hz) and the corresponding optimal power ranges from 34 to 100 nW at an acceleration of 0.6 g with the top- and bottom-stopper distances of 0.75 and 1.1 mm, respectively. The operating bandwidth of the PEH system (configurations I and II) in terms of NFB is much higher than those reported. It is noteworthy that the developed MEMS PEH system should provide both the frequency wideband and FUC behaviors at the same time. Hence, in the following chapter, the PEH system with FUC behavior is studied and discussed in detail.

Chapter 4

A FUC Vibration-Based MEMS Energy Harvester

To date most vibration-based energy harvesters, particularly MEMS-based harvesters, operate at frequencies of more than 100 Hz. Increasing compliant spring and bulk movable mass are required to achieve lower resonant frequency for low-frequency vibration scenarios. It is a great challenge to achieve small size and low resonant frequency simultaneously. In addition, low operating frequency would also result in reduced power output. FUC approach has been touted as a breakthrough to boost output power at low vibration frequencies. This chapter describes the work done on the development of FUC energy harvesting systems. This will not only realize a low and wideband frequency response but also convert the low-frequency excitation to a higher frequency range. As a result, significant additional power would be generated.

4.1 Design and Fabrication

4.1.1 Working principle

Figures 4.1 (a) and (b) show the architecture and mechanical model of a vibration-based FUC energy harvester system assembled with FUC oscillators 1 and 2 (termed

as FUC-1 and FUC-2). The system contains an excitation oscillator with spring stiffness k_0, damping factor c_0, and proof mass m_0. FUC-1 with spring stiffness k_1, damping factor c_1 and proof mass m_1 is placed at a distance of x_1 above the proof mass m_0. Likewise, FUC-2 with stiffness k_2, damping factor c_2 and proof mass m_2 is placed at a distance of x_2 below the proof mass m_0. The resonant frequencies of the FUC oscillators, i.e., ω_1 and ω_2, are higher than that of the excitation oscillator ω_0.

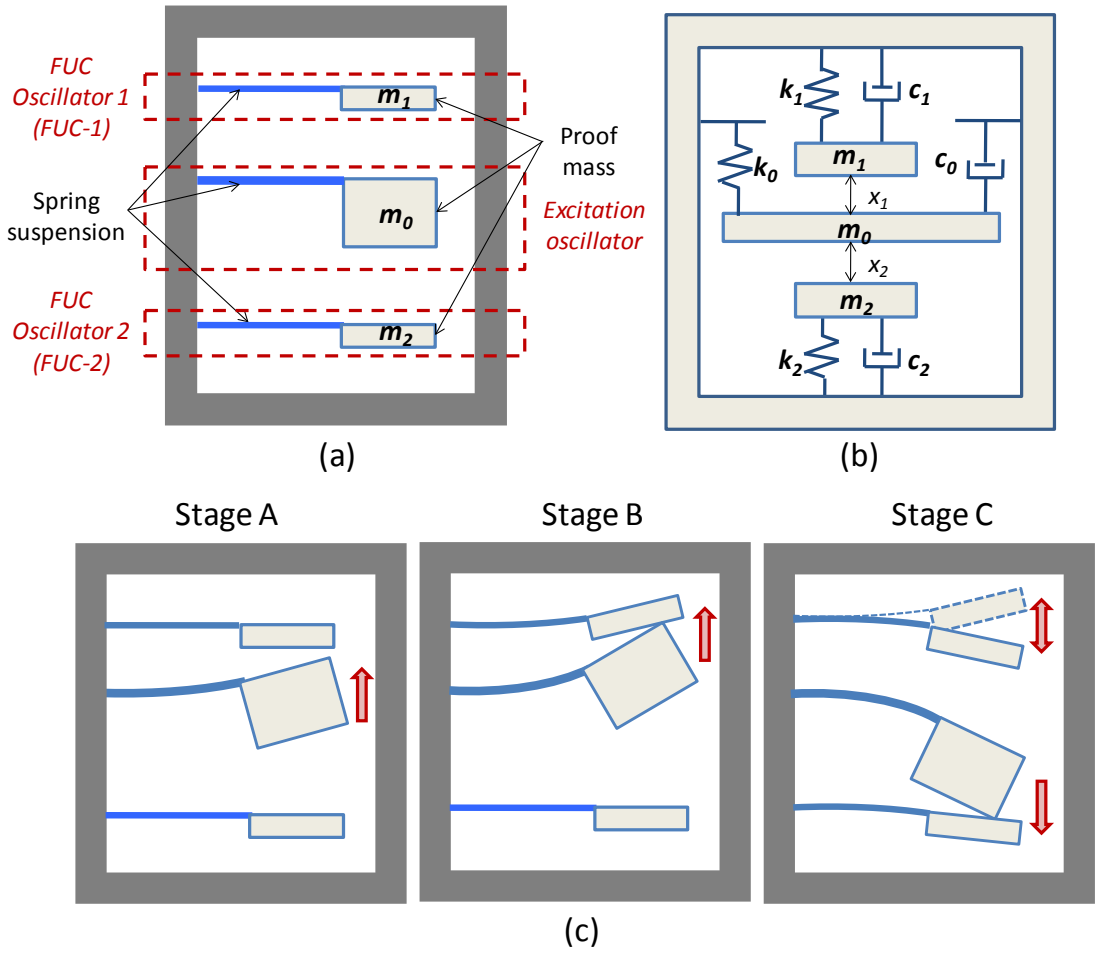

Figure 4.1 (a) Architecture, (b) mechanical model and (c) operation illustration of a vibration-based energy harvester system with FUC oscillators (FUC-1 and FUC-2).

The operation sequence of the system is shown in Fig. 4.1 (c). The excitation oscillator operates in such a way that the proof mass moves upward and downward between the two FUC oscillators and impacts with them periodically. In stage A, the

proof mass moves toward FUC-1. In stage B, the proof mass engages FUC-1 and they move together until the position where FUC-1 is released from the proof mass. In stage C, the proof mass continues its downward movement to FUC-2, during when FUC-1 self-oscillates at a high frequency, converting the mechanical energy in the spring to electrical energy. This process is then repeated in the opposite direction. When the excitation oscillator engages the FUC oscillator, there would be a sudden increase in the effective stiffness. The increase in stiffness would broaden the operating frequency range as described in Chapter 3. Thus the FUC behavior and bandwidth broadening are achieved simultaneously. In the system, the main design consideration is the minimum acceleration and gap distances at which the FUC oscillators will begin operation. In addition, the spring stiffness and weight of the proof mass are also important factors for achieving optimized performance.

4.1.2 Device configuration

4.1.2.1 PEH-I system

In Chapter 3, the frequency wideband behavior of the PEH system has been described. The system is termed PEH-I to differentiate it from a second version PEH-II which is described in the following section. In PEH-I system, the top stopper (PEH-H) also acts as a FUC oscillator and is assembled with a pre-determined gap distance of 0.75 mm from the proof mass. In the case that the vibration amplitude of PEH-L is larger than the gap distance of 0.75 mm, it is able to respond to ambient vibrations over a wider frequency bandwidth, while PEH-H, which acts as a FUC oscillator, would be triggered by the proof mass of PEH-L into a high-frequency oscillation.

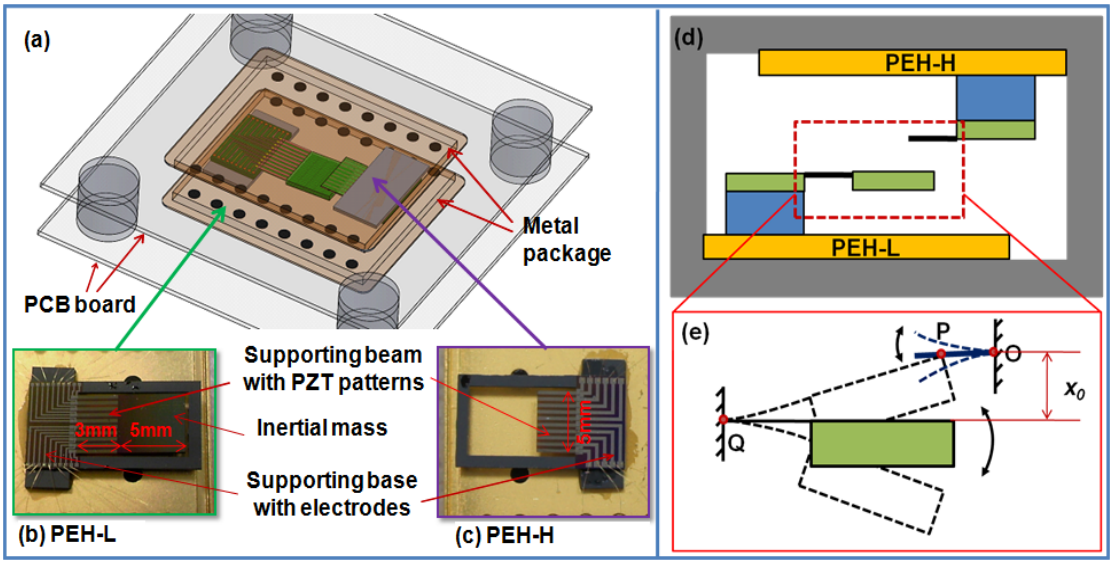

Figure 4.2 (a) Schematic drawing of PEH-I system; (b) microfabricated PEH-L and (c) PEH-H devices; (d) arrangement and (e) vibration behavior of PEH-I system.

4.1.2.2 PEH-II system

In Fig. 4.3 (a), a second FUC system (PEH-II) which comprises of a low-resonant-frequency (LRF) energy harvesting cantilever and a high-resonant-frequency (HRF) energy harvesting cantilever of the same chip size (5.2 mm × 4.2 mm × 0.4 mm). A cross-sectional view of the PEH-II system is shown in Fig. 4.3 (b). The LRF cantilever as shown in Fig. 4.3 (c) consists of a meandered Si beam coated with PZT thin film layer and a Si proof mass (1.65 mm × 2 mm× 0.4 mm) is attached at its end. The effective length, width and thickness of the meandered Si beam are 1.65 mm, 0.2 mm and 5 μm, respectively. The LRF cantilever is not only smaller in size but also has an extremely low resonant frequency of 20 Hz. Such low resonant frequency is rarely reported as MEMS energy harvesters. The HRF cantilever as shown in Fig. 4.3 (d) consists of a straight Si beam (1.65 mm × 2 mm ×5 μm) deposited with PZT thin film layer (2 μm thick) and a proof mass of the same size as that of the LRF cantilever.

The HRF cantilever has a relatively higher resonant frequency of 127 Hz. The detailed material and structural parameters are summarized in Table 4.1.

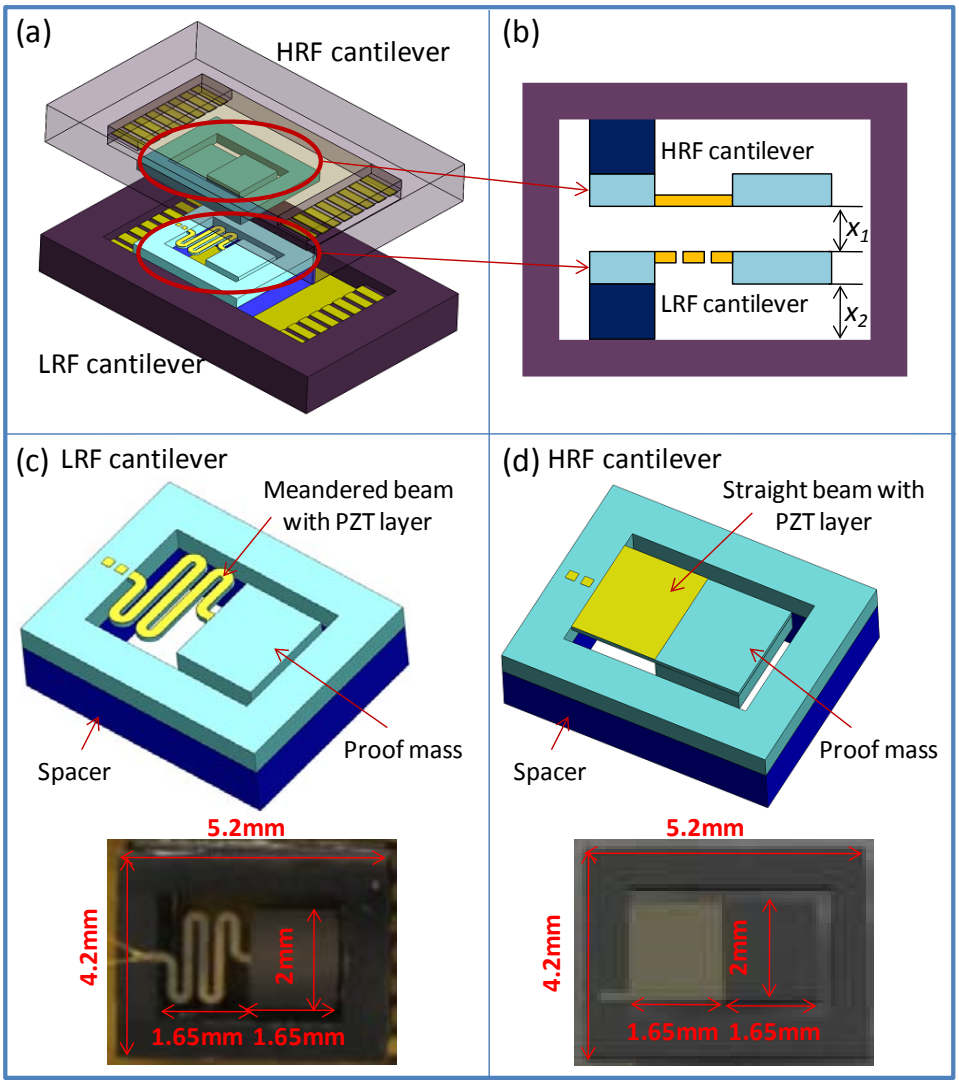

Figure 4.3 (a) Schematic illustration and (b) its cross section view of the PEH-II system; (c) 3D drawings and photographs of the meandered LRF and (d) straight HRF cantilevers.

The LRF and HRF cantilevers are separately assembled onto their DIPs supported by spacer chips in between. The distance x_1 between the HRF and LRF cantilevers is assigned as 1.5 mm, while the distance x_2 between the LRF cantilever and its DIP is 3 mm. Since the PZT thin film layer deposited on the meandered LRF cantilever is limited and the operating frequency is low, the power generated by the

LRF cantilever would be very small. However, due to the low stiffness of the beam, its vibration amplitude could be relatively large. Hence, the LRF cantilever is able to engage the HRF cantilever and subsequently convert the low-frequency excitation into a high-frequency oscillation of the HRF cantilever. As a result, the total output power of the FUC PEH-II system would be increased significantly.

Table 4.1 Material and structural parameters of the LRF and HRF cantilevers

Parameter	**LRF cantilever**	**HRF cantilever**
Young's modulus of PZT, E	72 GPa	
Vacuum dielectric coefficient, ε_0	8.85×10^{-12} Fm^{-1}	
Relative dielectric coefficient of PZT, $\varepsilon_{33}/\varepsilon_0$	1000	
Piezoelectric constant of PZT, d_{31}	-50 pm/V	
Capacitance of PZT thin film, C_e	5.3 nF	13 nF
Thickness of PZT thin film, t_e	2 μm	2 μm
Length of PZT beam, l_b	9.65 mm	1.65 mm
Width of PZT beam, w_b	0.2 mm	2 mm
Thickness of PZT beam, t_b	5 μm	5 μm
Length of proof mass, l_m	1.65 mm	1.65 mm
Width of proof mass, w_m	2 mm	2 mm
Thickness of proof mass, t_m	0.4 mm	0.4 mm
Weight of proof mass, m	3.1×10^{-6} kg	3.1×10^{-6} kg
Resonant frequency of cantilever, f	20 Hz	127 Hz
Angular frequency of cantilever, ω	125.6	797.6
Damping ratio, ξ	0.01	0.01

4.1.3 Fabrication process

The meandered LRF and straight HRF cantilevers are fabricated using micromachining process on a SOI wafer with 5-μm-thick Si device layer, 1-μm-thick BOX layer and 400-μm-thick Si handle layer. The process starts from multilayer

depositions of Pt/Ti/PZT/Ti/Pt/SiO_2 on the frontside of the SOI wafer as shown in Fig. 4.4 (a). After thermal oxidation of the SOI wafer at 1100 °C, Pt (0.2 μm)/Ti (0.05 μm) thin films are deposited by DC magnetron sputtering to form the bottom electrode. A $Pb(Zr_{0.52,}Ti_{0.48})O_3$ film of 2-μm-thick is then deposited by sol-gel deposition. Finally, Pt (0.2 μm)/Ti (0.05 μm) thin films are deposited by DC magnetron sputtering to form the top electrode.

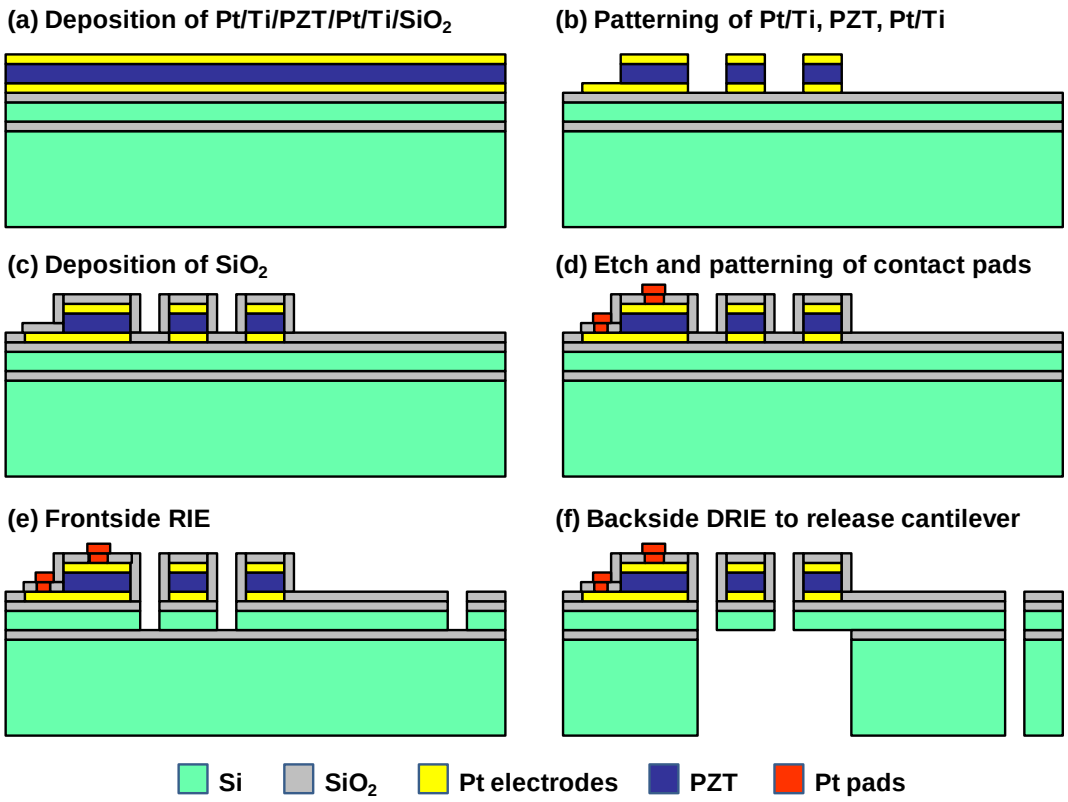

Figure 4.4 Microfabrication process of the LRF and HRF cantilevers.

In Fig. 4.4 (b), the top and bottom electrodes are etched by Ar ions, and the PZT thin film is wet etched by a mixture of HF, HNO_3 and HCl. A 0.8-μm-thick SiO_2 thin film is then deposited by RF-magnetron sputtering as an insulation layer as shown in Fig. 4.4 (c). In Fig. 4.4 (d), contact holes are etched and patterned with Pt to form the bonding pads. As shown in Fig. 4.4 (e), the SiO_2 layer and Si device layer are etched by RIE using feed gases of CHF_3 and SF_6, respectively. Finally, as in Fig. 4.4 (f), the

Si handle layer and BOX layer are etched from the backside using DRIE to release the cantilever structure. The microfabricated devices are assembled onto their DIPs with spacer chips in between and the bonding pads are connected to the metal pins of the DIPs by gold wires.

4.2 Modeling and Simulation

4.2.1 Modeling of FUC energy harvester system

As shown in Fig. 4.5, a mechanical model of a FUC vibration-based energy harvester system is composed of three mass-spring-damper oscillation sub-systems in which each sub-system influences each other. When the whole system is subjected to a time-varying excitation acceleration, the three oscillators will respond nonlinearly due to the periodic impact. A time-domain dynamic analysis is carried out and three cases are considered.

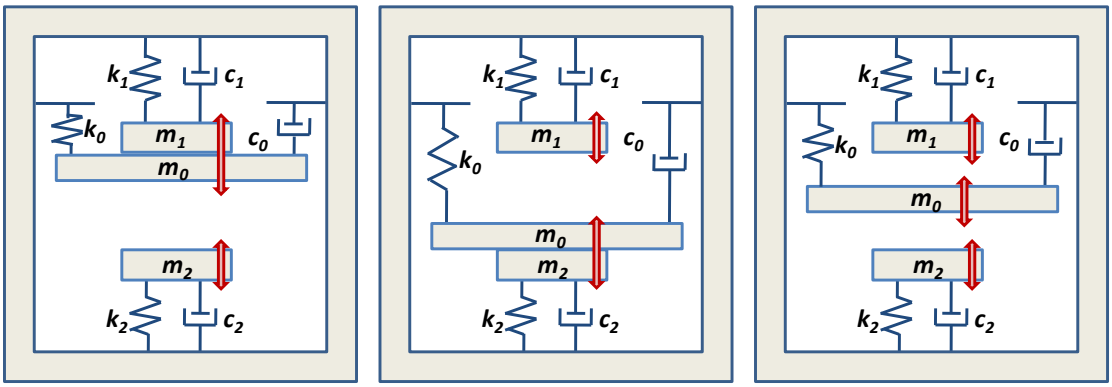

Figure 4.5 Illustration of cases I, II and III when the excitation oscillator is moving in between the two FUC oscillators.

Case I is the situation in which the excitation oscillator and FUC-1 engages each other and moves as a single system as shown in Fig. 4.5 (a), and FUC-2 is oscillating by itself at its own resonant frequency. Similarly, as shown in Fig. 4.5 (b), case II

describes a system when the excitation oscillator engages FUC-2 and FUC-1 is left to self-oscillate on its own. In case III, all the three oscillators are oscillating separately as shown in Fig. 4.5 (c). In this case, the excitation oscillator has just separated from the combined mode with one FUC oscillator, and is approaching to the other FUC oscillator.

The motions of the excitation oscillator, FUC-1 and FUC-2 relative to the casing are denoted by $z(t)$, $s_1(t)$, and $s_2(t)$, respectively. The differential equations of motion in case I are described by two second-order differential equations. After the engagement between FUC-1 and the excitation oscillator, the combined FUC-1 oscillator is driven by an external excitation $\ddot{y}\sin(\omega t)$. While the single FUC-2 experiences a damped self-oscillation after release from the excitation oscillator. Therefore, the motions of the combined FUC-1 and single FUC-2 oscillators in case I are given by

$$(m_0 + m_1)\ddot{s}_1 + (c_0 + c_1)\dot{s}_1 + k_1 s_1 + k_0(s_1 + x_1) = -(m_0 + m_1)\ddot{y}\sin(\omega t) \tag{4.1}$$

$$m_2\ddot{s}_2 + c_2\dot{s}_2 + k_2 s_2 = -m_2\ddot{y}\sin(\omega t) \tag{4.2}$$

Since the motion of the excitation oscillator $z(t)$ is the same as FUC-1 with a top gap distance x_1, it is represented as $z(t) = s_1(t) + x_1$.

Case II accounts for the time when the excitation oscillator is combined with FUC-2. It is symmetric to case I with only sign changes. Therefore, the motions of the combined FUC-2 and single FUC-1 are given by

$$(m_0 + m_2)\ddot{s}_2 + (c_0 + c_2)\dot{s}_2 + k_2 s_2 + k_0(s_2 - x_2) = -(m_0 + m_2)\ddot{y}\sin(\omega t) \tag{4.3}$$

$$m_1\ddot{s}_1 + c_1\dot{s}_1 + k_1 s = -m_1\ddot{y}\sin(\omega t) \tag{4.4}$$

Similarly, the motion of the excitation oscillator is the same as FUC-2 with an bottom gap distance x_2, thus it is given by $z(t) = s_2(t) - x_2$.

When the excitation oscillator is in contact with either FUC-1 or FUC-2, a normal (or contact) force T is exerted on the FUC oscillator. When the oscillators are no longer in contact, T is equal to zero. The normal forces exerted on FUC-1 (T_1) and FUC-2 (T_2) by the excitation oscillator are given by

$$T_1 = m_1\ddot{s}_1 + c_1\dot{s}_1 + k_1 s_1 + m_1\ddot{y}\sin(\omega t) \tag{4.5}$$

$$T_2 = m_2\ddot{s}_2 + c_2\dot{s}_2 + k_2 s_2 + m_2\ddot{y}\sin(\omega t) \tag{4.6}$$

In case III, these three oscillators are free to move independently. Therefore, the differential equation of motions are given by

$$m_0\ddot{z} + c_0\dot{z} + k_0 z = -m_0\ddot{y}\sin(\omega t) \tag{4.7a}$$

$$m_1\ddot{s}_1 + c_1\dot{s}_1 + k_1 s = -m_1\ddot{y}\sin(\omega t) \tag{4.7b}$$

$$m_2\ddot{s}_2 + c_2\dot{s}_2 + k_2 s_2 = -m_2\ddot{y}\sin(\omega t) \tag{4.7c}$$

Case III is valid as long as the excitation oscillator does not make contact with either of the FUC oscillators. If $z(t)$ is larger than $s_1(t) + x_1$ or less than $s_2(t) - x_2$, the system will revert back from case III to case I or II.

During the impact, the initial velocities of the combined FUC-1 and FUC-2 systems in cases I and II using the conservation of linear momentum are given by

$$V_1 = \frac{(C_R + 1)m_1 v_1 + (m_0 - C_R m_1)v_0}{m_0 + m_1} \tag{4.8}$$

$$V_2 = \frac{(C_R + 1)m_2 v_2 + (m_0 - C_R m_2)v_0}{m_0 + m_2} \tag{4.9}$$

where v_0, v_1 and v_2 are the instantaneous velocities of the three single oscillators at the moment of contact; V_1 and V_2 are the ensuing velocities of the combined FUC-1 and FUC-2 in cases I and II; C_R is the coefficient of restitution of two colliding objects is a fractional value representing the ratio of speeds after and before an impact. C_R = 1 represents the situation that pairs of objects with collide elastically, while C_R < 1 is the case that objects collide inelastically. For C_R = 0, the objects effectively "stop" at the collision, not bouncing at all. In this model, it is assumed the impact between the excitation oscillator and FUC oscillators is an elastic collision (C_R = 1). Hence, Eqs. (4.8) and (4.9) are simplified as:

$$V_1 = \frac{2m_1 v_1 + (m_0 - m_1)v_0}{m_0 + m_1} \tag{4.10}$$

$$V_2 = \frac{2m_2 v_2 + (m_0 - m_2)v_0}{m_0 + m_2} \tag{4.11}$$

4.2.2 Simulation of FUC energy harvester system

The dynamic motion of a FUC energy harvester system can be simulated using a software tool (Matlab). In the simulation, the excitation oscillator is assumed as a LRF cantilever, while FUC-1 and FUC-2 are considered as HRF cantilevers. The material properties and dimensions are shown in Tablea 4.1. The proof mass of the excitation oscillator and FUC oscillators is 3.1×10^{-6} kg. The resonant frequency of the excitation oscillator is 20 Hz, while that of FUC-1 and FUC-2 is 127 Hz. Hence, the corresponding frequency characteristics in terms of ω_0, ω_1 *and* ω_2 are 125.6, 797.6 and 797.6, respectively, where $\omega_0 = 2\pi f_0$, $\omega_1 = 2\pi f_1$ and $\omega_2 = 2\pi f_2$. The damping ratios ξ_0, ξ_1 and ξ_2 are assumed to be 0.01, and the damping factors c_0, c_1 and c_2 are obtained from $2\xi_0\omega_0 = c_0 / m_0$, $2\xi_1\omega_1 = c_1 / m_1$ and $2\xi_2\omega_2 = c_2 / m_2$. FUC-1 and FUC-

2 are set at the same gap distance of 4 mm from the excitation oscillator. When the system is subjected to a harmonic excitation, the simulation diagram for the dynamic motion of the FUC energy harvester system is given in Fig. 4.6.

The simulation time is started from *t=0* s and ended at *t=10* s with a tiny time step of 0.001 s. In the initial condition, the simulation parameters of the excitation oscillator, FUC-1 and FUC-2 are provided. As the system responds to the external excitation $y(t)$, the mass displacements $z(t), s_1(t), s_2(t)$,velocities $\dot{z}(t), \dot{s}_1(t), \dot{s}_2(t)$ and accelerations $\ddot{z}(t), \ddot{s}_1(t), \ddot{s}_2(t)$ of the three oscillators are calculated in case III using the differential equations (4.7a), (4.7b) and (4.7c), respectively. At every time step in case III loop, the gap distances between the excitation oscillator and the FUC-1 [$x_1 = z(t) - s_1(t)$], FUC-2 [$x_2 = s_1(t) - z(t)$] are counted. As the gap distance x_1 or x_2 satisfies the condition $x_1 \leq 0$ or $x_2 \leq 0$, it means the excitation oscillator starts to contact with FUC-1 or FUC-2. Subsequently, the dynamic mass motion of the system will jump from case III to case I or case II, which accounts for the situation when the excitation oscillator is combined with FUC-1 or FUC-2. The initial velocities of the combined FUC-1 and FUC-2 systems in cases I and II, namely V_1 and V_2 are given by equations (4.10) and (4.11), where the velocities of the three oscillators before engagement, namely v_0, v_1 and v_2 can be obtained from the last time step calculation in case III. After the system transfer to case I or II, the mass displacements, velocities and accelerations of the three oscillators can be obtained in every time step, by using equations (4.1) and (4.2) for case I and equations (4.3) and (4.4) for case II. Meanwhile, the contact force T between the excitation oscillator and FUC oscillator is calculated according to equations (4.5) and (4.6), respectively, in every running loop. As T is equal to zero, the oscillators are no longer in contact and the system returns

back to case III again. The calculation loop will be continued until the simulation time runs to the time end.

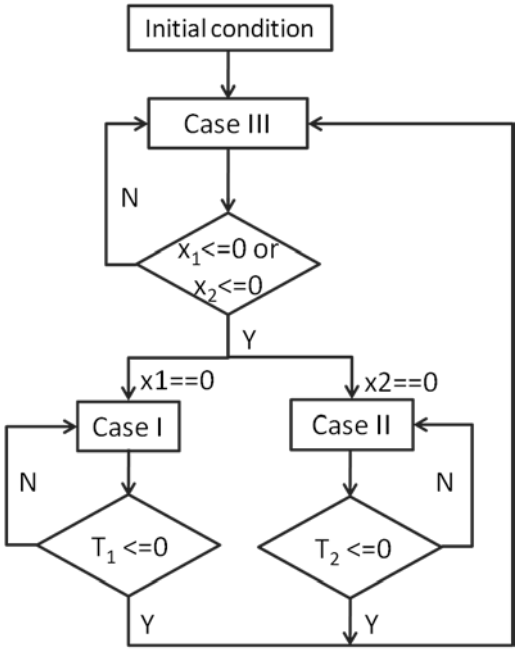

Figure 4.6 Simulation diagram using Matlab for the dynamic motion of the FUC energy harvester system.

Figure 4.7 shows the dynamic motion of FUC-1 (in green solid line), FUC-2 (in blue solid line) and excitation oscillator (in red dash line) as the system is subjected to a harmonic excitation of frequency 20 Hz at an acceleration of 1 g. For clarity, the motion of FUC-1 and FUC-2 is shifted at a distance of 4 mm from that of the excitation oscillator. Considering a particular instant of an oscillation cycle when the excitation oscillator is just in contact with FUC-1 at point A (case I). The excitation oscillator and FUC-1 are engaged and moves upward together. They experience a damped oscillation in its combined mode until point B, where the contact force between FUC-1 and excitation oscillator is reduced to zero. Thereafter, they separate from each other and assume a case III motion, where FUC-1 is left to self-oscillate at high frequency, while the excitation oscillator continues its downward movement

until point C. At point C, the excitation oscillator engages FUC-2 and assumes a case II motion until point D. At point D, FUC-2 is released to self-oscillate at high frequency, while the excitation oscillator moves upward until point E, where the excitation oscillator engages the self-oscillating FUC-1 again. The vibration cycle will persist as long as the amplitude of the excitation oscillator is larger than the prescribed gap distance of 4 mm.

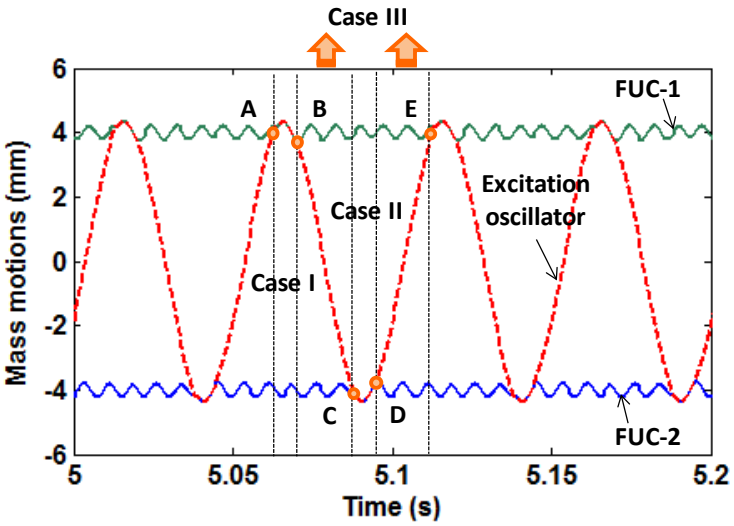

Figure 4.7 Simulation results of the dynamic motion of FUC-1, FUC-2 and excitation oscillator at an excitation frequency of 20 Hz and acceleration of 1 g.

Using Eq. (3.8), the output voltages of FUC-1 and the excitation oscillator are plotted as shown in Fig. 4.8 (a). The output voltage characteristics of FUC-2 are similar to that of FUC-1. As can be seen, the peak voltage of FUC-1 (151.9 mV) is higher than that of the excitation oscillator (80.7 mV), although the amplitude of FUC-1 (0.35 mm) is much smaller than that of the excitation oscillator (4.35 mm). From the output voltage shown in Fig. 4.8 (a), the optimized output power of FUC-1 and excitation oscillator are computed using Eq. (3.9) and shown in Fig 4.8 (b). Since the peak power of the excitation oscillator is only about 4.4 nW, it is too low to be identified. In contrast, the peak power of FUC-1 is as high as 0.24 μW, which is 54 times higher than that of the excitation oscillator. Similarly, the peak voltage and

power of FUC-2 are similar to those of FUC-1. It is clear that the output power of the system is significantly improved by employing the FUC oscillators.

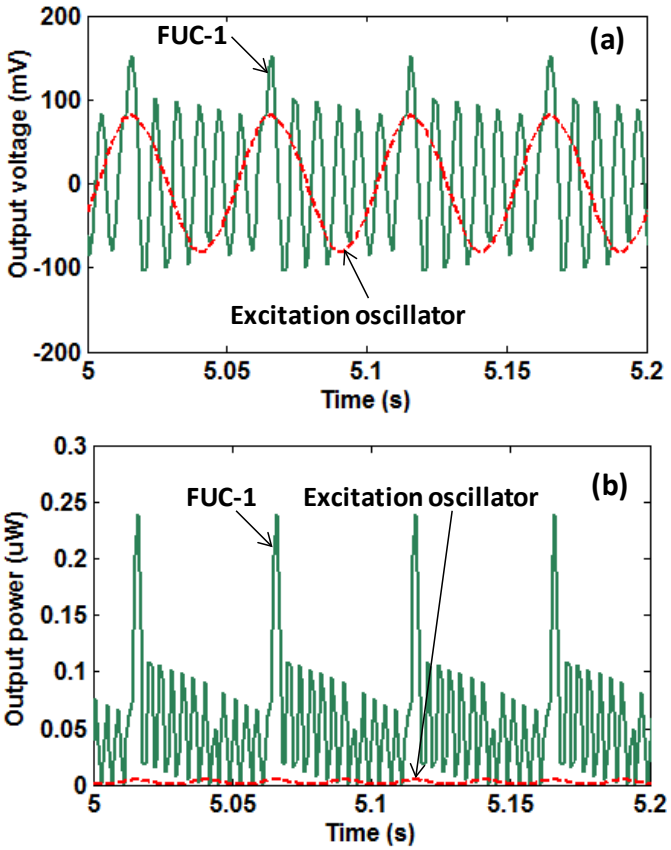

Figure 4.8 Simulated results of (a) output voltages and (b) power for FUC-1 and the excitation oscillator at excitation frequency of 20 Hz and acceleration of 1 g.

4.3 Experimental Work and Discussion

4.3.1 Experimental setup

Figure 4.9 shows the vibration testing setups for the FUC energy harvester (PEH-I and PEH-II) systems. The FA mechanism (in Fig. 3.19 (a)) is again employed for adjusting the gap distance between the excitation and FUC oscillators. The packaged PZT cantilevers are assembled onto their breadboards and mounted on the top and bottom L-shaped plates separately. The FA mechanism together with the assembled device is mounted on a vibration shaker. The vibration frequency and amplitude of the

shaker are controlled by a function generator through an amplifier. An accelerometer is attached to the FA mechanism to measure the base vibration acceleration. The output voltages of the PZT cantilevers are recorded by an oscilloscope with an assumed load resistance of 1 MΩ.

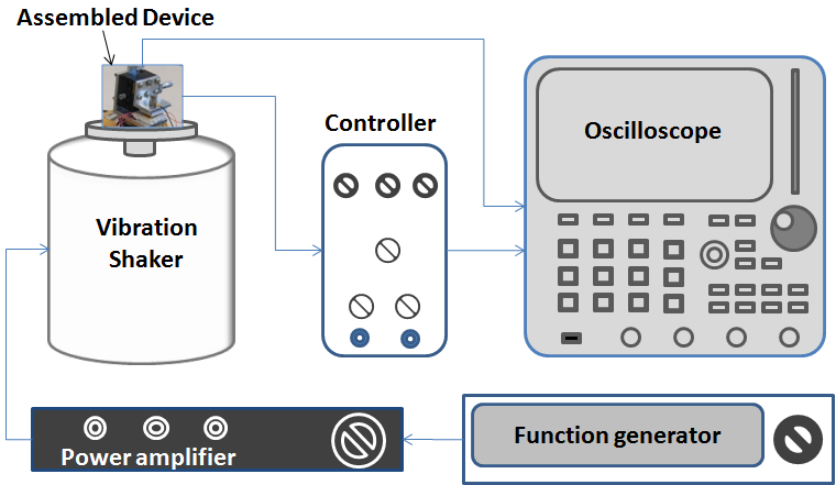

Figure 4.9 Experimental setup for the FUC energy harvester system.

4.3.2 PEH-I system

Figure 4.10 illustrates the FUC behavior of PEH-L and PEH-H in the PEH-I system. Since the top gap distance of 0.75 mm is smaller than the bottom gap distance of 1.1 mm, PEH-L could only engage PEH-H and not the metal package base. Consider a particular instant of an oscillation cycle when the proof mass is at its lowest point at position① and starts to move to position② where it impacts the supporting beam of PEH-H. The proof mass would then move upward together with the supporting beam until it reaches its maximum amplitude at position③. Subsequently, the proof mass together with the supporting beam would move downward until the supporting beam loses contact with the proof mass at position④. Thereafter, the proof mass continues its downward movement to position① during which the supporting beam of PEH-H is

left to self-oscillate at its own resonant frequency. The cycle is then repeated as the proof mass moves towards position② again. The oscillation cycle is repeated as long as the vibration amplitude of the proof mass is larger than the gap distance.

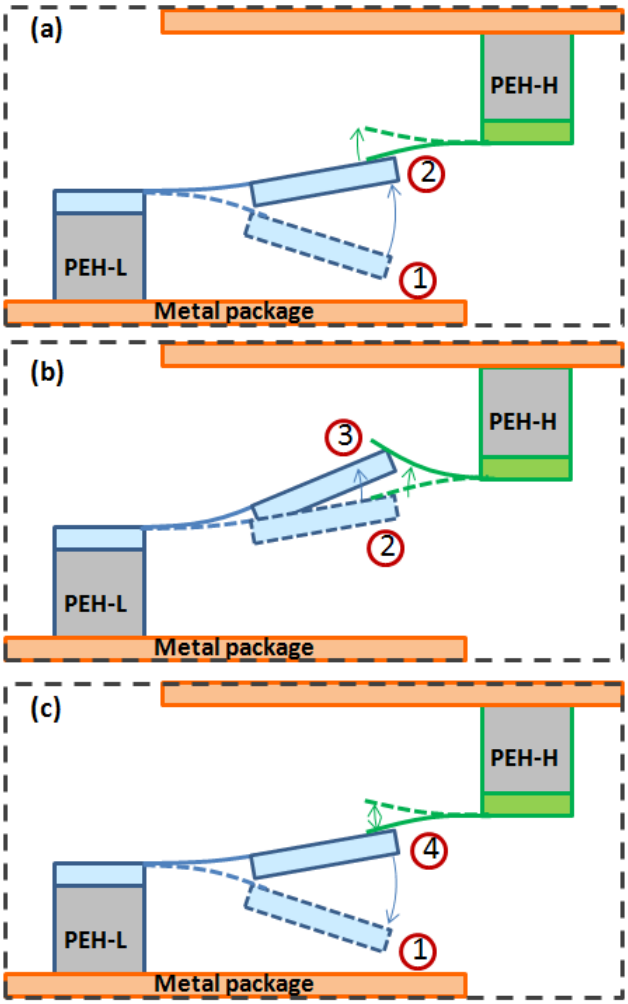

Figure 4.10 FUC behavior of the PEH-I system.

In the PEH-I system, two PZT elements of both PEH-L and PEH-H are connected in series for energy harvesting. From the instantaneous voltage output, it is found that the FUC behavior occurs over a wide operating bandwidth ranging from 30 Hz to 52 Hz at a base acceleration of 0.8 g and a gap distance of 0.75 mm. Figure 4.11 shows the instantaneous output voltage of PEH-L and PEH-H at frequencies of 37 and 51 Hz at 0.8 g, respectively. In Fig. 4.11 (a), the output voltage (peak voltage of 65.5

mV) of PEH-L (in blue) oscillates at 37 Hz; when it engages PEH-H (in red), which subsequently starts to self-oscillate at its natural frequency of 618 Hz, at an peak voltage of 73 mV, which is higher than that of PEH-L. At a higher excitation frequency of 51 Hz (Fig. 4.11 (b)), the peak voltage of PEH-L is 87.2 mV, while the peak voltage of PEH-H is increased to 106.1 mV at its natural frequency of 618 Hz. The output power at excitation frequencies of 37 and 51 Hz (acceleration of 0.8 g) are approximately 0.006 and 0.012 μW, respectively. Thus for ten PZT elements, the peak power would be around 0.03 (37 Hz) and 0.06 μW (51 Hz). As for PEH-H, the peak power at 37 and 51 Hz are around 0.018 and 0.026 μW, respectively. Hence, the peak power for ten PZT elements would be 0.09 (37 Hz) and 0.13 μW (51 Hz). The above results show that by incorporating the FUC oscillator, the total peak-power of the system at input acceleration of 0.8 g is increased to 0.12 and 0.19 μW at 37 and 51 Hz, respectively.

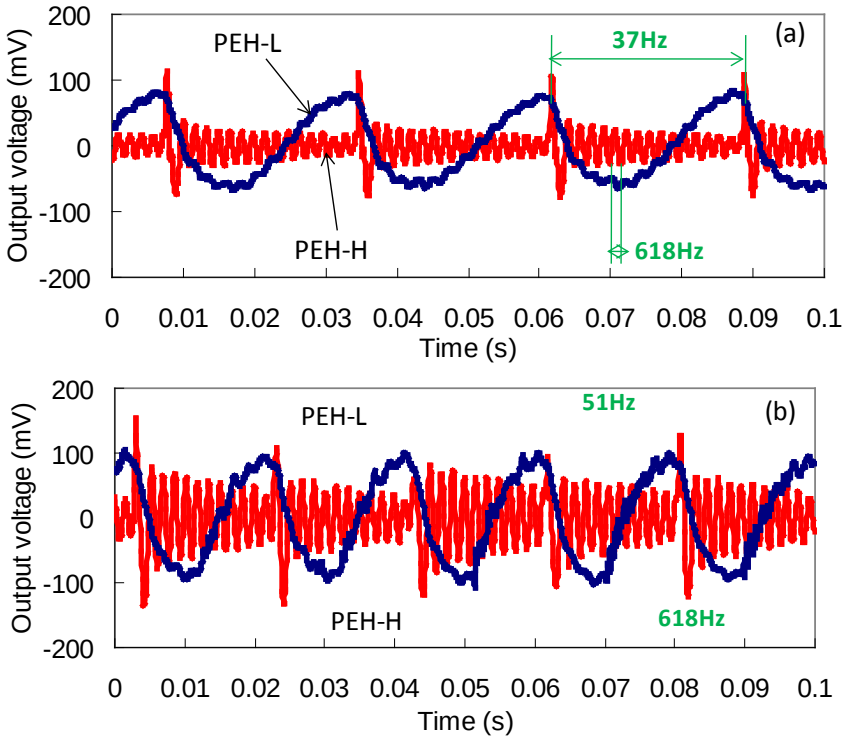

Figure 4.11 Instantaneous output voltages of PEH-L and PEH-H at frequencies of (a) 37 Hz and (b) 51 Hz at 0.8 g.

4.3.3 PEH- II system

As illustrated in Fig. 4.10, the FUC behavior of the PEH-II system is similar to that of PEH-I system. Since the top gap distance of 1.5 mm is smaller than the bottom gap distance of 3 mm, the LRF cantilever could only engage the HRF cantilever and not the metal package base. From the voltage output of PEH-II system, it is seen that FUC occurs during a wide operating frequency range from 13 to 26 Hz for a base acceleration of 0.8 g.

Figure 4.12 shows the instantaneous output voltages of the LRF and HRF cantilevers at vibration frequencies of 20 and 25 Hz, respectively. In Fig. 4.12 (a), the LRF cantilever (in green) oscillating at 20 Hz impacts the HRF cantilever at every vibration cycle and results in the HRF cantilever self-oscillating at 127 Hz (in purple). The peak voltage of the HRF cantilever of 153 mV is about 5 times higher than that of the LRF cantilever. Likewise, in Fig. 4.12 (b), the peak voltage of the HRF cantilever oscillating at 25 Hz is 209 mV, while that of the LRF cantilever which oscillates at 127 Hz has an peak voltage of 49 mV. The output voltage is increased about 4 times at a frequency of 25 Hz.

It is seen from Fig. 4.13 that at frequencies of 20 and 25 Hz (assuming the load resistance matches internal impedances), optimal power spectra can be calculated from the corresponding output voltages. For the LRF cantilever, the peak power obtained at 20 and 25 Hz are 0.003 and 0.01 μW, respectively. While those of the HRF cantilever are 0.34 (at 20 Hz) and 0.87 μW (at 25 Hz). As can be seen, the peak power of the HRF cantilever is up to 100 times higher than that of the LRF cantilever. With regards to the output rms power, the HRF cantilever is able to deliver up to 200 times higher than the LRF cantilever.

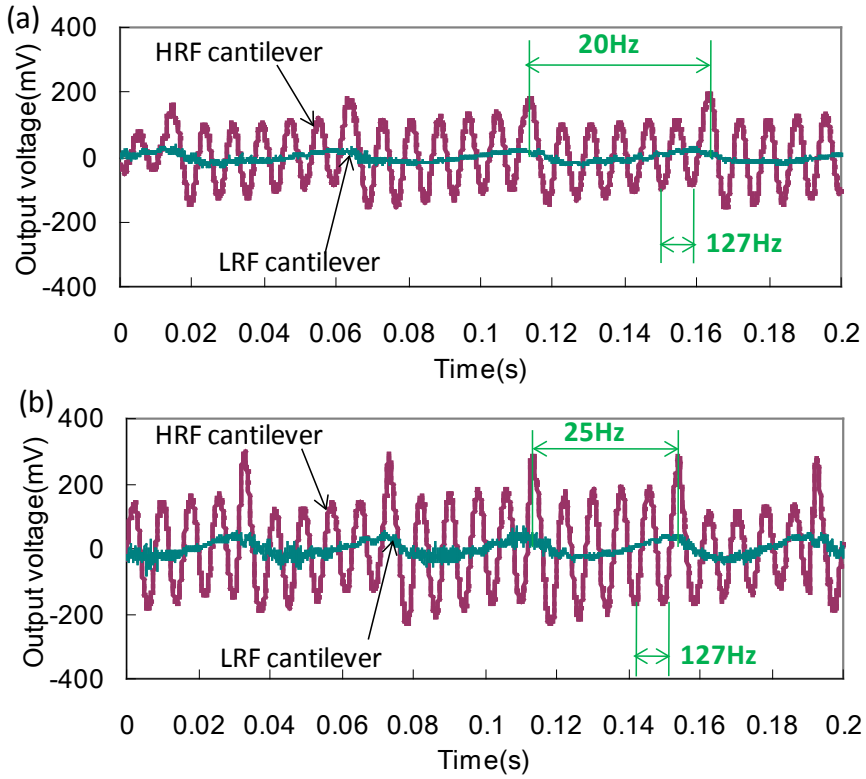

Figure 4.12 Instantaneous output voltages of LRF and HRF cantilevers at frequencies of (a) 20 Hz and (b) 25 Hz at 0.8 g.

The peak voltage and peak power of the LRF and HRF cantilevers at frequencies ranging from 10 Hz to 30 Hz and acceleration of 0.8 g are shown in Fig. 4.14. As can be seen, significant improvement in the voltage and power output is observed after the LRF cantilever engages the HRF cantilever at frequencies ranging from 13 to 26 Hz. When the excitation frequency is below 13 Hz or above 26 Hz, the voltage and power outputs of both cantilevers are insignificant. This is due to the low vibration amplitude of the LRF cantilever which is insufficient to trigger the vibration of the HRF cantilever. Hence, one can see that the PEH-II system is able to not only operate in a low and wideband frequency range but also achieves a higher power output. The power density of the system (output power divided by the volume of the cantilevers) in this case varies from 25.8 to 164.6 μW/cm3 in the frequency range of 13 to 26 Hz.

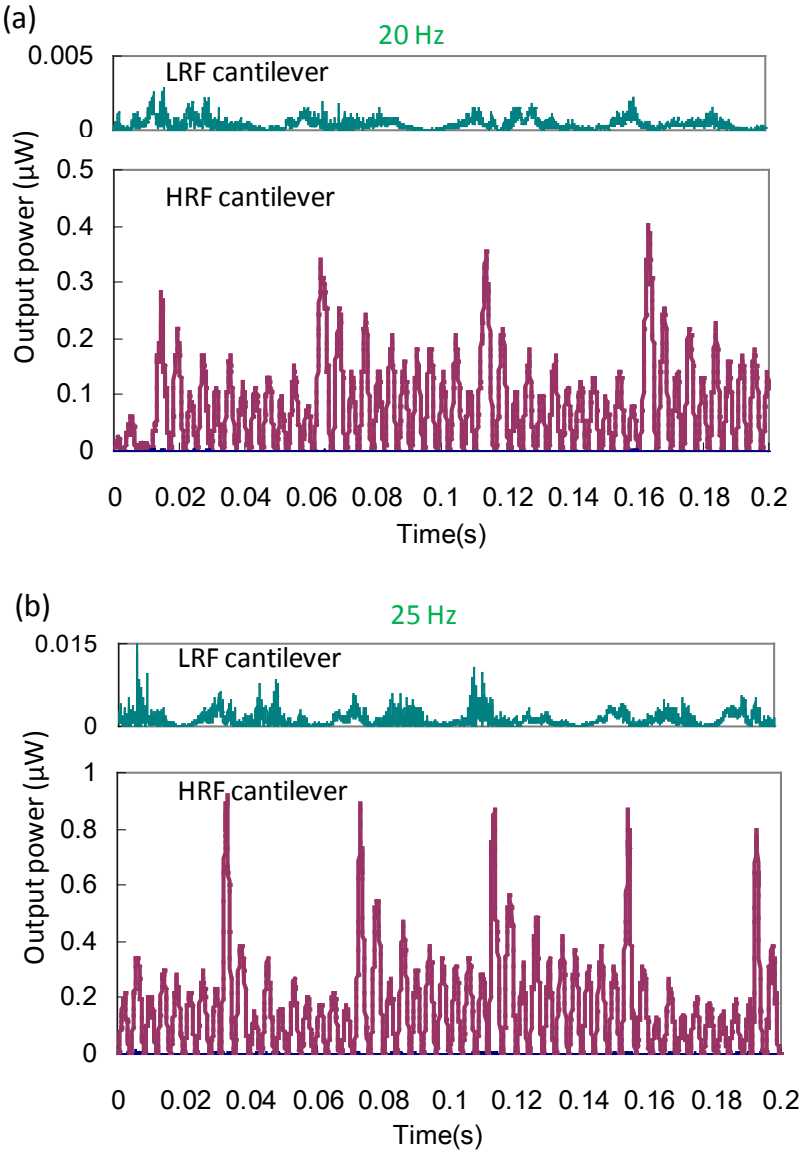

Figure 4.13 Output power spectra of LRF and HRF cantilevers at frequencies of (a) 20 Hz and (b) 25 Hz at 0.8 g.

There are mainly three reasons for the significant improvement of the output power of the HRF cantilever. Firstly, due to the large area of the PZT film on the HRF cantilever, it is able to generate a much higher electric power. Because the more PZT material patterned, the more power would be generated for the same strain distribution (refer to Appendix B). Secondly, the unfolded beam length of the LRF cantilever is much longer than that of the HRF cantilever. Thus the average strain distribution along the beam length of the LRF cantilever is reduced significantly and

hence results in a lower power output. Lastly, the HRF cantilever has much higher resonant frequency and capacitance comparing with the LRF cantilever, which would result in a extremely low piezoelectric impedance. Hence HRF cantilever is able to transfer much more power to the external load..

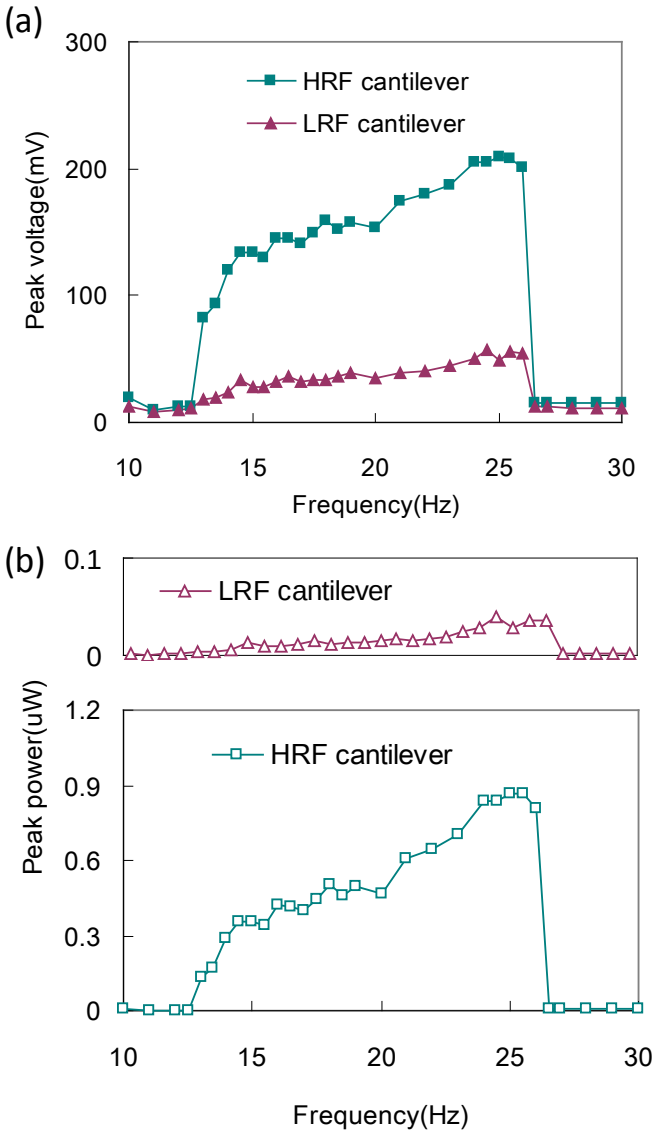

Figure 4.14 (a) Peak voltages and (b) peak power of the LRF and HRF cantilevers against frequencies from 10 to 30 Hz at 0.8 g.

4.3.4 Comparison of PEH-I and PEH-II systems

Table 4.2 shows a summary of the performance of the PEH-I and PEH-II systems in terms of peak-power density and operating bandwidth. Comparing with PEH-I system,

the improved PEH-II system is able to achieve a much higher peak-power density of up to 164.6 μW/cm^3 at frequency of 25 Hz. At present, there is no report of MEMS piezoelectric energy harvesters that is able to achieve a power density of at such level with a low operating frequency of less than 30 Hz. The PEH-II system has also extended the operating bandwidth to 13 Hz (from 13 to 26 Hz) which is near the vibration frequency of human motion (less than 10 Hz). This is an obvious advantage as currently there are still no reports of MEMS piezoelectric energy harvesters operating at such bandwidth range.

Table 4.2 Comparison of PEH-I and PEH-II systems

	EH-I system			EH-II system		
		LRF cantilever	HRF cantilever		Meandered cantilever	Straight cantilever
Peak power (μW)	37 Hz	0.03	0.09	20 Hz	0.003	0.34
	51 Hz	0.06	0.13	25 Hz	0.01	0.87
Cantilever size (mm^3)		8x5x0.4	3x5x0.01		3.25x2x0.4	3.25x2x0.4
Peak power density (μW/cm^3)	37 Hz	7.4		20 Hz	88.8	
	51 Hz	11.8		25 Hz	164.6	
Resonant frequency (Hz)	36			20		
Operation bandwidth (Hz)	22 (30-52)			13 (13-26)		

4.4 Summary

In this chapter, the design, microfabrication, modeling and characterization of FUC vibration-based MEMS PEH-I and PEH-II systems are presented. The devices are able to convert random or irregular low-frequency vibrations to high-frequency oscillations. A mechanical model has been employed and the working principles are

described. The dynamic behavior of both the FUC PEH-I and PEH-II systems are demonstrated experimentally. In the PEH-II system, the HRF cantilever which acts as a FUC oscillator, is triggered by using a LRF cantilever which acts as an excitation oscillator. As a result, the instantaneous output voltage and power of the HRF cantilever show significant improvement over the LRF cantilever. The main advantage of the proposed FUC approach is that it broadens the operating frequency range and increases the output power simultaneously. In addition, it is easy to assemble and does not require the use of extra energy or bulk magnets. For the PEH-I system, the operating bandwidth ranges from 30 to 52 Hz at a base acceleration of 0.8 g and the peak-power density reaches 11.8 $\mu W/cm^3$ at an operating frequency of 51 Hz. For the PEH-II system, the peak-power density increases gradually from 25.8 to 164.6 $\mu W/cm^3$ in a broad frequency range of 13 to 26 Hz at 0.8 g. It is seen that the PEH-II system offers a possible solution for practical application in a low-frequency vibration environment such as that of human motion.

Chapter 5

A 3-D Multi-Frequency Vibration-Based MEMS Energy Harvester

To harvest energy from vibration sources with different frequency peaks, numerous prototypes based on tunable, wideband and multiple-frequency approaches have been discussed in Chapter 2. In general, most of the tunable and wideband energy harvesters operate in a continuous frequency range. In this chapter, the development of a multiple-frequency energy harvester operating at three discrete resonant frequencies is discussed. Most of the reported energy harvesters are designed to scavenge energy only from a single vibration direction. To overcome the limitations of 1-D and 2-D energy harvesting and scavenge energy from vibration sources of different directions, a 3-D vibration-driven electromagnetic MEMS energy harvester with multiple vibration modes has been proposed. The device is capable of scavenging energy from out-of-plane vibrations at mode I as well as in-plane vibrations at modes II and III.

5.1 Design and Fabrication

5.1.1 Device configuration

The proposed 3-D multi-frequency electromagnetic energy harvester is shown schematically in Fig. 5.1 (a). It consists of a movable circular-mass with a diameter of 4.5 mm and a thickness of 450 μm, and is suspended by a circular-ring system. The circular-ring system consists of three concentric rings with a width of 30 μm and a height of 150 μm which are connected to each other at a spacing of 200 μm by a series of junction blocks placed at an interval of 60°. The concentric rings are designed to have the same spring stiffness along in-plane direction, so as to resonate in two orthogonal in-plane directions with nearly the same resonant frequencies.

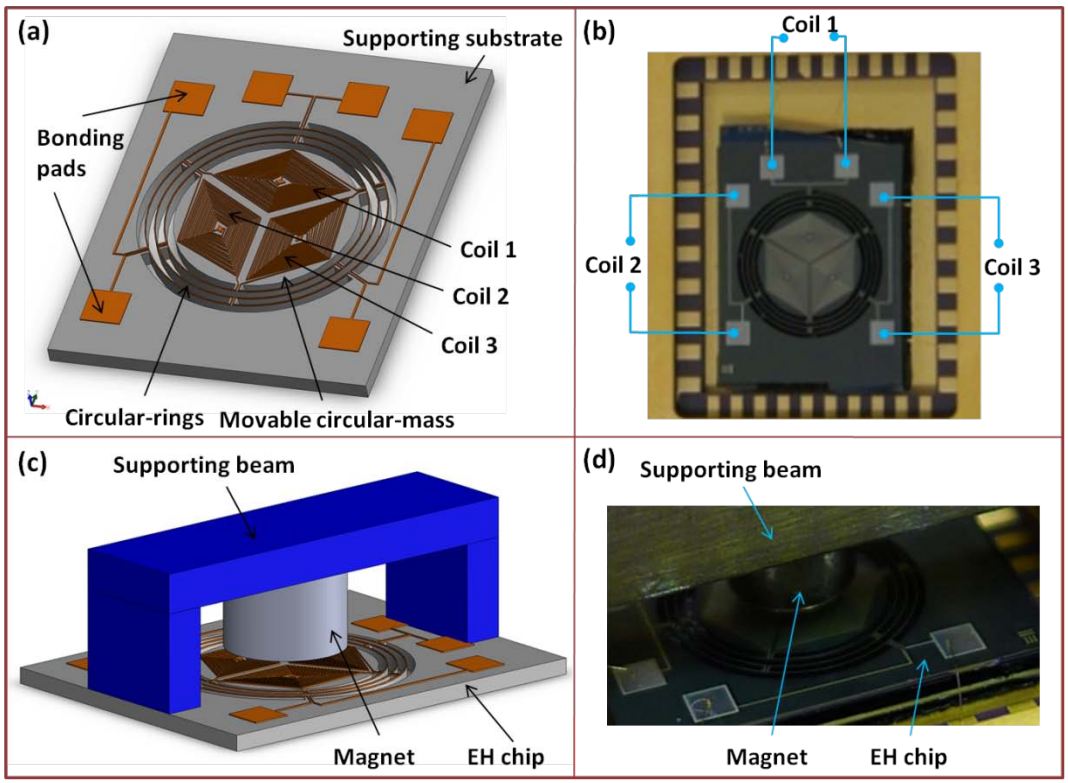

Figure 5.1 (a) A schematic drawing and (b) microfabricated 3-D energy harvester chip; (c) schematic drawing and (d) photograph of the device assembled with magnet.

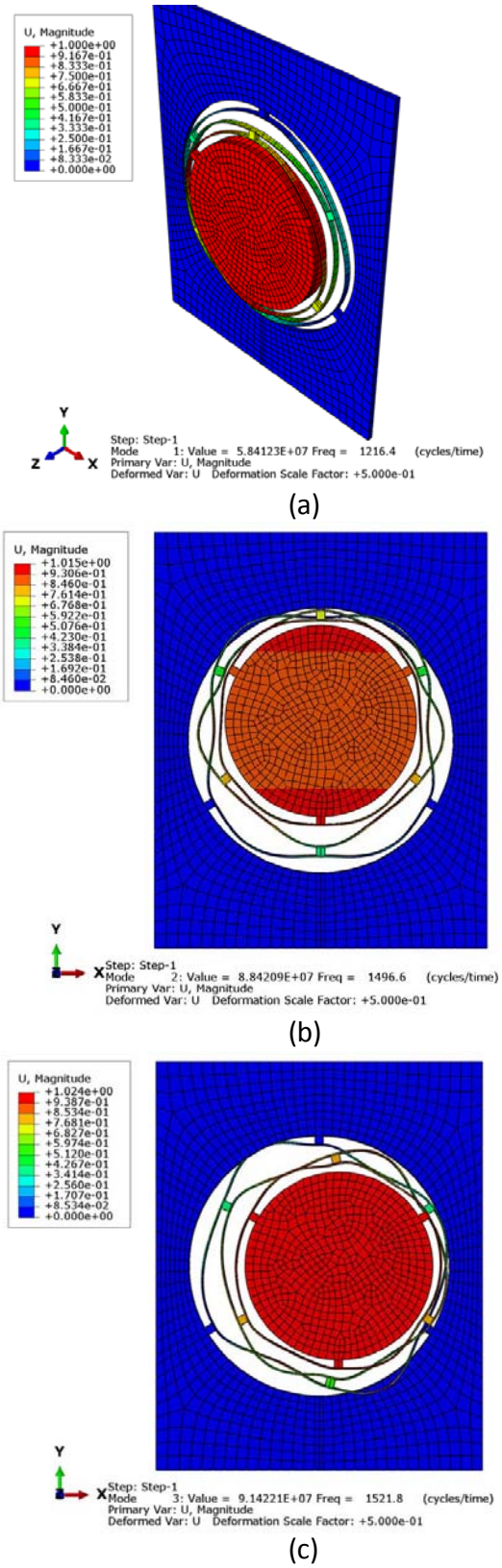

Figure 5.2 Finite element analysis of (a) mode I at 1216 Hz; (b) mode II at 1497 Hz; (c) mode III at 1522 Hz.

Three diamond-shaped Al coils (Coils 1, 2 and 3) are mounted symmetrically about the axes through a 120° sector. Each coil consists of two layers and each layer contains 17 loops of 1X10 μm wires with a spacing of 25 μm between each loop. The coils are connected to their individual bonding pads. The energy harvester is mounted on a spacer chip and assembled onto a DIP which is connected to the bonding pads by gold wires. A permanent magnet of diameter 3 mm and length 2 mm is attached on a supporting beam and is placed on top of the chip with a gap of 1 mm as shown in Figs. 5.1 (c) and (d). When the circular-mass vibrates in-plane or out-of-plane, the relative movement between the coils and magnet will induce an electrical current according to Faraday's law of induction.

A finite element analysis employing Abaqus has been conducted to study the vibration behaviors of the energy harvester. In the simulation, the material properties of the crystal-orientation-dependent Si wafer have elastic stiffness coefficients of C_{11} = 165.6 GPa, C_{12} = 63.9 GPa, C_{44} = 79.5 GPa at room temperature [153]. Figure 5.2 shows the mode shapes of the first three vibration modes (modes I, II and III) corresponding to resonant frequencies of 1216, 1497 and 1522 Hz, respectively. At mode I, the circular-mass oscillates out-of-plane, while at modes II and III, in-plane oscillations occur along the y- and x-axis, respectively. It is seen that the in-plane resonant frequencies of modes II and III are almost similar. The slight difference in frequency of 25 Hz is due to the anisotropy of the material property.

5.1.2 Fabrication process

The process flow of microfabrication is illustrated in Fig. 5.3. A SOI wafer consisting of a 150-μm-thick Si device layer, a 1-μm-thick BOX layer and a 725-μm-thick Si handle layer is in use. In Fig. 5.3 (a), a 0.1-μm-thick Si_3N_4 insulation layer is first

deposited on the frontside surface of the SOI wafer using a plasma-enhanced chemical vapor deposition (PECVD) system (Novellus Sequel^{TM} Express PECVD). A 1-µm-thick Al layer is then deposited by physical vapor deposition (Applied Materials Endura^{TM} HP PVD) followed by RIE process by a Applied Materials Centura Electron Cyclotron Resonance Etcher with a combination gas of C_{12}/BC_{13}/Ar in the ratio of 110:60:15 for patterning the first coil layer and bonding pads using Mask 1 as shown in Fig. 5.3 (b). Subsequently, a 0.8-µm-thick Si_3N_4 insulation layer is deposited by PECVD and pad openings are formed by RIE process by Lam Research Exelan HPT Dielectric Reactive Ion Etcher using Mask 2 as shown in Fig. 5.3 (c). Using Masks 3 and 4, 1-µm-thick Al and 0.8-µm-thick Si_3N_4 are again deposited, patterned and etched to form the second coil layer and contact pads as shown in Fig. 5.3 (d). A 2-µm-thick SiO_2 layer is then deposited on the top surface by Novellus Sequel^{TM} Express PECVD as a passivating and hard mask layer followed by patterning and RIE of the SiO_2, Si_3N_4 layers using CHF_3 (for SiO_2) and CF_4 (for Si_3N_4). As shown in Fig. 5.3 (e), a Si device layer with depth of 150 µm is then DRIE to form the frontside features, such as the circular-mass and rings of the device.

After the frontside processes are completed, the SOI wafer is reduced to approximately 450 µm by backside grinding and polishing. Thus the handle layer thickness is reduced from 725 µm to be around 300 µm. A 2-µm-thick SiO_2 is then deposited on the backside of the wafer as a hard mask layer by Surface Technology Systems PECVD. A thick photoresist layer is subsequently patterned on the SiO_2 layer using Mask 6 followed by a backside Surface Technology Systems DRIE to a maximum depth of 300 µm as shown in Figs. 5.3 (f) and (g). To ensure that the entire Si handle layer is fully etched away, a uniform backside DRIE process is employed and eventually terminated at the BOX layer. Before the DRIE process is carried out,

the wafer is diced into small chip size to avoid breakage during the wet etching and release processes. In Fig. 5.3 (h), the final process involves dry etching of the remaining SiO_2 on the frontside and BOX layers by CHF_3 plasma.

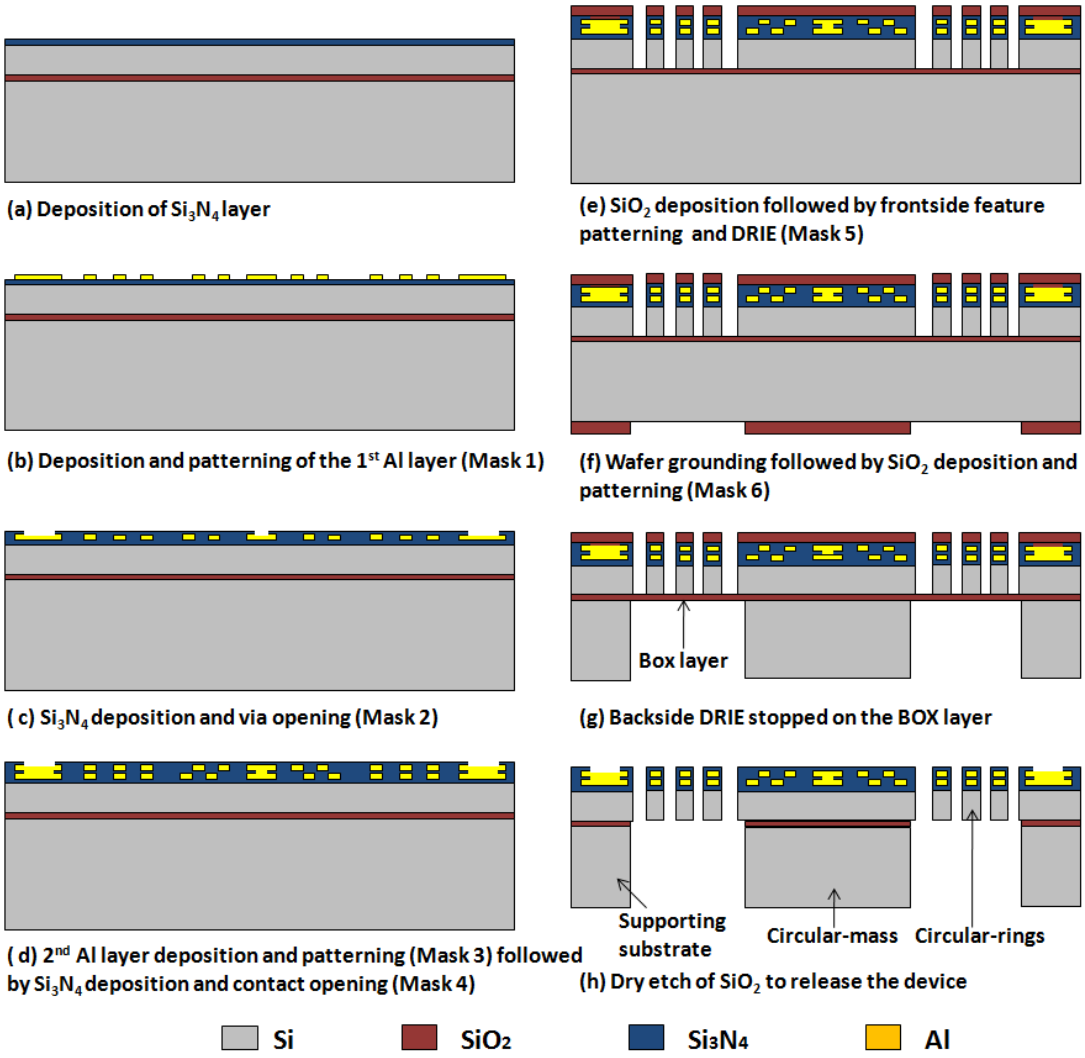

Figure 5.3 Microfabrication processes of the 3-D multi-frequency electromagnetic energy harvester chip.

A scanning electron micrograph (SEM) of the fabricated device is shown (partially) in Fig. 5.4. The enlarged sections indicate that the height of the circular mass has been reduced from 450 μm to less than 400 μm due to over etching of the backside DRIE process. In addition, the width of the circular-ring is reduced from 30 μm to approximately 20~25 μm after the frontside DRIE process. Depending on the

location of the chip on the wafer, the circular-rings may display asymmetrical undercut. Such geometrical imperfection may lead to changes in resonant directions and frequencies [146].

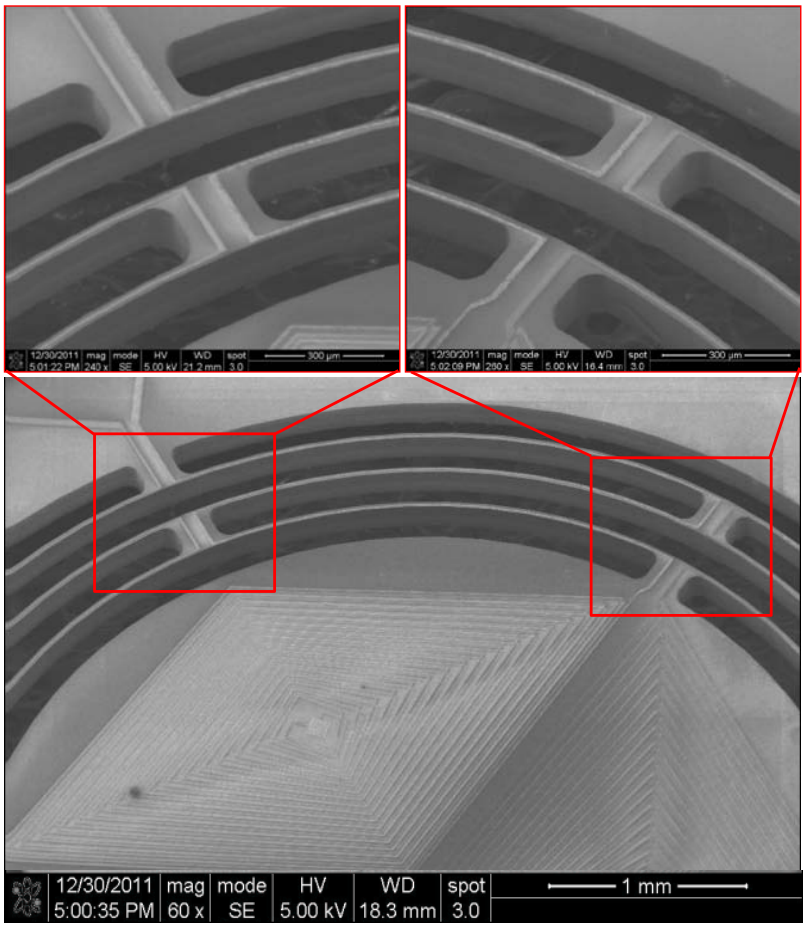

Figure 5.4 SEM images of the fabricated electromagnetic energy harvester chip.

5.2 Modeling and Simulation

5.2.1 Dynamic model

A vibration-based energy harvester can essentially be considered as a second-order mass-spring-damper system as discussed in the previous chapter. The differential equation of mass motion is determined by Newton's Second Law as

$$M\ddot{Z}(t) + C\dot{Z}(t) + KZ(t) = -M\ddot{Y}(t) \tag{5.1}$$

where *M*, *K*, and *C* are the mass, spring stiffness and damping factor of the system, respectively; *Z(t)* is the relative displacement of the mass with respect to the supporting base; $Y(t) = Y\sin(\omega t)$ is a harmonic excitation applied to the system with excitation amplitude *Y* and frequency ω.

The relative displacement of mass motion *Z(t)* can be derived from the steady-state solution of Eq. (5.1) and is expressed as

$$Z(t) = \frac{Y(\omega/\omega_n)^2}{\sqrt{(1-(\omega/\omega_n)^2)^2 + (2\varsigma(\omega/\omega_n))^2}}\sin(\omega t - \varphi) \tag{5.2}$$

where ω_n is the resonant frequency of the system $\omega_n = 2\pi f_r = \sqrt{K/M}$; ς is the overall damping ratio $2\varsigma\omega_n = C/M$; φ is the phase angle between the base excitation and mass motion. From Eq. (5.2), the relative velocity of mass motion is given by

$$\dot{Z}(t) = \frac{Y\omega(\omega/\omega_n)^2}{\sqrt{(1-(\omega/\omega_n)^2)^2 + (2\varsigma(\omega/\omega_n))^2}}\cos(\omega t - \varphi) \tag{5.3}$$

When the excitation frequency and direction matches with the resonant frequency and direction of the system at one of the vibration modes ($\omega = \omega_n$), the relative displacement and velocity of mass motion are given by

$$Z(t) = \frac{Y}{2\varsigma}\sin(\omega_n t - \varphi) \tag{5.4}$$

$$\dot{Z}(t) = \frac{Y\omega_n}{2\varsigma}\cos(\omega_n t - \varphi) \tag{5.5}$$

5.2.2 Electro-magnetic model

An electro-magnetic model of the proposed 3-D multi-frequency electromagnetic energy harvester is constructed to calculate the vibration-induced voltage and power.

Figure 5.5 shows a schematic illustration of the top view of a circular mass with three coils (Coils 1, 2 and 3) placed in a magnetic field which is assumed to be uniform with strength $\vec{B}$ in area A_B (shaded area). Each coil consists of two layers and each layer contains 17 loops (shown as 2 loops of a layer for simplicity). Since the magnetic field covers a smaller area than that of the circular mass, some loops would fall outside the magnetic field.

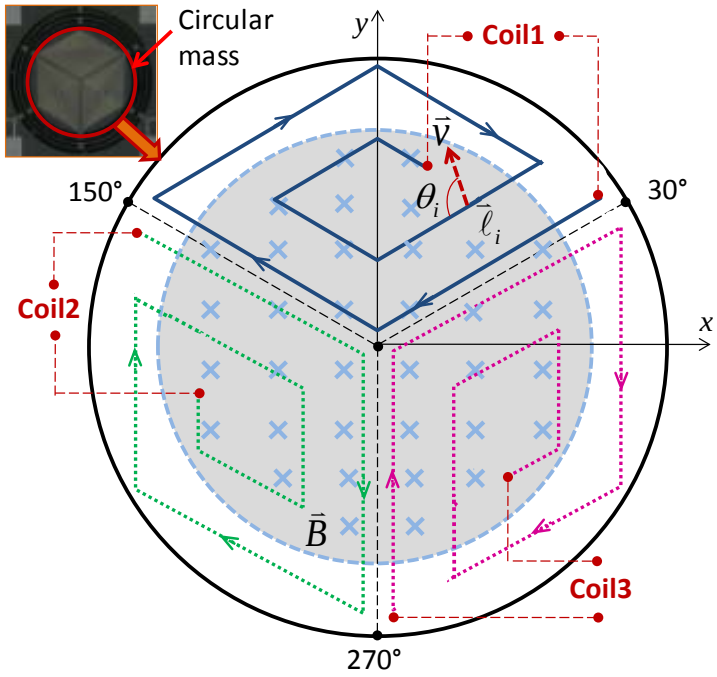

Figure 5.5 Schematic drawing of the top view of a vibrating mass with coils (Coils 1, 2 and 3) placed in a magnetic field.

According to Faraday's law of induction, the electromotive force (emf) ε of a coil is proportional to the negative of the rate of change of the magnetic flux as

$$\varepsilon = -\frac{d\Phi}{dt} = -\frac{d}{dt}\sum_{i=1}^{n}(\vec{B}\cdot\vec{A}_i) \tag{5.6}$$

Equation (5.6) can further be expanded to give

$$\varepsilon = -\sum_{i=1}^{n}\frac{d\vec{B}}{dt}\cdot\vec{A}_i - \sum_{i=1}^{n}\vec{B}\cdot\frac{d\vec{A}_i}{dt} \tag{5.7}$$

where Φ is the magnetic flux density; *t* is the time; *i* is the order number of each loop; *n* is the total number of loops of a coil; A_i is the magnetic field area included in the *i*-th loop. Equation (5.7) is a general expression of the vibration-induced voltage, which includes both the change of the magnetic field strength and the area in each loop.

In the out-of-plane motion (mode I), the magnetic field area A_i included in each loop is assumed constant, thus the second term is ignored and a simplified induced voltage ε_{out} by out-of-plane motion is given by

$$\varepsilon_{out} = -\frac{dB}{dt}\sum_{i=1}^{n} A_i \tag{5.8}$$

For the first vibration mode, as shown in Eq. (5.8), the out-of-plane vibration-induced voltage is related to the rate of change of the magnetic field strength as well as the total effective magnetic field area of a coil. For a cylindrical magnet, the magnetic field strength *B(t)* is given by [154]

$$B(t) = \frac{B_r}{2}\left[\frac{(d(t)+h)}{[r^2+(d(t)+h)^2]^{1/2}} - \frac{d(t)}{[r^2+d(t)^2]^{1/2}}\right] \tag{5.9}$$

where B_r is the residual magnetic field strength; *r* and *h* are the radius and length of the magnet, respectively; *d(t)* is the gap distance from the coil to the magnet. The variation of the gap distance *d(t)* is related to the difference between the initial gap d_0 and the vertical mass motion. Hence, the rate of change of the magnetic field strength $\dot{B}(t)$ can be obtained. The total magnetic area A_i of each coil can be calculated numerically and subsequently the out-of-plane vibration-induced voltage ε_{out}.

For the in-plane motion (modes II and III), the magnetic field strength of each coil is assumed uniform. Thus the first term of Eq. (5.7) is ignored and the induced voltage ε_{in} by in-plane motion is given by

$$\varepsilon_{in} = -B\sum_{i=1}^{n}\frac{dA_i}{dt} = -\sum_{i=1}^{n} Bvl_i \sin\theta_i \tag{5.10}$$

where l_i is the effective length of each loop included in the electromagnetic field; θ_i is the angle between the in-plane velocity v and the induced current direction along each wire. In our design, a coil loop consists of four wires. Hence, in a given loop, angle θ_i in each wire could vary. The effective coil length and angle θ_i are determined numerically and subsequently the induced voltage ε_{in} by in-plane motion is obtained using Eq. (5.10).

5.2.3 Simulation of induced voltage due to in-plane motion

To study the induced voltage of each coil due to an in-plane motion, the circular-mass is assumed to move in an arbitrary direction at a constant velocity of 0.3 m/s^2. For a gap distance of 0.5 mm between the magnet and the circular-mass, the electromagnetic field strength is 0.2 T according to Eq. (5.9). Figure 5.6 (a) shows the induced voltages of Coils 1, 2 and 3 obtained based on Eq. (5.10) in a polar coordinate system, where the polar radius represents the rms voltage value of each coil and the angular values represent the directions of the mass motion with respect to the x-axis. As seen, the maximum voltages of Coils 1, 2 and 3 occur at angles of 90° (270°), 30° (210°) and 150° (330°), respectively, while the minimum voltages occur at angles perpendicular to these angles. For a mass motion along 60° (240°) direction, Coils 1 and 2 show similar output voltages as indicated by points A and A'. However, at this angle there is little or no voltage output in Coil 3 as indicated by point O. When the mass motion is at an angle of 150° (330°), the output voltage of Coil 3 is maximum as indicated by point B and B', which is more than twice that of Coi1s 1 and 2 as indicated by point C and C'. The similar voltage output of Coils 1 and 2 at

angles of 60° (240°) and 150° (330°) are due to their symmetrical layout along the 150° (330°) axis as indicated in Fig. 5.5 (a). The coils experience a similar change of magnetic flux when the mass moves along these two axes. In between these axes, Coil 1 produces more voltage output or less than Coil 2 since it experiences more changes of magnetic flux or less than Coil 2. For Coil 3, it would experience a maximum change of magnetic flux when the mass moves along the 150° (330°) axis and a minimum when it moves along the 60° (240°) axis.

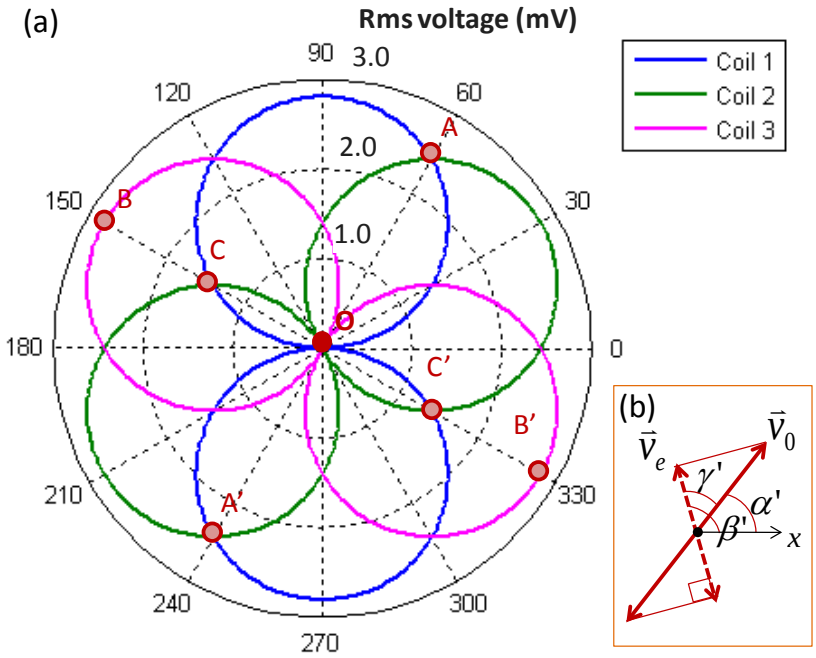

Figure 5.6 (a) Output voltage of each coil with respect to the in-plane mass motion; (b) schematic illustration of the relationship between the input velocity and the resultant driving velocity at resonant mode.

The above discussion is based on the assumption of a constant value of mass-motion velocity. It is important to note that the resultant mass motion is not only influenced by the external excitation but also dependent on the resonant mode of the energy harvester. Figure 5.6 (b) shows an input excitation velocity of $\vec{v}_0$ at an angle α' and a resonant mode at an angle β'. From Eq. (5.5), the mass-motion velocity at

resonance can be written as $v_r(t) = \frac{v_0 \cos(\gamma')}{2\varsigma} \cos(\omega_n t - \varphi)$, where $\gamma' = \beta' - \alpha'$ is the angle between the input velocity and the resonant mode, and the resultant driving velocity $\vec{v}_e$ is given by $v_e = v_0 \cos(\gamma')$.

5.3 Experimental Work and Discussion

5.3.1 Experimental setup

The experimental setup includes a shaker, a power amplifier, an accelerometer and a DSA coupled to a computer through a GPIB port. The device is attached to a breadboard and mounted on a rotation stage. As shown in Fig. 5.7, the rotation stage is assembled onto a L-shaped holder to perform both out-of-plane (setup (a)) and in-plane motions (setup (b)). As the 3-D energy harvester device is excited with different frequencies, amplitudes and directions, the generated voltages of each of the three coils are recorded by different channels of the DSA and the computer as well.

5.3.2 Out-of-plane behavior (mode I)

Based on experimental setup (a), the out-of-plane motion induced voltages of Coils 1, 2 and 3 for excitation frequencies of 1200 to 1400 Hz at acceleration of 1.0 g are shown in Fig. 5.8. As the permanent magnet is placed above the center of the vibrating-mass, the coils experience similar magnet flux change and hence would generate similar output voltages (around 3.5~3.6 mV at resonant frequency of 1285 Hz). It is noted that the mode I (frequency of 1285 Hz) is about 5.7% higher than the simulated result of 1216 Hz (as shown in Fig. 5.2). The slight discrepancy is due to the difference in the material property as well as a slight variation in the dimensions

of the actual fabricated device. The simulated voltage ε_{out} of a single coil obtained using Eq. (5.8) is also included in the figure, and the results agree well with the experimental data. Details of the various parameters used in the simulation are given in Table 5.1.

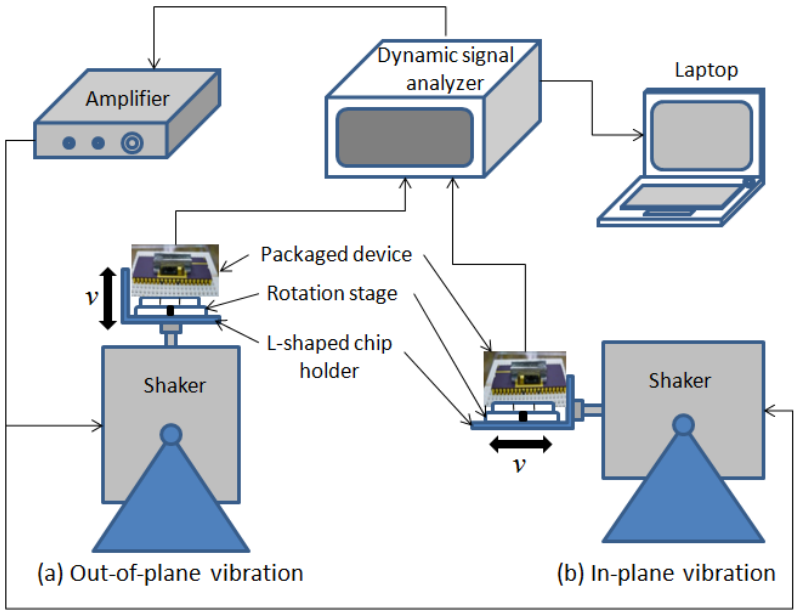

Figure 5.7 Schematic illustrations of experimental setup for (a) out-of-plane and (b) in-plane excitations.

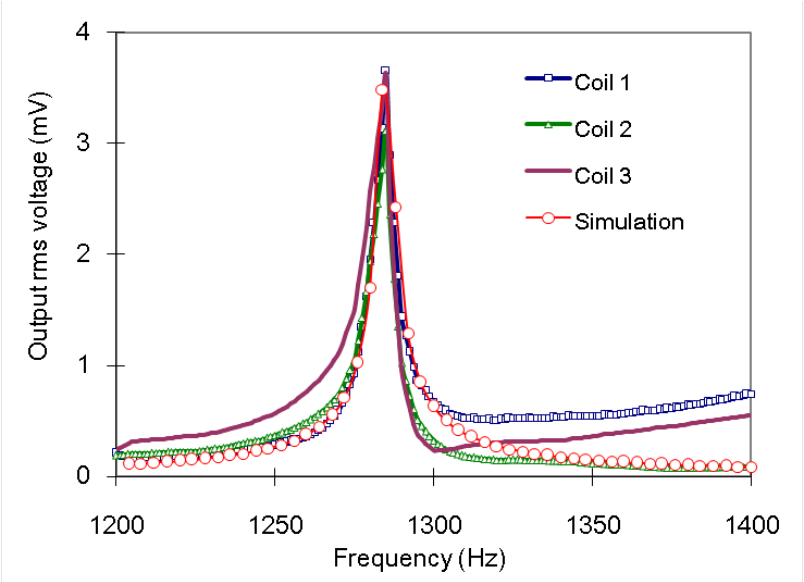

Figure 5.8 Experimental and simulated output voltages at excitation frequencies of 1200 to 1400 Hz with out-of-plane input acceleration of 1.0 g.

Table 5.1 Structural and simulation parameters of the 3-D energy harvester device

Structural and simulation parameters	Values
Magnet type	NeFeB (1.2T)
Magnet diameter	3 mm
Magnet height	2 mm
Initial gap distance	1 mm
Circular-rings width	30 μm
Circular-rings thickness	150 μm
Circular-rings spacing	200 μm
Metal line width	10 μm
Metal line thickness	1 μm
Metal lines spacing	25 μm
Coil turns of each layer	17
Resistance of Coil 1	640 Ω
Resistance of Coil 2	600 Ω
Resistance of Coil 3	560 Ω
Circular-mass diameter	4.5 mm
Circular-mass thickness	450 μm
Overall damping ratio	0.0018
Chip size	10 x 8 x 0.45 mm^3

When the coils are connected in series and the out-of-plane excitation is at mode I resonance of 1285 Hz and acceleration of 1.0 g, the overall output rms voltage and power for various load resistances are shown in Fig. 5.9. As can be seen, the output voltage increases monotonically as the load resistance increases. When the load resistance matches the total internal resistance of 1.8 kΩ, a maximum output power of 0.016 μW is achieved. This translates into a power density of 0.444 $\mu W/cm^3$, which is obtained from the output power normalized by the chip volume.

5.3.3 In-plane behavior (modes II and III)

By using experimental setup (b), the output voltages at excitation frequencies of 1200 to 1700 Hz and acceleration of 1.0 g are recorded at different in-plane excitation

angles in increment of 30°. From the simulated results, modes II and III are expected to occur along the y- and x- directions, respectively. In reality, due to the material anisotropy and variation in the dimensions of the actual fabricated device, they occur at angles of 60° (240°) and 150° (330°). Hence, the device is excited at angles of 60° and 150°, and the output rms voltages as a function of the frequency are shown in Fig. 5.10.

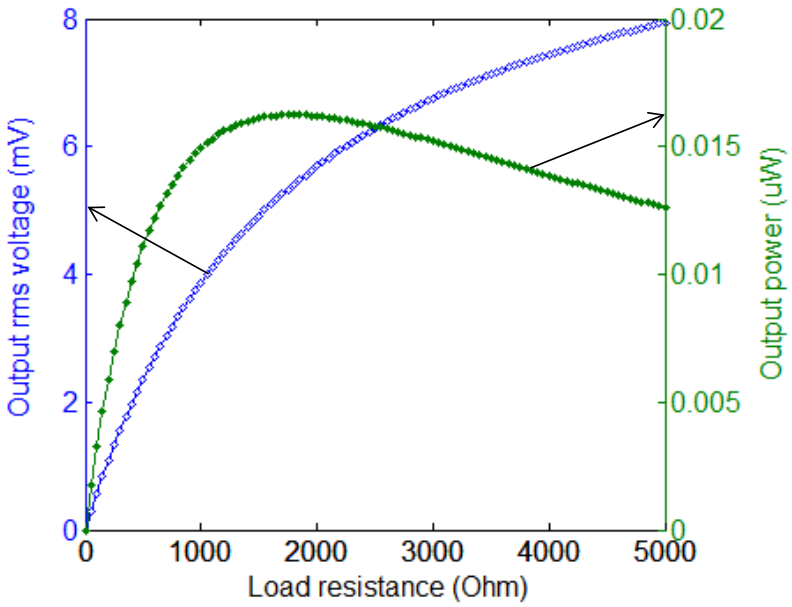

Figure 5.9 Overall output rms voltage and power against load resistance at mode I.

As shown in Fig. 5.10 (a), at excitation angle of 60°, the rms peak voltage of Coils 1 and 2 at mode II frequency of 1470 Hz are 3.6 and 2.9 mV, respectively, while the peak voltage of Coil 3 at mode II is not very obvious. At mode III frequency of 1550 Hz, the peak voltage of Coil 3 is only 0.26 mV, while the peak voltages of Coils 1 and 2 are hardly noticeable. A tentative inference on this figure is that the resonant mode II of the device occurs along angle of 60° (240°), while mode III is perpendicular to this angle as 150° (330°). Based on the simulation results as shown in Fig. 5.6, for mode II at angle of 60°, the excitation angle is just along the mode II direction. The output voltages of Coils 1 and 2 reach the maximum values, while that

of Coil 3 is almost zero. For mode III at angle of 150°, since the excitation angle of 60° is perpendicular to mode III direction, the resultant driving velocity at angle of 150° would be quite small. Hence, the voltage peaks of Coils 1, 2 and 3 are not very obvious for mode III.

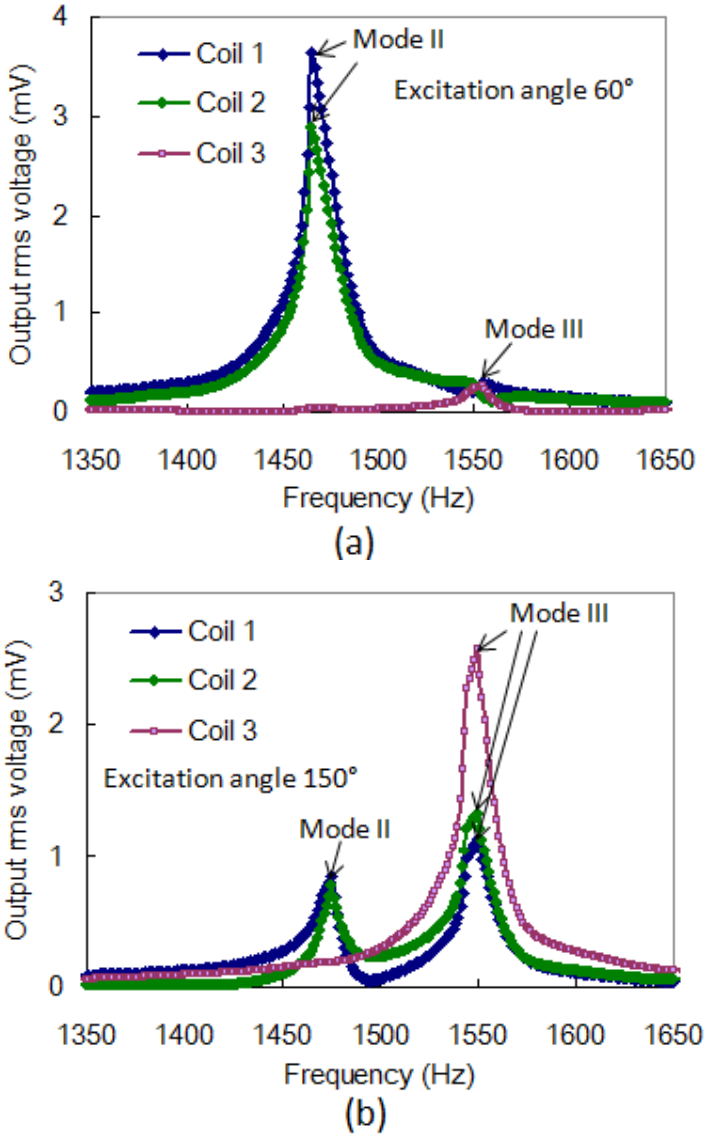

Figure 5.10 Output rms voltages with an input acceleration of 1.0 g as a function of frequency at excitation angles of (a) 60° and (b) 150°.

In Fig. 5.10 (b), at an excitation angle of 150°, a peak voltage of 2.6 mV is generated by Coil 3 at mode III. For Coils 1 and 2, peak voltages are also observed at both modes II and III resonance. Similarly, a tentative explanation on this figure is

that the excitation angle is just along the mode III direction at angle of 150°. Coil 3 reaches its maximum output voltage, which is about twice that of Coi1s 1 and 2. While similar voltage outputs of Coils 1 and 2 are obtained due to their symmetrical layout along the 150° axis. The results also indicate that at both excitation angles of 60° and 150°, the simulated frequencies of 1497 Hz (mode II) and 1522 Hz (mode III) agree well with the measured values to within 1.8%.

To further study the performance of the device, the output rms voltages excited at modes II and III resonance at excitation angles ranging from 0° to 180° in increment of 30° are shown in Fig. 5.11. Since the harmonic excitations from 180° to 360° show identical response due to symmetry, the data are extended to the full range of 360°. For mode II resonance at frequency of 1470 Hz, the experimental results represented as E-Coils 1, 2 and 3 are shown in Fig. 5.11 (a), while the simulation results (using Eq. (5.10)) are shown as S-Coils 1, 2 and 3. The parameters used in simulation are as shown in Table 5.1. The simulated results of Coils 1 and 2 (in red solid line) are similar and generally agree well with the experimental data, while the simulated voltage output of Coil 3 (in red dash line) is almost zero and hence is hardly noticeable in the figure.

From the experimental results, it is seen that at an excitation angle of 60° (240°), Coils 1 and 2 exhibit similar output characteristics with maximum voltages of 3.6 mV (Coil 1) and 2.9 mV (Coil 2). While at an excitation angle of 150° (330°) which is perpendicular to 60° (240°), the output voltages generated are at their minimum of 0.8 mV (Coil 1) and 0.7 mV (Coil 2). The output voltage decreases gradually from the peak value to the minimum as the excitation angle changes from 60° (240°) to 150° (330°). For Coil 3, the output voltage at any excitation angle is generally negligible.

This figure fully validates the previous inference that the resonant mode II of the device occurs along angle of 60° (240°).

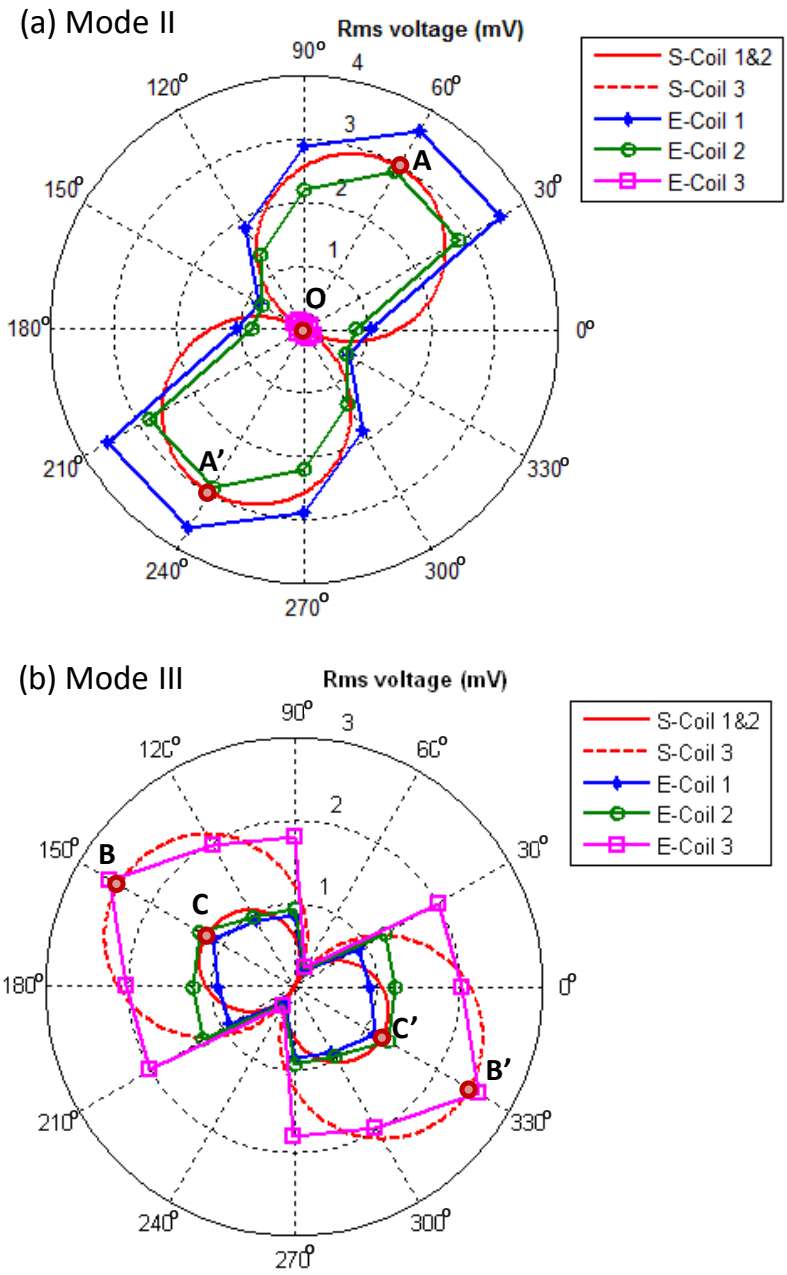

Figure 5.11 Experimental and simulated output voltages with input acceleration of 1 g as a function of excitation angle α for modes (a) II and (b) III.

Similarly, the experimental and simulated output voltages of the coils for mode III resonance at frequency of 1550 Hz are shown in Fig. 5.11 (b). At excitation angle of 150° (330°), the measured maximum output voltage of Coils 1, 2 and 3 are 1.1, 1.3

and 2.6 mV, respectively. The minimum output voltages of these coils are only 0.2~0.3 mV at a perpendicular excitation angle of 60° (240°). In general, the simulated results agree well with the experimental. This figure again confirms that the resonant mode III of the device occurs along angle of 150° (330°).

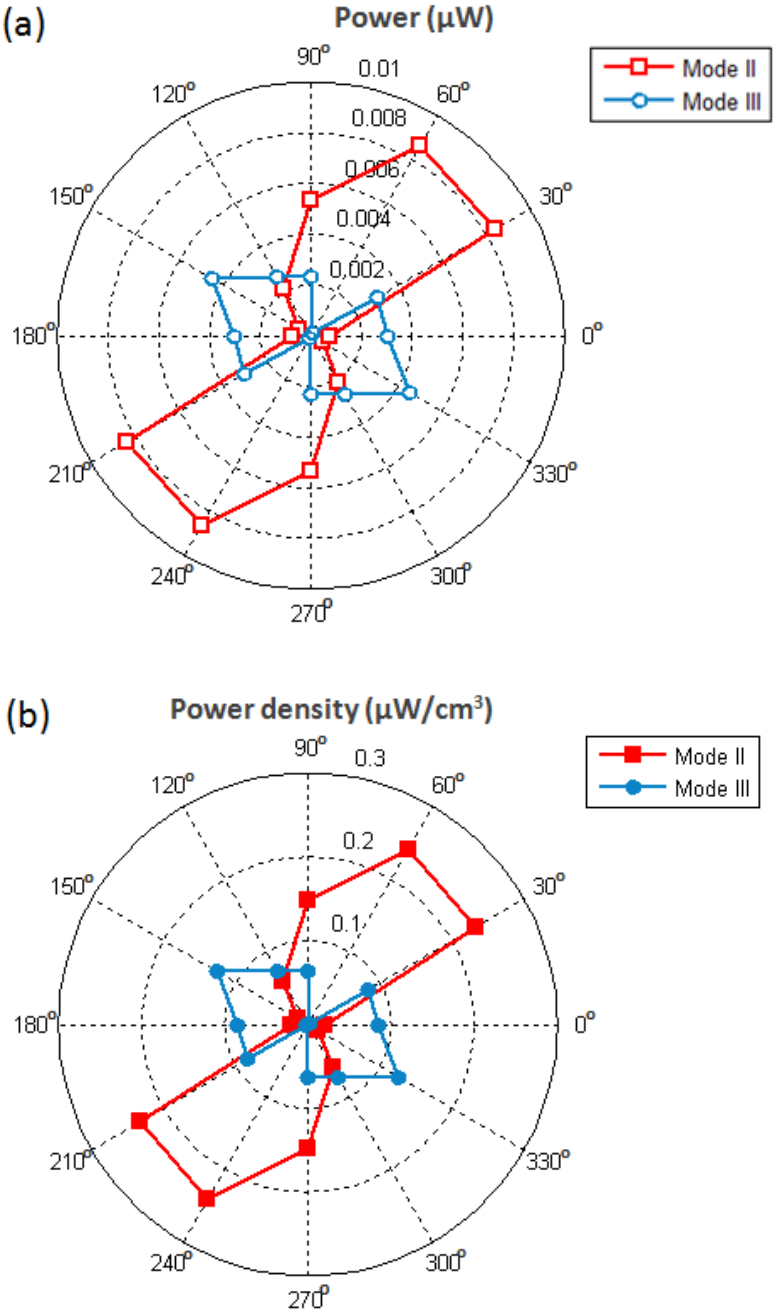

Figure 5.12 Calculated overall optimum (a) power and (b) power density for modes II and III with respect to different excitation angles at input acceleration of 1 g.

From the measured voltages for both modes II and III, the optimum power of each coil is calculated when the load resistance matches with the coil resistance. The overall optimum power (sum of the optimum power of Coils 1, 2 and 3) for modes II and III with respect to different excitation angles are shown in Fig. 5.12 (a). The corresponding power densities are shown in Fig. 5.12(b). As expected the maximum power and power densities for both modes II and III correspond to their respective maximum voltage directions at 60° (240°) and 150° (330°), respectively. Other than the resonance angle, the power generation decreases gradually and reaches its minimum value at the angle just perpendicular to its resonance angle. For mode II, the maximum power and power density obtained are approximately 0.0087 μW and 0.242 μW/cm^3, respectively, while for mode III, the maximum power of 0.0045 μW and power density of 0.125 μW/cm^3 achieved are only about half of those for mode II.

Table 5.2 Experimental results of vibration behavior and output performance of the 3-D multi-frequency energy harvester device

		Mode I	**Mode II**	**Mode III**
Mode shape		z-axis (out-of-plane)	60° to x-axis (in-plane)	150° to x-axis (in-plane)
Resonant frequency (Hz)		1285	1480	1550
Peak rms voltage (mV)	Coil 1	3.6	3.6	1.1
	Coil 2	3.5	2.9	1.3
	Coil 3	3.6	0.04	2.6
Maximum power (μW)		0.016	0.0087	0.0045
Power density (μW/cm^3)		0.444	0.242	0.125

The overall vibration performance of the proposed 3-D multi-frequency energy harvester is summarized in Table 5.2. As can be seen, the device exhibits out-of-plane and in-plane (3-D) resonance vibrations along z-axis (mode I of frequency 1285 Hz),

60° (mode II of frequency 1470 Hz) and 150° (mode III of frequency 1550 Hz) with respect to x-axis, respectively. The optimized power of the device for modes I, II and III are 0.016, 0.0087, and 0.0045 μW, respectively, at excitation acceleration of 1.0 g. Accordingly, the power densities for these three modes are 0.444, 0.242, and 0.125 $\mu W/cm^3$, respectively.

5.4 Summary

The design, fabrication and characterization of a 3-D MEMS electromagnetic energy harvester with multiple resonant frequencies have been described. Electro-magnetic model has been built for both out-of-plane and in-plane vibration-induced voltages of Coils 1, 2 and 3. The simulations show that for Coils 1, 2 and 3, the maximum voltages were induced at angles of 90° (270°), 30° (210°) and 150° (330°), respectively. The device is characterized by both out-of-plane and in-plane excitations with three vibration modes (modes I, II and III) which are perpendicular to each other at resonant frequencies of 1285, 1470 and 1550 Hz. Experiments show that the directions of the three resonance modes are along the z-axis (mode I), and at 60° (mode II) and 150° (mode III). The overall optimized power are respectively 0.016, 0.0087 and 0.0045 μW at an acceleration of 1.0 g. The power output could further be improved by increasing the excitation acceleration, the number of coils and layers and the magnetic field strength. With further optimization in the design and dimensional parameters, it is expected that the three vibration modes would be brought nearer to a common resonant frequency. This would improve the effectiveness in harvesting ambient kinetic energy. The results have shown a good potential for realizing a practical 3-D vibration-driven energy harvester device.

Chapter 6

Conclusions and Recommendations

6.1 Conclusions on Current Work

This thesis covers the work done on design and development of various vibration-based MEMS energy harvesters for sustaining self-autonomous wireless sensor nodes. The main focus of this research is to explore and investigate new MEMS-based energy harvesting mechanisms for resolving current problems on environmental vibrations of low and random frequencies in multiple directions.

Wideband energy harvesters are highly desirable for scavenging energy from random and irregular environmental vibrations. In this work, we have designed and developed a piezoelectric MEMS energy harvester with wide operating range by using mechanical stoppers. Analytical and experimental investigations on broad frequency response of the system with stoppers on one side (configuration I) and two sides (configuration II) have been conducted. The key parameters for the frequency response, including base acceleration, damping ratio, frequency characteristic and stopper distance, have been studied. The system has achieved wideband range of 32-42 Hz (for configuration I with bottom-stopper distance of 1.1 mm) and 30-48 Hz (for configuration II with top-stopper distance of 0.75 mm and bottom-stopper distance of 1.1 mm) with respect to a center operating frequency of 36 Hz at

acceleration of 0.6 g. In terms of NFB, the proposed wideband PEH system has realized a much higher NFB of 0.28 (configuration I) and 0.5 (configuration II) than other reported energy harvesters. It is also noteworthy that the system provides a major advantage of achieving both frequency wideband and FUC behaviors at the same time.

FUC energy harvesters, which convert ambient low-frequency excitations into high-frequency self-oscillations, have been introduced to boost the output power of the devices. In this work, FUC MEMS energy harvester systems (PEH-I and PEH-II), which are able to convert the low-frequency of 36 Hz (PEH-I) and 20 Hz (PEH-II) of the excitation oscillators to high-frequency self-oscillations of 618 Hz (PEH-I) and 127 Hz (PEH-II) by incorporating piezoelectric MEMS FUC cantilevers have been developed. The operation principle has been demonstrated and a mechanical model has been employed to simulate the dynamic behavior. In the PEH-II system, it is seen that a significant improvement in the output power has been achieved. The main advantage of the proposed FUC approach is that it broadens the operating frequency range and increases the output power simultaneously. In addition, the proposed FUC energy harvester systems have quite low operating frequency of less than 50 Hz, which is not seen in other piezoelectric MEMS energy harvesters. Hence, the design offers a possible solution for harvesting energy from extremely low-frequency vibrations such as that of human motion.

A 3-D multi-frequency energy harvester has also been designed and the device is able to scavenge energy from out-of-plane vibration in mode I frequency of 1285 Hz as well as in-plane vibration in mode II frequency of 1470 Hz and mode III frequency of 1550 Hz. These three vibration modes are perpendicular to each other along the z-axis (mode I), and at 60° (mode II) and 150° (mode III) to the x-axis. The simulation

results of the output voltages for Coils 1, 2 and 3 based on an electro-magnetic model show good agreement with the experimental results. Overall optimized power densities of 0.444, 0.242 and 0.125 μW/cm^3 at modes I, II and III were achieved. The results have shown a good potential for realizing a practical 3-D vibration-driven energy harvester device.

6.2 Recommendations for Future Work

Energy harvesting is a clean and renewable power solution for wireless sensor networks. There is a wide variety of applications that could greatly benefit from vibration-based MEMS energy harvesters. Currently, a wide coverage of studies together with depth investigations on critical issues have been carried out, including wideband, FUC and 3-D, for realizing not only higher output power but also wider operating variance for adapting to various vibration scenarios. However, a few issues have yet to be addressed with rooms for further improvements and optimization.

In the current reported wideband energy harvesters, most achieve a broad operating range at the expense of a reduced power output. A new concept to replace the mechanical stoppers with piezoelectric FUC cantilevers for achieving both wideband and FUC behaviors at the same time has been demonstrated. As a result, the system could not only respond to low and random frequency vibrations, but also have significant power improvement. However, the author's current study is evaluated by incorporating two PZT cantilevers assembled together mechanically. Other integrated design configurations with optimized stopper distance and frequency characteristics could be developed using the MEMS fabrication and chip-to-chip bonding technique. With further reduced device volume and optimized parameters, the integrated system would be more effective for harvesting vibration energy. If a packaged device with

reduced operating frequency is able to be attached on the human body, such as fingers, hand wrists or limbs, this energy harvesting system would respond to irregular vibrations from human movements in a wide frequency range of around 10 Hz.

The proposed 3-D multi-frequency MEMS energy harvester operates at relatively high frequencies, which limits its application in common vibration sources of less than 200 Hz. Thus a compliance structure design is required by either reducing the width and thickness of the circular-rings, or increasing the circular-mass and the numbers of circular-rings. Another solution for compliance structure is to use polymer-based spring structure with low Young's modulus for replacing Si springs. Both methods would introduce the microfabrication challenge to some extent. In addition, the power output could further be improved by increasing the number of coils and layers and optimizing the coil layout and magnets arrangement. By further optimizing the design and dimensional parameters, it is expected that the three vibration modes would be brought nearer to a low resonant frequency which would improve the effectiveness in harvesting the ambient kinetic energy from a 3-D vibration sources.

The energy conversion coefficients of current reported MEMS energy harvesters based on piezoelectric, electromagnetic and electrostatic mechanisms are restricted by the conversion mechanisms themselves. To further improve the power efficiency, ZnO nanowires have been considered as a promising candidate for piezoelectric-based energy harvesting. A research group in Georgia Tech has successfully fabricated high-output flexible nanogenerators using horizontally aligned ZnO nanowire arrays [155-156]. The electrical output reached a peak power density of ~11 mW/cm^3, which is 10-20 times of that from PZT-based energy harvesters. By integrating with laterally-arrayed ZnO nanowires on top of a low-frequency MEMS cantilever, the power generated due to vibrations could significantly be enhanced.

Bibliography

[1] N. Maluf, and K. Williams, “An Introduction to Microelectromechanical Systems Engineering”, London: Artech House, 2004.

[2] S. Beeby, G. Ensell, M. Kraft, and N. White, “MEMS Mechanical Sensors”, London: Artech House, 2004.

[3] N.C. Tien, A. Ongkodjojo, R.C. Roberts, and D. Li, “The future of MEMS in energy technologies”, *International Conference on Solid-State and Integrated Circuits Technology Proceedings*, pp.2452-2455, 2008.

[4] I. F. Akyildiz, W. Su, Y. Sankarasubramaniam, and E. Cayirci, “Wireless sensor networks: a survey”, *Computer Networks*, vol. 38, no. 4, pp. 393-422, 2002.

[5] D. Culler, D. Estrin, and M. Srivastava, “Overview of sensor networks”, *IEEE Computer*, vol. 37, no. 8, pp. 4149, 2004.

[6] I. F. Akyildiz, W. L. Su, S. Yogesh, and C. Erdal, “A survey on sensor networks”, *IEEE Communications Magazine*, vol. 40, no. 8, pp. 102114, 2002.

[7] C. O. Mathuna, T. O’Donnell, R. V. Martinez-Catala, J. Rohan, and B. O’Flynn, “Energy scavenging for long-term deployable wireless sensor networks”, *Talanta*, vol. 75, no. 3, pp. 613-623, 2008.

[8] S. J. Roundy, “Energy scavenging for wireless sensor nodes with a focus on vibration to electricity conversion”, *Ph.D. Thesis*, University of California, Berkeley, 2003.

[9] V. Raghunathan, S. Ganeriwal, and M. Srivastava, “Emerging techniques for long lived wireless sensor networks”, *IEEE Communications Magazine*, vol. 44, no. 4, pp. 108-114, 2006.

[10] D. Niyato, E. Hossain, M. M. Rashid, and V. K. Bhargava, “Wireless sensor networks with energy harvesting technologies: a game-theoretic approach to optimal energy management”, *IEEE Wireless Communications*, vol. 14, no. 4, pp. 90-96, 2007.

[11] J. P. Thomas, M. A. Qidwai, and J. C. Kellogg, “Energy scavenging for small-scale unmanned systems”, *Journal of Power Sources*, vol. 159, no. 2, pp. 1494-1509, 2006.

[12] Y. K. Tan, “Analysis, design and implementation of energy harvesting systems for wireless sensor nodes”, *Ph.D. Thesis*, National University of Singapore, Singapore, 2010.

[13] J. B. Lee, Z. Chen, M. G. Allen, A. Rohatgi, and R. Arya, “A high voltage solar cell array as an electrostatic MEMS power supply”, *Micro Electro Mechanical Systems, Proceedings of IEEE Workshop*, pp. 331-336, 1994.

[14] J. F. Randall, “On the Use of Photovoltaic Ambient Energy Sources for Powering Indoor Electronic Devices”, *Ph.D. Thesis*, Swiss Federal Institute of Technology, Lausanne, Switzerland, 2003.

[15] M. A. Green, K. Emery, Y. Hisikawa, and W. Warta, “SHORT COMMUNICATION Solar cell efficiency tables (version 30)”, *Progress in Photovoltaics: Research and Applications*, vol. 15, no. 5, pp. 425-430, 2007.

[16] J. F. Randall, and J. Jacot, “Is AM1.5 applicable in practice? Modelling eight photovoltaic materials with respect to light intensity and two spectra”, *Renewable Energy*, vol. 28, no. 12, pp. 1851-1864, 2003.

[17] M. Stordeur, and I. Stark, “Low power thermoelectric generator – self-sufficient energy supply for micro systems”, *16th International Conference on Thermoelectrics*, pp. 575 -577, 1997.

[18] H. B¨ottner, “Thermoelectric micro devices: current state, recent developments and future aspects fot technological progress and applications”, *Proceedings of the 21st International Conference on Thermoelectrics*, pp. 511-518, 2002.

[19] J. Xie, C. Lee, and H. Feng, “Design, fabrication and characterization of CMOS MEMS-based thermoelectric power generators”, *Journal of Microelectromechanical Systems*, vol. 19, no. 2, pp. 317-324, 2010.

[20] The Seiko Watch Corporation, http://www.seikowatches.com.

[21] T. Kanesaka, “Development of a thermal energy watch”, *Proc. 64th Conference on Chronometry (Socit Suisse de Chronomtrie), Le Sentier, Switzerland*, pp. 19-22, 1999.

[22] N. S. Hudak, and G. G. Amatucci, “Small-scale energy harvesting through thermoelectric, vibration, and radio frequency power conversion”, *Journal of Applied Physic*s, vol. 103, no. 10, pp. 101301, 2008.

[23] J. M. Rabaey, M. J. Ammer, and J. L. da Silva, “PicoRadio supports ad hoc ultra-low power wireless networking”, *Computer*, vol. 33, no. 7, pp. 42-48, 2000.

[24] J. B. Burch, M. Clark, M. G. Yost, C. T. E. Fitzpatrick, A. M. Bachand, J. Ramaprasad, and J. S. Reif, “Radio frequency nonionizing radiation in a community exposed to radio and television broadcasting”, *Environmental Health Perspectives*, vol. 114, no. 2, pp. 248, 2006.

[25] S. Roundy, P. K. Wright, and K. S. J. Pister, "Micro-electrostatic vibration-to-electricity converters", *ASME International Mechanical Engineering Congress and Exposition*, pp. 487-496, 2002.

[26] F. Cottone, "Nonlinear Piezoelectric Generators for Vibration Energy Harvesting", *Ph.D. Thesis*, University of Perugia, Italy, 2008.

[27] N. Schenck, and J. Paradiso, "Energy scavenging with shoe-mounted piezoelectrics", *IEEE Micro*, vol. 21, no. 3, pp. 30-42, 2001.

[28] S. Roundy, D. Steingart, L. Frechette, P. Wright, and J. Rabaey, "Power sources for wireless sensor networks", *First European Workshop on Wireless Sensor Networks*, pp. 1-17, 2004.

[29] F. Moll, and A. Rubio, "An approach to the analysis of wearable body-powered systems", *Proceedings of the Mixed Design of Integrated Circuits and Systems Conference*, Gdynia, Poland, 2000.

[30] T. Starner, "Human powered wearable computing", *IBM Systems Journal*, vol. 35, no. 3-4, pp. 618-629, 1996.

[31] E. M. Yeatman, "Advances in power sources for wireless sensor nodes", *International Workshop on Wearable and Implantable Body Sensor Networks Proceedings*, Imperial College London, U.K., 2004.

[32] S. P. Beeby, M. J. Tudor, and N. M. White, "Energy harvesting vibration sources for microsystems applications", *Measurement Science and Technology*, vol. 17, no. 12, pp. 175-195, 2006.

[33] C. B. Williams, and R. B. Yates, "Analysis of a micro-electric generator for microsystems", *Sensors and Actuators A: Physics*, vol. 52, no. 1-3, pp. 8-11, 1996.

[34] P. D. Mitcheson, T. C. Green, E. M. Yeatman, and A. S. Holmes, "Architectures for vibration-driven micropower generators", *Journal of Microelectromechanical Systems*, vol. 13, no. 3, pp. 429-40, 2004.

[35] S. Roundy, and P. K. Wright, "A piezoelectric vibration based generator for wireless electronics", *Smart Material and Structures*, vol. 13, no. 4, pp. 1131-1142, 2004.

[36] S. R Anton, and H. A Sodano, "A review of power harvesting using piezoelectric materials (2003–2006)", *Smart Material and Structures*, vol. 16, no. 3, R1, 2007.

[37] P. Glynne-Jones, S. P. Beeby, and N. M. White, "Towards a piezoelectric vibration powered microgenerator", *IEE Proceedings - Science, Measurement and Technology*, vol. 148, no. 2, pp. 68-72, 2001.

[38] N. M. White, P. Glynne-Jones, and S. P. Beeby, "A novel thick-film piezoelectric micro-generator", *Smart Material and Structures*, vol. 10, no. 4,

850-852, 2001.

[39] H. A. Sodano, G. Park, and D. J. Inman, “Estimation of electric charge output for piezoelectric energy harvesting”, *Strain*, vol. 40, no. 2, pp. 49–58, 2004.

[40] S. Saadon, and O. Sidek, “A review of vibration-based MEMS piezoelectric energy harvesters”, *Energy Conversion and Management*, vol. 52, no. 1, pp. 500-504, 2011.

[41] H. B. Fang, J. Q. Liu, Z. Y. Xu, L. Dong, L. Wang, D. Chen, B. C. Cai, and Y. Liu, “Fabrication and performance of MEMS-based piezoelectric power generator for vibration energy harvesting”, *Microelectronics Journal*, vol. 37, no. 11, pp. 1280-1284, 2006.

[42] D. Shen, J. H. Park, J. Ajitsaria, S. Y. Choe, H. C. Wikle, and D. J. Kim, “The design, fabrication and evaluation of a MEMS PZT cantilever with an integrated Si proof mass for vibration energy harvesting”, *Journal of Micromechanics and Microengineering*, vol. 18, no. 5, pp. 055017, 2008.

[43] M. Renaud, K. Karakaya, T. Sterken, P. Fiorini, C. Van Hoof, and R. Puers, “Fabrication, modeling and characterization of MEMS piezoelectric vibration harvesters,” *Sensors and Actuators A: Physics*, vol. 145-146, no. 1-2, pp. 380-386, 2008.

[44] Y. B. Jeon, R. Sood, J. H. Jeong, and S. G. Kim, “MEMS power generator with transverse mode thin film PZT,” *Sensors and Actuators A: Physics*, vol. 122, no. 1, pp. 16-22, 2005.

[45] B. S. Lee, S. C. Lin, W. J. Wu, X. Y. Wang, P. Z. Chang, and C. K. Lee, “Piezoelectric MEMS generators fabricated with an aerosol deposition PZT thin film”, *Journal of Micromechanics and Microengineering*, vol. 19, no. 6, pp. 065014, 2009.

[46] J. C. Park, J. Y. Park, and Y. P. Lee, “Modeling and characterization of piezoelectric d_{33}-mode MEMS energy harvester,” *Journal of Microelectromechanial Systems*, vol. 19, no. 5, pp. 1215-1222, 2010.

[47] M. Marzencki, Y. Ammar, and S. Basrour, “Integrated power harvesting system including a MEMS generator and a power management circuit,” *Sensors and Actuators A: Physics*, vol. 145-146, no. 1-2, pp. 363-370, 2008.

[48] R. Elfrink, T. M. Kamel, M. Goedbloed, S. Matova, D. Hohlfeld, Y. van Andel, and R. van Schaijk, “Vibration energy harvesting with aluminum nitride-based piezoelectric devices,” *Journal of Micromechanics and Microengineering*, vol. 19, no. 9, pp. 094005, 2009.

[49] T.-T. Yen, T. Hirasawa, P. K. Wright, A. P. Pisano, and L. Lin, “Corrugated aluminum nitride energy harvesters for high energy conversion effectiveness,” *Journal of Micromechanics and Microengineering*, vol. 21, no. 8, pp. 085037, 2011.

[50] R. Xu, A. Lei, T. L. Christiansen, K. Hansen, M. Guizzetti, K. Birkelund, E.V. Thomsen, and O. Hansen, "Screen printed PZT/PZT thick film bimorph MEMS cantilever device for vibration energy harvesting", *Proceedings of the 16th International Solid-State Sensors, Actuators and Microsystems Conference (IEEE Transducers 2011)*, pp. 679-682, 2011.

[51] E. E. Aktakka, R. L. Peterson, and K. Najafi, "Thinned-PZT on SOI process and design optimization for piezoelectric inertial energy harvesting", *Proceedings of the 16th International Solid-State Sensors, Actuators and Microsystems Conference (IEEE Transducers 2011)*, pp. 1649-1652, 2011.

[52] C. B. Williams, C. Shearwood, M. A. Harradine, P. H. Mellor, T. S. Birch, and R. B. Yates, "Development of an electromagnetic micro-generator", *IEE Proceeding- Circuits Devices and Systems*, vol. 148, no. 6, pp. 337-342, 2001.

[53] C. Shearwood, and R. B. Yates, "Development of an electromagnetic micro-generator", *Electronics Letters*, vol. 33, no. 22, pp.1883-1884, 1997.

[54] C. Serre, A. Perez-Rodriguez, N. Fondevilla, J. R. Morante, J. Montserrat, and J. Esteve, "Vibrational energy scavenging with Si technology electromagnetic inertial microgenerators", *Microsystem Technologies*, vol. 13, no. 11-12, pp. 1655-1661, 2007.

[55] C. Serre, A. Perez-Rodriguez, N. Fondevilla, J. R. Morante, E. Martincic, S. Martinez, J. Montserrat, and J. Esteve, "Design and implementation of mechanical resonators for optimized inertial electromagnetic microgenerators", *Microsystem Technologies*, vol. 14, no. 4-5, pp. 653-658, 2008.

[56] M. El-hami, P. Glynne-Jones, E. James, S. P. Beeby, N. M. White, A. D. Brown, J. N. Ross, and M. Hill, "Design and fabrication of a new vibration-based electromechanical power generator", *Sensors and Actuators A: Physics*, vol. 92, no. 1-3, pp. 335-342, 2001.

[57] P. Glynne-Jones, M. J. Tudor, S. P. Beeby, and N. M. White, "An electromagnetic, vibration-powered generator for intelligent sensor systems", *Sensors and Actuators A: Physics*, vol. 110, no. 1-3, pp. 344-349, 2004.

[58] S. P. Beeby, R. N. Torah, M. J. Tudor, P. Glynne-Jones, T. O'Donnell, C. R. Saha, and S. Roy, "A micro electromagnetic generator for vibration energy harvesting", *Journal of Micromechanics and Microengineering*, vol. 17, no. 7, pp. 1257-1265, 2007.

[59] S. Kulkarni, E. Koukharenko, R. Torah, J. Tudor, S. Beeby, T. O'Donnell, and S. Roy, "Design, fabrication and test of integrated micro-scale vibration-based electromagnetic generator", *Sensors and Actuators A: Physics*, vol. 145-146, no. 1-2, pp. 336-342, 2008.

[60] N. N. H. Ching, H. Y. Wong, W. J. Li, P. H. W. Leong, and Z. Wen, "A laser-micromachined multi-modal resonating power transducer for wireless sensing systems", *Sensors and Actuators A: Physics*, vol. 97, pp. 685-690, 2002.

[61] J. M. H. Lee, S. C. L. Yuen, W. J. Li, and P. H. W. Leong, “Development of an AA size energy transducer with micro resonators”, *Proceedings of IEEE International Symposium on Circuits and Systems*, vol. 4, pp. IV876–IV879, 2003.

[62] N. Wang, and D. P. Arnold, “Fully batch-fabricated MEMS magnetic vibration energy harvesters”, *Proceedings of PowerMEMS 2009*, pp. 348-351, 2009.

[63] Y. Jiang, S. Masaoka, T. Fujita, M. Uehara, T. Toyonaga, K. Fujii, K. Higuchi, and K. Maenaka, “Fabrication of a vibration-driven electromagnetic energy harvester with integrated NdFeB/Ta multilayered micro-magnets”, *Journal of Micromechanics and Microengineering*, vol. 21, no. 9, pp. 095014, 2011.

[64] C. Cepnik, and U. Wallrabe, “A flat high performance micro energy harvester based on a serpentine coil with a single winding”, *Proceedings of the 16th International Solid-State Sensors, Actuators and Microsystems Conference (IEEE Transducers 2011)*, pp. 661-664, 2011.

[65] H. Kloub, D. Hoffmann, B. Folkmer, and Y. Manoli, “A micro capacitive vibration energy harvester for low power electronics”, *Proceedings of PowerMEMS 2009*, pp. 165-168, 2009.

[66] D. Hoffmann, B. Folkmer, and Y. Manoli, “Fabrication, characterization and modelling of electrostatic micro-generators”, *Journal of Micromechanics and Microengineering*, vol. 19, no. 9, pp. 094001, 2009.

[67] D. Hoffmann, B. Folkmer, and Y. Manoli, “Analysis and characterization of triangular electrode structures for electrostatic energy harvesting”, *Journal of Micromechanics and Microengineering*, vol. 21, no. 10, pp. 104002, 2011.

[68] Y. Chiu, and V. F. G. Tseng, “A capacitive vibration-to-electricity energy converter with integrated mechanical switches”, *Journal of Micromechanics and Microengineering*, vol. 18, no. 10, pp. 104004, 2008.

[69] M. Miyazaki, H. Tanaka, G. Ono, T. Nagano, N. Ohkubo, T. Kawahara, and K. Yano, “Electric-energy generation using variable-capacitive resonator for power-free LSI: efficiency analysis and fundamental experiment”, *ISLPED ’03*, pp. 193-198, 2003.

[70] J. Boland, Y. H. Chao, Y. Suzuki, and Y. C. Tai, “Micro electret power generator”, *IEEE International Conference on Micro Electro Mechanical Systems (MEMS 2003)*, pp. 538-541, 2003.

[71] T. Tsutsumino, Y. Suzuki, N. Kasagi1, and Y. Sakane, “Seismic power generator using high-performance polymer electret”, *IEEE International Conference on Micro Electro Mechanical Systems (MEMS 2006)*, pp. 98-101, 2006.

[72] Y. Sakane, Y. Suzuki, and N. Kasagi, “The development of a high-performance perfluorinated polymer electret and its application to micro

power generation", *Journal of Micromechanics and Microengineering*, vol. 18, no. 10, pp. 104011, 2008.

[73] D. Miki, M. Honzumi, Y. Suzuki, and N. Kasagi, "Large-amplitude MEMS electret generator with nonlinear spring", *Proceedings of the 23rd IEEE International Conference on Micro Electro Mechanical Systems (MEMS 2010)*, pp. 176-179, 2010.

[74] Y. Suzuki, D. Miki, M. Edamoto, and M. Honzumi, "A MEMS electret generator with electrostatic levitation for vibration-driven energy-harvesting applications", *Journal of Micromechanics and Microengineering*, vol. 20, no. 10, pp. 104002, 2010.

[75] T. Masaki, K. Sakurai, T. Yokoyama, M. Ikuta, H. Sameshima, M. Doi, T. Seki, and M. Oba, "Power output enhancement of a vibration-driven electret generator for wireless sensor applications", *Journal of Micromechanics and Microengineering*, vol. 21, no. 10, pp. 104004, 2011.

[76] E. Halvorsen, E. R. Westby, S. Husa, A. Vogl, N. P. Østbø, V. Leonov, T. Sterken, and T. Kvisterøy, "An electrostatic energy harvester with electret bias", *Proceedings of the 15th International Conference on Solid-State Sensors, Actuators and Microsystems (IEEE Transducer 09)*, pp. 1381-1384, 2009.

[77] Z. Yang, J. Wang, and J. Zhang, "A high-performance micro electret power generator based on microball bearings", *Journal of Micromechanics and Microengineering*, vol. 21, no. 6, pp. 065001, 2011.

[78] Y. Naruse, N. Matsubara, K. Mabuchi, M. Izumi, and S. Suzuki, "Electrostatic micro power generation from low-frequency vibration such as human motion", *Journal of Micromechanics and Microengineering*, vol. 19, no. 9, pp. 094002, 2009.

[79] P. Basset, D. Galayko, A. Mahmood Paracha, F. Marty, A. Dudka, and T. Bourouina, "A batch-fabricated and electret-free silicon electrostatic vibration energy harvester", *Journal of Micromechanics and Microengineering*, vol. 19, no. 11, pp. 115025, 2009.

[80] H. Lo and Y. Tai, "Parylene-based electret power generators", *Journal of Micromechanics and Microengineering*, vol. 18, no. 10, pp. 104006, 2008.

[81] T. von Buren, P. Lukowicz, and G. Troster, "Kinetic energy powered computing - An experimental feasibility study," *Proceedings of the 7th IEEE International Symposium on Wearable Computers (ISWC 2003)*, pp. 22-24, 2003.

[82] D. Paci, M. Schipani, V. Bottarel, and D. Miatton, "Optimization of a piezoelectric energy harvester for environmental broadband vibrations," *Proceedings of the 15th IEEE International Conference on Electronics, Circuits and Systems (ICECS 2008)*, pp. 177-181, 2008.

[83] S. Roundy, P. K. Wright, and J. Rabaey, “A study of low level vibrations as a power source for wireless sensor nodes”, *Computer Communications*, vol. 26, no. 11, pp. 1131-1144, 2003.

[84] S. Roundy, “On the Effectiveness of Vibration Based Energy Scavenging”, *Journal of Intelligent Material Systems and Structures*, vol. 16, no. 10, pp. 809-823, 2005.

[85] E. Reilly, L. Miller, R. Fain, and P. K. Wright, “A study of ambient vibrations for piezoelectric energy conversion,” *Proceedings of PowerMEMS 2009*, pp. 312-315, 2009.

[86] L. M. Miller, E. Halvorsen, T. Dong, and P. K. Wright, “Modeling and experimental verification of low-frequency MEMS energy harvesting from ambient vibrations”, *Journal of Micromechanics and Microengineering*, vol. 21, no. 4, pp. 045029, 2011.

[87] D. Zhu, M. J. Tudor, and S. P. Beeby, “Strategies for increasing the operating frequency range of vibration energy harvesters: a review”, *Measurement Science and Technology*, vol. 21, no. 2, pp. 022001, 2010.

[88] J. F. Gieras, J. H. Oh, M. Huzmezan, and H. S. Sane, “Electromechanical energy harvesting system”, *Patent Publication Number*: WO2007070022(A2), WO2007070022(A3), 2007.

[89] X. Wu, J. Lin, S. Kato, K. Zhang, T. Ren, and L. Liu, “A frequency adjustable vibration energy harvester,” Proceedings of *PowerMEMS 2008 + microEMS 2008*, pp. 245-248, 2008.

[90] V. R. Challa, M. G. Prasad, Y. Shi, and F. T. Fisher, “A vibration energy harvesting device with bidirectional resonance frequency tunability,” *Smart Material and Structures*, vol. 17, no. 1, pp. 015035, 2008.

[91] E. S. Leland, and P. K. Wright, “Resonance tuning of piezoelectric vibration energy scavenging generators using compressive axial preload,” *Smart Material and Structures*, vol. 15, no. 5, pp. 1413-1420, 2006.

[92] C. Eichhorn, F. Goldschmidtboeing and P. Woias, “A frequency piezoelectric energy convert based on a cantilever beam”, *Proceedings of PowerMEMS 2008+ microEMS2008*, pp. 309-312, 2008.

[93] W-J Wu, Y-Y Chen, B-S Lee, J-J He, and Y-T Peng, “Tunable resonant frequency power harvesting devices”, *Proceedings of SPIE*, vol. 6169, pp. 55-62, 2006.

[94] D. Charnegie, “Frequency tuning concepts for piezoelectric cantilever beams and plates for energy harvesting”, *MSc Dissertation*, University of Pittsburgh, USA, 2007.

[95] S. M. Shahruz, “Design of mechanical band-pass filters for energy scavenging”, *Journal of Sound and Vibration*, vol. 292, no. 3-5, pp. 987-998,

2006.

[96] H. Xue, Y. Hu, and Q-M Wang, “Broadband piezoelectric energy harvesting devices using multiple bimorphs with different operating frequencies”, *IEEE Transactions on Ultrasonics, Ferroelectrics, and Frequency Control*, vol. 55, no. 9, pp. 2104-2108, 2008.

[97] G-H Feng, and J-C Hung, “Optimal FOM designed piezoelectric microgenerator with energy harvesting in a wide vibration bandwidth”, *Proceedings of the 2nd IEEE International Conference on Nano/Micro Engineered and Molecular Systems (IEEE NEMS 2007)*, pp. 511-514, 2007.

[98] M. Ferrari, V. Ferrari, M. Guizzetti, D. Marioli, and A. Taroni, “Piezoelectric multifrequency energy converter for power harvesting in autonomous microsystems”, *Sensors and Actuators, A: Physical*, vol. 142, no. 1, pp. 329-335, 2008.

[99] I. Sari, T. Balkan, and H. Kulah, “An electromagnetic micro power generator for wideband environmental vibrations”, *Sensors and Actuators, A: Physical*, vol. 145-146, no. 1-2, pp. 405-413, 2008.

[100] I. Sari, T. Balkan, and H. Kulah, “An electromagnetic micro energy harvester based on an array of parylene cantilevers”, *Journal of Micromechanics and Microengineering*, vol. 19, no. 10, pp. 105032, 2009.

[101] M. S. M. Soliman, E. M. Abdel-Rahman, E. F. El-Saadany, and R. R. Mansour, “A wideband vibration-based energy harvester”, *Journal of Micromechanics and Microengineering*, vol. 18, no. 11, pp. 115021, 2008.

[102] M. S. M. Soliman, E. M. Abdel-Rahman, E. F. El-Saadany, and R. R. Mansour, “A design procedure for wideband micropower generators”, *Journal of Microelectromechanical Systems*, vol. 18, no. 6, pp. 1288-1299, 2009.

[103] S. Moss, A. Barry, I. Powlesland, S. Galea, and G. P. Carman, “A low profile vibro-impacting energy harvester with symmetrical stops”, *Applied Physics Letters*, vol. 97, no. 23, pp. 234101, 2010.

[104] D. Spreemann, B. Folkmer, D. Maurath, and Y. Manoli, “Tunable transducer for low frequency vibrational energy scavenging”, *Proceedings of EurosensorsXX*, 2006.

[105] B. P. Mann, and N. D. Sims, “Energy harvesting from the nonlinear oscillations of magnetic levitation”, *Journal of Sound and Vibration*, vol. 319, no. 1-2, pp. 515-530, 2009.

[106] S. G. Burrow, and L. R. Clare, “A resonant generator with non-linear compliance for energy harvesting in high vibrational environments”, *Proceedings of IEEE International Electric Machines and Drives Conference, (IEMDC 2007)*, vol. 1, pp. 715-720, 2007.

[107] S G Burrow, L R Clare, A Carrella, and D Barton, “Vibration energy

harvesters with non-linear compliance", *Proceedings of SPIE*, vol. 6928, pp. 692807, 2008.

[108] A. Erturk, J. Hoffmann, and D. J. Inman, "A piezomagnetoelastic structure for broadband vibration energy harvesting", *Applied Physics Letters*, vol. 94, no. 25, pp. 254102, 2009.

[109] X. Xing, J. Lou, G. M. Yang, O. Obi, C. Driscoll, and N. X. Sun, "Wideband vibration energy harvester with high permeability magnetic material", *Applied Physics Letters*, vol. 95, no. 13, pp. 134103, 2009.

[110] J. Yang, Y. Wen, P. Li, and X. Dai, "A magnetoelectric, broadband vibration-powered generator for intelligent sensor systems", *Sensors and Actuators: A Physical*, vol. 168, no. 2, pp. 358-364, 2011.

[111] G. Sebald, H. Kuwano, D. Guyomar, and B. Ducharnel, "Experimental Duffing oscillator for broadband piezoelectric energy harvesting", *Smart Material and Structures*, vol. 20, no. 10, pp. 102001, 2011.

[112] F. Cottone, H. Vocca, and L. Gammaitoni, "Nonlinear energy harvesting", *Physical Review Letters*, vol. 102, no. 8, pp. 080601, 2009.

[113] B. And`o, S. Baglio, C. Trigona, N. Dumas, L. Latorre, and P. Nouet, "Nonlinear mechanism in MEMS devices for energy harvesting applications", *Journal of Micromechanics and Microengineering*, vol. 20, no. 12, pp. 125020, 2010.

[114] M. Ferrari, M. Baù, M. Guizzetti, and V. Ferrari, "A single-magnet nonlinear piezoelectric converter for enhanced energy harvesting from random vibrations", *Sensors and Actuators: A Physical*, vol. 172, no. 1, pp. 287-292, 2011.

[115] S. C. Stanton, C. C. McGehee, and B. P. Mann, "Reversible hysteresis for broadband magnetopiezoelastic energy harvesting", *Applied Physics Letters*, vol. 95, no. 17, pp. 174103, 2009.

[116] L. G. W. Tvedt, D. S. Nguyen, and E. Halvorsen, "Nonlinear behavior of an electrostatic energy harvester under wide- and narrowband excitation", *Journal of Microelectromechanical Systems*, vol. 19, no. 2, pp. 305-316, 2010.

[117] D. S. Nguyen, E. Halvorsen, G. U. Jensen, and A. Vogl, "Fabrication and characterization of a wideband MEMS energy harvester utilizing nonlinear springs", *Journal of Micromechanics and Microengineering*, vol. 20, no. 12, pp. 125009, 2010.

[118] D. S. Nguyen, and E. Halvorsen, "Nonlinear springs for bandwidth-tolerant vibration energy harvesting", *Journal of Microelectromechanical Systems*, vol. 20, no. 6, pp. 1225-1227, 2011.

[119] A. Hajati, and S-G Kim, "Ultra-wide bandwidth piezoelectric energy harvesting", *Applied Physics Letters*, vol. 99, no. 8, pp. 083105, 2011.

[120] B. Yang, and C. Lee, “Non-resonant electromagnetic wideband energy harvesting mechanism for low frequency vibrations”, *Microsystem Technologies*, vol. 16, no. 6, pp. 961-966, 2010.

[121] M. Umeda, K. Nakamura, and S. Ueha, “Analysis of transformation of mechanical impact energy to electrical energy using a piezoelectric vibrator”, *Japanese Journal of Applied Physics*, vol. 35, no. 5B, pp. 3267-3273, 1996.

[122] M. Umeda, K. Nakamura, and S. Ueha, “Energy storage characteristics of a piezo-generator using impact induced vibration”, *Japanese Journal of Applied Physics*, vol. 36, no. 5B, pp. 3146-3151, 1997.

[123] M. Renaud, P. Fiorini, R. van Schaijk, and C. van Hoof, “Harvesting energy from the motion of human limbs: the design and analysis of an impact-based piezoelectric generator”, *Smart Materials and Structures*, vol. 18, no. 3, pp. 035001, 2009.

[124] G. Manla, N. M. White, and J. Tudor, “Harvesting energy from vehicle wheels”, *Proceedings of the 15th International Conference on Solid-State Sensors, Actuators and Microsystems (IEEE Transducer 09)*, pp. 1389-1392, 2009.

[125] L. Gu, and C. Livermore, “Impact-driven, frequency up-converting coupled vibration energy harvesting device for low frequency operation”, *Smart Materials and Structures*, vol. 20, no. 4, pp. 045004, 2011.

[126] L. Gu, “Low-frequency piezoelectric energy harvesting prototype suitable for the MEMS implementation”, *Microelectronics Journal*, vol. 42, no. 2, pp. 277-282, 2011.

[127] D-G Lee, G-P Carman, D. Murphy, and C. Schulenburg, “Novel micro vibration energy harvesting device using frequency up conversion”, *Proceedings of the 14th International Conference on Solid-State Sensors, Actuators and Microsystems (IEEE Transducer 07)*, pp. 871-874, 2007.

[128] O. Zorlu, E. T. Topal, and H. Kulah, “A vibration-based electromagnetic energy harvester using mechanical frequency up-conversion method”, *IEEE Sensors Journal*, vol. 11, no. 2, pp. 481-488, 2011.

[129] S-M Jung, and K-S Yun, “A wideband energy harvesting device using snap-through buckling for mechanical frequency-up conversion”, *Proceedings of the 23rd IEEE International Conference on Micro Electro Mechanical Systems (MEMS 2010)*, pp. 1207-1210, 2010.

[130] S-M Jung, and K-S Yun, “Energy-harvesting device with mechanical frequency-up conversion mechanism for increased power efficiency and wideband operation”, *Applied Physics Letters*, vol. 96, no. 11, pp. 111906, 2010.

[131] H. Kulah, and K. Najafi, “Energy scavenging from low-frequency vibrations by using frequency up-conversion for wireless sensors applications”, *IEEE*

Sensors Journal, vol. 8, no. 3, pp. 261-268, 2008.

[132] I. Sari, T. Balkan, and H. Kulah, "An electromagnetic micro power generator for low-frequency environmental vibrations based on the frequency up-conversion technique", *Journal of Microelectromechanical Systems*, vol. 19, no. 1, pp. 14-27, 2010.

[133] T. Galchev, H. Kim, and K. Najafi, "Non-resonant bi-stable frequency-increased power scavenger from low-frequency ambient vibration", *Proceedings of the 15th International Conference on Solid-State Sensors, Actuators and Microsystems (IEEE Transducer 09)*, pp. 632-635, 2009.

[134] T. Galchev, E. E. Aktakka, H. Kim, and K. Najafi, "A piezoelectric frequency-increased power generator for scavenging low-frequency ambient vibration", *Proceedings of the 23rd IEEE International Conference on Micro Electro Mechanical Systems (MEMS 2010)*, pp. 1203-1206, 2010.

[135] T. Galchev, H. Kim, and K. Najafi, "Micro power generator for harvesting low-frequency and nonperiodic vibrations", *Journal of Microelectromechanical Systems*, vol. 20, no. 4, pp. 852-866, 2011.

[136] Q. Tang, Y Yang, and X. Li, "Bi-stable frequency up-conversion piezoelectric energy harvester driven by non-contact magnetic repulsion", *Smart Materials and Structures*, vol. 20, no. 12, pp. 125011, 2011.

[137] Y. Yang, Q. Tang, and X. Li, "Non-contact repulsive-force excitation for highly endurable wide frequency-range energy-harvesting", *Proceedings of the 16th International Conference on Solid-State Sensors, Actuators and Microsystems (IEEE Transducer 2011)*, pp. 687-690, 2011.

[138] D. F. Berdy, B. Jung, J. F. Rhoads, and D. Peroulis, "Increased-bandwidth, meandering vibration energy harvester", *Proceedings of the 16th International Conference on Solid-State Sensors, Actuators and Microsystems (IEEE Transducer 2011)*, pp. 2638-2641, 2011.

[139] I-H Kim, H-J Jung, B. M. Lee, and S-J Jang, "Broadband energy-harvesting using a two degree-of-freedom vibrating body", *Applied Physics Letters*, vol. 98, no. 21, pp. 214102, 2011.

[140] B. Yang, C. Lee, W. Xiang, J. Xie, J. H. He, R. K. Kotlanka, S. P. Low, and H. Feng, "Electromagnetic energy harvesting from vibrations of multiple frequencies", *Journal of Micromechanics and Microengineering*, vol. 19, no. 3, pp. 035001, 2009.

[141] B. Yang, J. Liu, G. Tang, J. Luo, C. Yang, and Y. Li, "A generator with nonlinear spring oscillator to provide vibrations of multi-frequency", *Applied Physics Letters*, vol. 99, no. 22, pp. 223505, 2011.

[142] Z. Chew, and L. Li, "Design and characterisation of a piezoelectric scavenging device with multiple resonant frequencies", *Sensors and Actuators, A: Physical*, vol. 162, no. 1, pp. 82-92, 2010.

[143] B. Yang, C. Lee, R. K. Kotlanka, J. Xie, and S. P. Lim, "A MEMS rotary comb mechanism for harvesting the kinetic energy of planar vibrations", *Journal of Micromechanics and Microengineering*, vol. 20, no. 6, pp. 065017, 2010.

[144] Y. Zhu, S. O. R. Moheimani, and M. R. Yuce, "A 2-DOF MEMS ultrasonic energy harvester", *IEEE Sensors Journal*, vol. 11, no. 1, pp. 155-161, 2011.

[145] U. Bartsch, J. Gaspar, and O. Paul, "A 2D electret-based resonant micro energy harvester", *Proceedings of IEEE 22nd International Conference on Micro Electro Mechanical Systems, (IEEE MEMS 2009)*, pp. 1043-1046, 2009.

[146] U. Bartsch, J. Gaspar, and O. Paul, "Low-frequency two-dimensional resonators for vibrational micro energy harvesting", *Journal of Micromechanics and Microengineering*, vol. 20, no. 3, pp. 035016, 2010.

[147] C. Lee, S. Kawano, T. Itoh, and T. Suga, "Characteristics of sol-gel derived PZT thin films with lead oxide cover layers and lead titanate interlayers", *Journal of Material Science*, vol. 31, no. 17, pp. 4559-4568, 1996.

[148] C. Lee, T. Itoh, R. Maeda, and T. Suga, "Characterization of micromachined piezoelectric PZT force sensors for dynamic scanning force microscopy", *Review of Scientific Instruments*, vol. 68, no. 5, pp. 2091-2100, 1997.

[149] T. Kobayashi, and R. Maeda, "Smart optical microscanner with piezoelectric resonator, sensor, and tuner using $Pb(Zr,Ti)O_3$ thin film", *Applied Physics Letters*, vol. 90, no. 18, pp. 183514, 2007.

[150] M. Zhu, E. Worthington, and J. Njuguna, "Analyses of power output of piezoelectric energy-harvesting devices directly connected to a load resistor using a coupled piezoelectric-circuit finite element method," *IEEE Transactions on Ultrasonics, Ferroelectrics and Frequency Control*, vol. 56, no. 7, pp. 1309-1318, 2009.

[151] F. P. Beer, and E. R. Johnston, Mechanics of Materials, *McGraw-Hill Inc.* 1992.

[152] A. Narimani, M. F. Golnaraghi, and G. N. Jazar, "Frequency response of a piecewise linear vibration isolator", *Journal of Vibration and Control*, vol. 10, no. 12, pp. 1775-1794, 2004.

[153] A. Hopcroft Matthew, D. Nix William, and W. Kenny Thomas, "What is the Young's Modulus of Silicon?" *Journal of Microelectromechanical Systems*, vol. 19, no. 2, pp. 229-382, 2010.

[154] T. Zhang, C. Jiang, H. Xu, and J. Mao, "Permanent-magnet longitudinal fields for magnetostrictive devices", *Journal of Applied Physics*, vol. 101, no. 3, pp. 034511, 2007.

[155] X. Wang, J. Song, J. Liu, and Z. L. Wang, "Direct-current nanogenerator driven by ultrasonic waves", *Science*, vol. 316, no. 5821, pp. 102-105, 2007.

[156] G. Zhu, R. Yang, S. Wang, and Z. L. Wang, “Flexible high-output nanogenerator based on lateral ZnO nanowire array”, *Nano Letters*, vol. 10, no. 8, pp. 3151-3155, 2010.

Appendices

Appendix A: Frequency Response of A Wideband Energy Harvester with Stoppers on Two Sides

The dimensionless equation of the mass motion of an impact-based energy harvester system with stoppers on two sides is given by

$$\ddot{u} + 2\xi_0\dot{u} + u = \rho^2 \sin(\rho\tau) + f(u,\dot{u}) \tag{A.1}$$

where

$$f(u,\dot{u}) = \begin{cases} -2\rho_1\xi_1\dot{u} - \rho_1^2 u + \rho_1^2\delta_1 & (u \geq \delta_1) \\ 0 & (-\delta_2 < u < \delta_1) \\ -2\rho_2\xi_2\dot{u} - \rho_2^2 u - \rho_2^2\delta_2 & (u \leq -\delta_2) \end{cases} \tag{A.2}$$

The first-order approximate solution of (A.1) is assumed to be

$$u = a(\tau)\sin(\varphi(\tau)) \tag{A.3}$$

$$\dot{u} = a(\tau)\rho\cos(\varphi(\tau)) \tag{A.4}$$

$$\varphi(\tau) = \rho\tau + \beta(\tau) \tag{A.5}$$

where $a(\tau)$ is a slowly varying amplitude, and $\beta(\tau)$ is a slowly varying phase difference between the base excitation and the response. Eqs. (A.3) and (A.4) imply that

$$\dot{a}\sin\varphi + a\dot{\beta}\cos\varphi = 0 \tag{A.6}$$

Substituting Eqs. (A.3) and (A.4) into Eq. (A.1) yields

$$\begin{aligned}\dot{a}\rho\cos\varphi - a\dot{\beta}\rho\sin\varphi &= a(\rho^2-1)\sin\varphi \\ &+ \rho^2\sin(\varphi-\beta) - 2\xi_0 a\rho\cos\varphi + f(u,\dot{u})\end{aligned} \tag{A.7}$$

Solving Eqs. (A.6) and (A.7) for $\dot{a}$ and $\dot{\beta}$, we have

$$\begin{aligned}\dot{a}\rho = &[a(\rho^2-1)+\rho^2\cos\beta]\sin\varphi\cos\varphi \\ &-(2\xi_0 a\rho+\rho^2\sin\beta)\cos^2\varphi + f(u,\dot{u})\cos\varphi\end{aligned} \tag{A.8}$$

$$\begin{aligned}a\dot{\beta}\rho = &-[a(\rho^2-1)+\rho^2\cos\beta]\sin^2\varphi \\ &+(2\xi_0 a\rho+\rho^2\sin\beta)\cos\varphi\sin\varphi - f(u,\dot{u})\sin\varphi\end{aligned} \tag{A.9}$$

Since the variables $\dot{a}$ and $\dot{\beta}$ vary slowly, we may suppose that their average values remain constant over a cycle period of 2π:

$$\begin{aligned}2\pi\dot{a}\rho = &\int_0^{2\pi}[(a(\rho^2-1)+\rho^2\cos\beta)\sin\varphi\cos\varphi - (2\xi_0 a\rho+\rho^2\sin\beta)\cos^2\varphi]d\varphi \\ &+\int_0^{2\pi} f(u,\dot{u})\cos\varphi d\varphi\end{aligned} \tag{A.10}$$

$$\begin{aligned}2\pi a\dot{\beta}\rho = &\int_0^{2\pi}[-(a(\rho^2-1)+\rho^2\cos\beta)\sin^2\varphi + (2\xi_0 a\rho+\rho^2\sin\beta)\cos\varphi\sin\varphi]d\varphi \\ &+\int_0^{2\pi} f(u,\dot{u})\sin\varphi d\varphi\end{aligned} \tag{A.11}$$

where

$$f(u,\dot{u}) = \begin{cases} -2\rho_1\xi_1 a\rho\cos\varphi - \rho_1^2 a\sin\varphi + \rho_1^2\delta_1 & (\varphi_1 < \varphi < \varphi - \varphi_1) \\ -2\rho_2\xi_2 a\rho\cos\varphi - \rho_2^2 a\sin\varphi - \rho_2^2\delta_2 & (\pi+\varphi_2 < \varphi < 2\pi - \varphi_2) \end{cases} \tag{A.12}$$

$\varphi_1 = \sin^{-1}(\delta_1/a)$ and $\varphi_2 = \sin^{-1}(\delta_2/a)$ are the phase values of when the proof mass engages the top-stopper and bottom-stopper, respectively.

For the steady-state response solution of the system, the time derivatives on the left-hand side of Eqs. (A.10) and (A.11) are considered to be zero. Hence integration of Eqs. (A.10) and (A.11) gives

$$\pi\rho^2 \sin\beta = -2\xi_0 a\rho\pi - \rho_1\xi_1 a\rho(\pi - 2\varphi_1 - \sin 2\varphi_1) - \rho_2\xi_2 a\rho(\pi - 2\varphi_2 - \sin 2\varphi_2) \tag{A.13}$$

$$\pi\rho^2 \cos\beta = \pi a(1-\rho^2) - [\frac{1}{2}\rho_1^2 a(2\varphi_1 - \sin 2\varphi_1 - \pi) + \frac{1}{2}\rho_2^2 a(2\varphi_2 - \sin 2\varphi_2 - \pi) + 2\rho_1^2\delta_1\cos\varphi_1 + 2\rho_2^2\delta_2\cos\varphi_2] \tag{A.14}$$

Combining Eqs. (A.13) and (A.14), the implicit equation for the amplitude a as a function of the excitation frequency ρ is given by

$$\pi^2\rho^4 = X_1^2 + X_2^2 \tag{A.15}$$

where X_1 and X_2 are in the right-hand side of Eqs. (A.13) and (A.14), respectively. Based on the frequency-response function (A.15), the dimensionless amplitude a with respect to frequency ρ can be obtained accordingly.

Appendix B: Series and Parallel Connections of PZT Elements

As shown in Fig. 3.3, on the supporting beams of PEH-L and PEH-H, ten parallel-arrayed PZT elements are patterned on top of each beam and they are series assigned Arabic numbers from 1 to 10. The PZT elements are electrically isolated from one another for ease of connection in series or in parallel in the measurement.

B.1 Voltage outputs for PZT elements connected in series and in parallel

In order to study the output performance of PZT elements connected in series and in parallel, load rms voltage measurement of configuration I (PEH-L with metal package)

is conducted by using vibration testing system in Fig. 3.11. The input impedance 1 MΩ of DSA is served as the load resistance in the testing and following discussion.

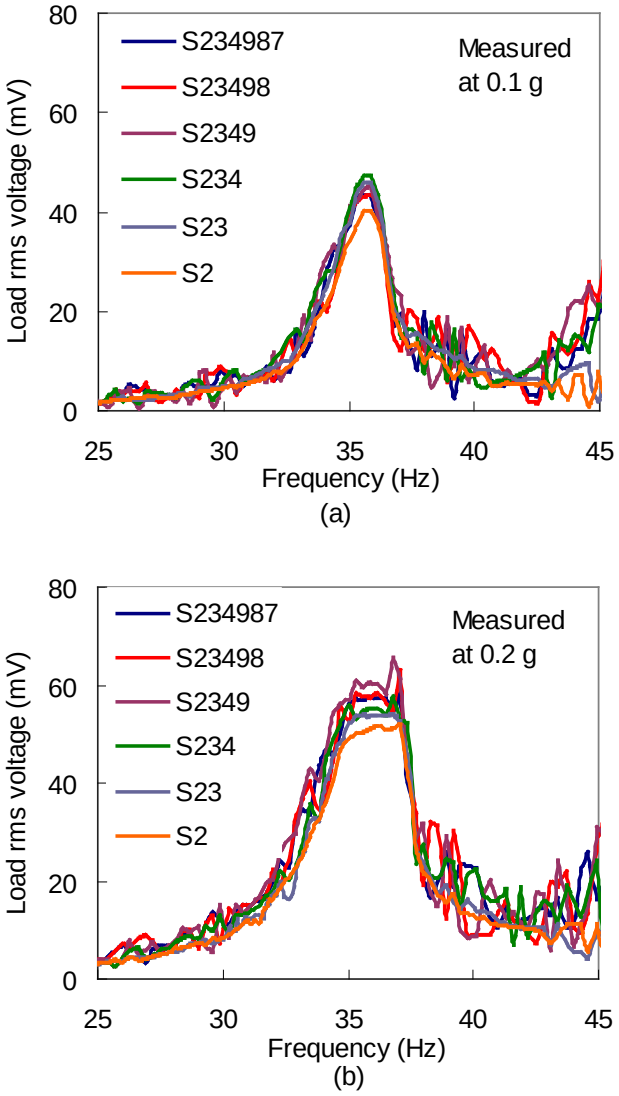

Figure B.1 Load rms voltages against frequencies for gradually increasing numbers of PZT elements connected in series at accelerations of (a) 0.1 g and (b) 0.2 g.

Figures B.1 (a) and (b) show the load rms voltages against frequencies for gradually increasing numbers of PZT elements connected in series at accelerations of 0.1 g and 0.2 g, respectively. Likewise, Figs. B.2 (a) and (b) show the load rms voltages against frequencies for varying numbers of PZT elements connected in parallel at accelerations of 0.1 g and 0.2 g. For example, “S234987” indicates PZT

elements of No. 2, 3, 4, 9, 8 and 7 connected in series and “P234987” means PZT elements of No. 2, 3, 4, 9, 8 and 7 connected in parallel. It is found that the load rms voltages for series connection overlap with each other and are not affected by the connected numbers of PZT elements. However, for parallel connection, as the numbers of PZT elements gradually increasing from 1 to 6, the load rms voltages increase. As seen in Fig. B.2, the maximum voltage peaks of 94 and 119 mV occur at the resonant frequency of 36 Hz with input accelerations of 0.1 g and 0.2 g, respectively.

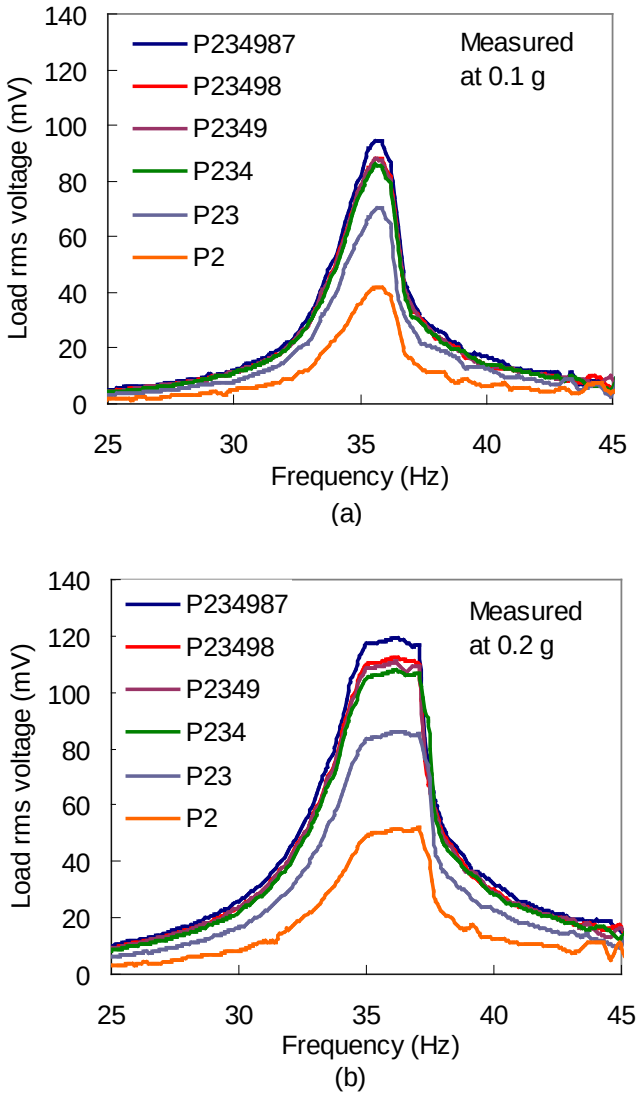

Figure B.2 Load rms voltages against frequencies for gradually increasing numbers of PZT elements connected in parallel at accelerations of (a) 0.1 g and (b) 0.2 g.

From Figs. B.1 and B.2, the voltage peaks at resonant frequency of 36 Hz for different numbers of PZT elements connected in series and in parallel are extracted and shown in Fig. B.3 (a), where the trend difference can be seen more clearly. For series connection, the load rms voltage keeps relatively constant regarding to the gradually increasing numbers of PZT elements. However, for parallel connection, the load rms voltage raises with the increment of connected PZT elements. The raising rate of the load rms voltage decreases until relatively constant with the increment of PZT elements.

Such voltage trends for series and parallel connections are due to the large PZT impedance. It is known that, for n voltage sources connected in series, the resultant voltage is n times larger than single voltage source. However, the resultant impedance is also n times larger than the impedance of single voltage source (here refers to PZT element). Therefore, the load voltage delivered to the external impedance which is smaller than the impedance of single PZT element does not change much. For n voltage sources connected in parallel, the resultant voltage is the same as single voltage source. Meanwhile, the resultant impedance is 1/n times smaller than the impedance of single PZT element. Therefore, initially the load voltage delivered to the external impedance will increase greatly, but gradually keep constant as increasing numbers of voltage sources connected. Such trends can be explained and verified by using simulation software SPICE as shown in Fig. B.3 (b). In the simulation, the source voltage *Vs* of each PZT element is derived from the measured load rms voltage V_L in Fig. 3.14 (b) by using equivalent circuit as shown in Fig. 3.12. It is found that the simulation results match quite well with the experimental results. The minor difference is because the fluctuation of the impedance of each PZT element was not considered in the simulation.

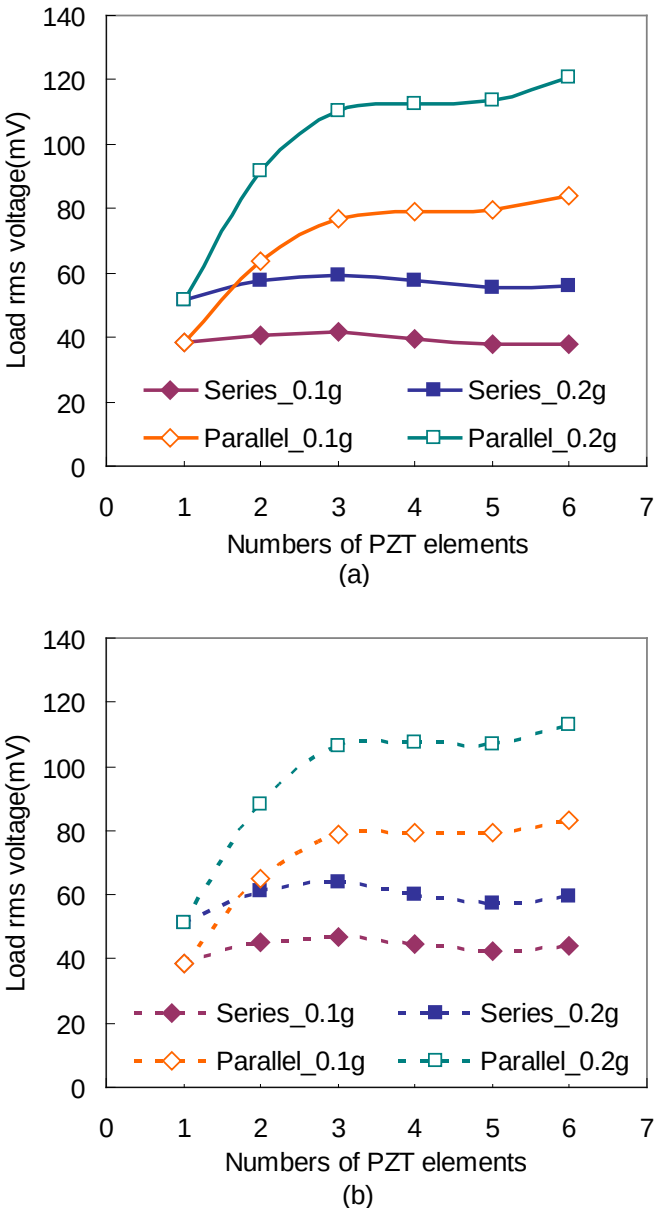

Figure B.3 (a) Experimental and (b) simulation results of voltage peaks at resonant frequency for different numbers of PZT elements connected in series and in parallel.

B.2 Power outputs for PZT elements connected in series and in parallel

In Figs. B.4 and B.5, the load rms voltages and corresponding power outputs are presented regarding to varying resistances by experimental and simulation methods. In the experiment, load resistors in parallel with DSA are connected with six PZT elements in series and in parallel connections. Thus the load rms voltage measured by

the DSA is referring to the resultant resistance of the external resistors and internal impedance of the DSA connected in parallel.

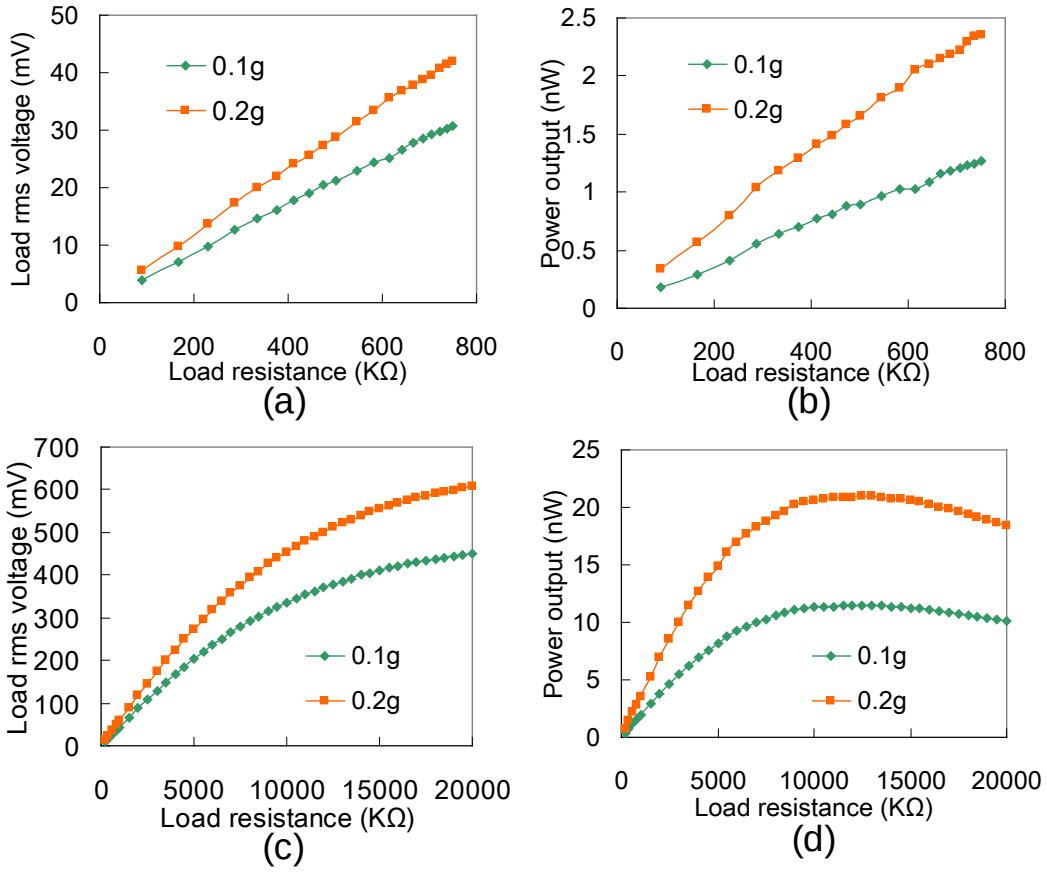

Figure B.4 Experimental results of (a) load rms voltages and (b) power outputs against load resistances for six PZT elements in series connection; Simulation results of (c) load rms voltages and (d) power outputs against load resistances for six PZT elements in series connection.

Figure B.4 (a) and (b) show the experimental results of load rms voltages and power outputs against load resistances for six PZT elements connected in series at accelerations of 0.1 g and 0.2 g. It is seen that the load rms voltages and power outputs increase monotonically. Be noted that the load resistance range is within 800 kΩ, because the impedance of DSA is 1 MΩ, the resultant load resistance will always be smaller than 1 MΩ, no matter how large the external resistors of the circuit connected with. It is also known that the maximum power output occurs when the

load impedance matches with the resultant internal impedance of the PZT elements in the circuit. For six PZT elements connected in series, the resultant impedance is too large that beyond the measurement range. Therefore, in Fig. B.4 (b), it is only seen a gradually growing power output without appearing a maximum power peak. To complete and present the whole curve, simulation results by SPICE are shown in Figs. B.4 (c) and (d). It is seen that the load rms voltages tend towards constant values after monotonically increasing. The power outputs reach the maximum values of 11.4 and 20.9 nW with the matched load resistance of 12.5 MΩ at 0.1 g and 0.2 g, respectively.

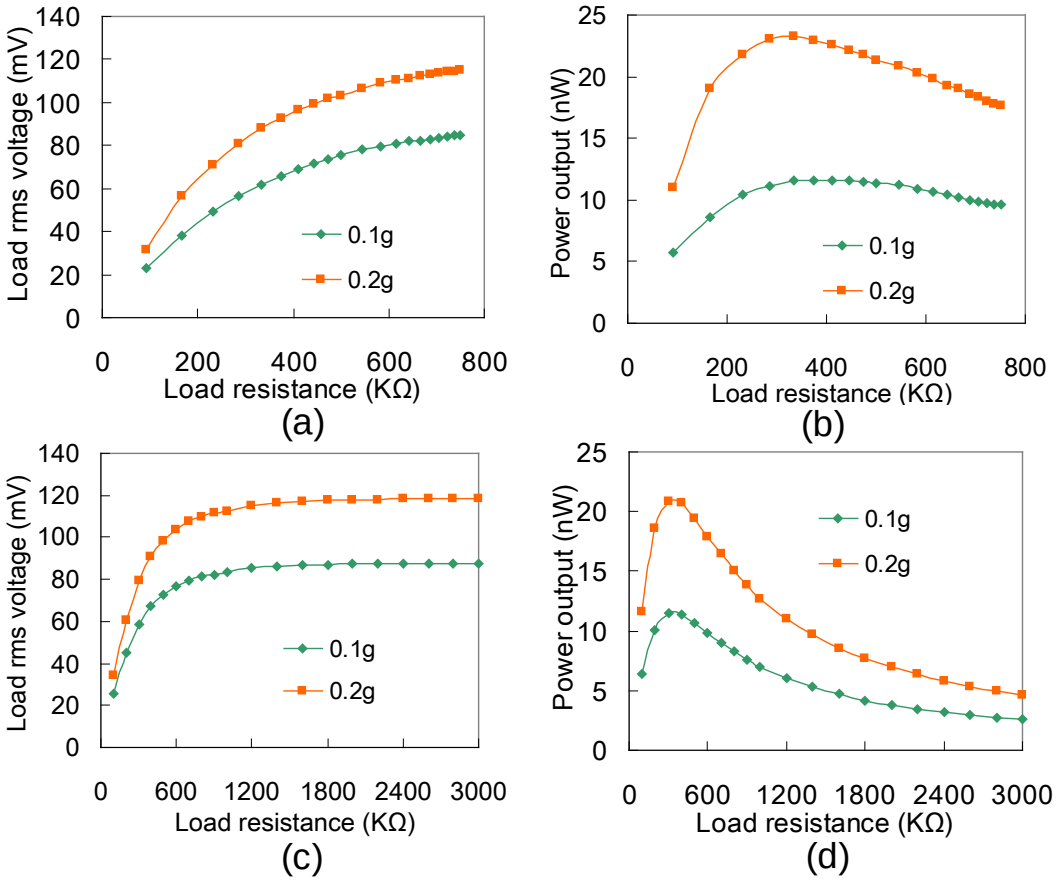

Figure B.5 Experimental results of (a) load rms voltages and (b) power outputs against load resistances for six PZT elements in parallel connection; Simulation results of (c) load rms voltages and (d) power outputs against load resistances for six PZT elements in parallel connection.

For six PZT elements connected in parallel, Figs. B.5 (a) and (b) show the experimental results of load rms voltages and power outputs against load resistances at accelerations of 0.1 g and 0.2 g. It is seen that the load rms voltage increases monotonically as the load resistance increasing. Nevertheless, the power outputs come out the peak values of 11.6 nW and 23.3 nW with matched resistance of 333 kΩ at 0.1 g and 0.2 g. The simulation results are shown in Figs. B.5 (c) and (d). Similarly, the slope of the curve of the load rms voltage tends to be gradually reduced after the load resistance continuously increased above the value of the load resistance at maximum output power. Besides, the power outputs reach the maximum values of 11.6 and 23.3 nW which are in the same level as the values of 11.4 and 20.9 nW for six PZT elements in series connection in Figs. B.4 (c) and (d) at the accelerations of 0.1 g and 0.2 g, but with a quite small matched load resistance of 330 kΩ. Thus it is concluded that, in spite of the connection types of these PZT elements, the optimal power generated for six PZT elements remain the same with respect to corresponding matching load resistance.

Comparing the experimental results in Fig. B.4 (b) and Fig. B.5 (b), although PZT elements connected in series and in parallel produce similar power into matched load resistance, the matched resistance in case of parallel is much lower than the one of series connection. So it is concluded that PZT elements in parallel connection is preferred, because it produces much higher power output than the case of series connection under low load resistance. For this reason, the power generation for PZT elements in parallel connection will be used in the measurement of this thesis.

Appendix C: List of Publications

Journal papers

1. **Huicong Liu**, Bo Woon Soon, Nan Wang, C J Tay, Chenggen Quan, and Chengkuo Lee, “Feasibility study of a 3-D vibration-driven electromagnetic MEMS energy harvester with multiple vibration modes”, J. Micromech. Microeng., vol. 22, no. 12, 125020, 2012.

2. **Huicong Liu**, Chengkuo Lee, Takeshi Kobayashi, C. J. Tay, and Chenggen Quan, “Piezoelectric MEMS-based wideband energy harvesting systems using a frequency-up-conversion cantilever stopper”, Sens. Actuators A: Phys., vol. 186, pp. 242-248, 2012.

3. **Huicong Liu**, Chengkuo Lee, Takeshi Kobayashi, C. J. Tay, and Chenggen Quan, “Investigation of MEMS piezoelectric energy harvester system with frequency-widen-bandwidth mechanism introduced by mechanical stoppers”, Smart Mater. Struct., vol. 21, no. 3, pp. 035005, 2012.

4. **Huicong Liu**, Chengkuo Lee, Takeshi Kobayashi, C. J. Tay, and Chenggen Quan, “A New S-shaped MEMS PZT Cantilever for Energy Harvesting from Low Frequency Vibrations Below 30 Hz”, Microsyst. Technol., vol. 18, no .4, pp. 497-506, 2012.

5. **Huicong Liu**, C. J. Tay, Chenggen Quan, Takeshi Kobayashi, and Chengkuo Lee, “Piezoelectric MEMS energy harvester for low-frequency vibrations with wideband operation range and steadily increased output power”, IEEE/ASME J. Microelectromech. Syst., vol. 20, no. 5, pp. 1131-1142, 2011.

6. **Huicong Liu**, C. J. Tay, Chenggen Quan, Takeshi Kobayashi, and Chengkuo Lee, "A scrape-through piezoelectric MEMS energy harvester with frequency broadband and up-conversion behaviors", Microsyst. Technol., vol. 17, no. 12, pp. 1747-1754, 2011.

7. C. J. Tay, Chenggen Quan, **Huicong Liu**, Mahadevaiah Gopal, and Ramam Akkipeddi, "Stress gradient of a micro-optoelectromechanical systems Fabry–Perot cavity based on InP", J. Micro/Nanolith. MEMS MOEMS, vol. 9, no. 2, pp. 023010, 2010.

Conference papers

1. **Huicong Liu**, Chengkuo Lee, Takeshi Kobayashi, C J Tay, and Chenggen Quan, "A MEMS-based wideband piezoelectric energy harvester system using mechanical stoppers", IEEE IEDM Tech. Dig., pp. 681-684, Washington DC, USA, Dec. 5-7, 2011.

2. **Huicong Liu**, Chengkuo Lee, Takeshi Kobayashi, C J Tay, and Chenggen Quan, "Study of the operation-frequency broadening effect of MEMS piezoelectric energy harvester for low-frequency vibrations", Power MEMS 2011, 2A-1, pp. 34-37 Seoul, Republic of Korea, Nov. 15-18, 2011.

3. **Huicong Liu**, Chengkuo Lee, Takeshi Kobayashi, C J Tay, and Chenggen Quan, "Investigation of piezoelectric MEMS-based wideband energy harvesting system with assembled frequency-up-conversion mechanism", Eurosensors XXV, Athens, Greece, Sep. 4-7, 2011.

4. Kah How Koh, Takeshi Kobayashi, **Huicong Liu**, and Chengkuo Lee, “Investigation of a piezoelectric driven MEMS mirror based on single S-shaped PZT actuator”, Eurosensors XXV, Athens, Greece, Sep. 4-7, 2011.

5. **Huicong Liu**, Takeshi Kobayashi, Nan Wang, C J Tay, Chenggen Quan, and Chengkuo Lee, “Piezoelectric MEMS energy harvesting mechanism for collecting energy from low frequency vibrations - Toward self-powered wireless sensor networking”, IEEE, The 8th International Conf. on Networked Sensing Systems (INSS), Penghu, Taiwan, June 12-15, 2011.

6. **Huicong Liu**, Chenggen Quan, C J Tay, Takeshi Kobayashi, and Chengkuo Lee, “A MEMS-based piezoelectric cantilever patterned with PZT thin film array for harvesting energy from low frequency vibrations”, 2011 International Conf. on Optics in Precision Engineering and Nanotechnology (ICOPEN 2011), Singapore, March 23-25, 2011.

7. **Huicong Liu**, C J Tay, Chenggen Quan, Takeshi Kobayashi, and Chengkuo Lee, “Dynamic characterization of a MEMS-based PZT cantilever for energy harvesting”, The International Conference on Experimental Mechanics (ICEM 2010), Kuala Lumpur, Malaysia, Nov. 29 - Dec. 1, 2010.